New radiometric age constraints on the Ordovician-Silurian boundary from Anticosti Island (eastern Canada) and the Siljan district (Sweden)

by

Mariko Cappello
Laurea, University of Bologna, 2016

A Thesis Submitted in Partial Fulfillment of the
Requirements for the Degree of

MASTER OF SCIENCE

in the School of Earth and Ocean Sciences

Acknowledging with respect the Lekwungen-speaking peoples on whose traditional territory the university stands and the Songhees, Esquimalt and W̱SÁNEĆ peoples whose historical relationships with the land continue to this day.

University of Victoria

New radiometric age constraints on the Ordovician-Silurian boundary from Anticosti Island (eastern Canada) and the Siljan district (Sweden)

by

Mariko Cappello
Laurea, University of Bologna, 2016

Supervisory Committee

Dr. Jon Husson, Supervisor
(School of Earth and Ocean Sciences)

Dr. Dante Canil, Departmental Member
(School of Earth and Ocean Sciences)

Dr. Vera Pospelova, Departmental Member
(School of Earth and Ocean Sciences)

ABSTRACT

The transition from the end of the Ordovician to the beginning of the Silurian Period is characterized by the glaciation of the Gondwana paleocontinent, eustatic sea level change, a perturbation to the global carbon cycle and one of the five major mass extinctions of the Phanerozoic Eon. Due to significant sea level fall, the Ordovician-Silurian (O-S) boundary is often marked by hiatus and exposure in the shallow marine geologic record (e.g., Copper et al. [2013]). Two locations that host stratigraphic succession close to the boudary are Anticosti Basin of Quebec (Canada, e.g., Desrochers et al. [2010]), and the carbonate mounds of the Siljan ring district (Dalarna County, Sweden, e.g., Ebbestad et al. [2015]).

The exact timing and dynamics of the glaciation and mass extinction are yet to be understood. Similarly, the interplay between those events and the carbon cycle perturbation are still unclear. As a result, there is a serious need for radiometric age constraints in this crucial part of the Paleozoic Era. The acquisition of more radiometric dates, achieved in this study, aims to address the present dearth of absolute dates close to the boundary. The dates produced in this study represent the first modern geochronologic constraints on the O-S boundary, leveraging the development of the EARTHTIME initiative and the latest U-Pb dating techniques that have improved accuracy and allowed for dating of single zircon crystals at $\leq$0.1% precision level.

Here I present two new U-Pb zircon ages obtained via bentonite dating. The first bentonite, 443.61±0.52 Ma (2σ, including analytical, tracer calibration and decay constant uncertainties) was collected from the base of the Lousy Cove Member, Ellis Bay Formation (Anticosti Island, Quebec, Canada). The second one, 443.28±0.50 Ma (including analytical, tracer calibration and decay constant uncertainties) comes from a karstic void within the Boda Core Facies of the Boda Formation (Dalarna County, Sweden). U-Pb geochronology

(chemical abrasion, isotope dilution, thermal ionization mass spectrometry: CA-ID-TIMS) on single zircons was used to obtain these ages.

These results are the closest radiometric ages to the current O-S boundary (compared to any time constraints in the 2012 Geologic Time Scale) and allow to significantly reduce the uncertainty of the current age boundary (443.8±1.5, Cohen et al. [2018]). Furthermore these absolute ages have been used to make models that explore drivers of Earth system change, such as an end-Ordovician global carbon cycle perturbation.

Contents

List of Tables

List of Figures

ACKNOWLEDGEMENTS

This research was funded by an NSERC Discovery Grant awarded to Jon Husson. I would like to thank the University of Victoria for granting the use of laboratory equipment and facilities. I would also like to thank Paul Copper for pointing out the main target horizon in Macaire Creek (Anticosti Island, Quebec), André Desrochers for sharing his knowledge and expertise while guiding us on the field, Kristin Bergman and Seth Finnegan for the helpful collaboration and support in the field and beyond. A special thanks goes to Blair Schoene and the brilliant reseachers working at the Princeton Radiogenic Isotope Laboratory for letting us use their equipment and for their continued assistance and support necessary to carry out CA-ID-TIMS on our samples. Thanks to David S. Jones and Joshua Zimmit for the insightful conversations and support. Thanks to Dante Canil, Rebecca Morris and Rebecca Scholtysik for their help with the geochemical characterization and petrographic observations of one of our samples. I also want to thank Vera Pospelova and Chris Barnes for sharing their paleontological expertise and for their useful suggestions. Last, but not least, thanks to Jon Husson for the continued support from the very start, for always making time and for the ever positive and constructive feedback.

"There's truth even in tainted knowledge, if one reads carefully"

N. K. Jemisin

DEDICATION

To Yake.

For the inspiring conversations. For the out-of-the-box thinking.

For never making anything too easy.

Chapter 1

Introduction

This chapter has a three-fold purpose: to give an overview of the Ordovician-Silurian boundary, to lay out the chronostratigraphic cornerstones of the current late Ordovician-early Silurian time model and lastly, to introduce the motivation for this study. The first part, section 1.1, presents the major events that characterize the boundary. The second part, section 1.2, outlines some of the main stratigraphic correlation tools adopted to help define the boundary. The last paragraph, section 1.3, introduces the problem that this research project is trying to tackle, and describes the approach undertaken in this study.

1.1 The Ordovician-Silurian boundary

The transition between the Ordovician Period, presently defined as 485.4-443.8 million years ago (Ma), and the Silurian Period, presently defined as 443.8-419.2 Ma, is marked by profound perturbations to the Earth system. The geological record shows evidence of a large scale glaciation, with its peak in the Hirnantian Stage (last stage of the Ordovician, 445.2-443.8 Ma). Moreover lithological, stratigraphic and isotopic proxies indicate a mass extinction and a perturbation to the global carbon cycle (e.g., Melchin et al. [2013], Sheehan [2001]). Sea level, ocean circulation and geochemistry were also significantly altered (e.g., Sheehan [2001]).

The strongest evidence for glaciation comes from the preservation of glacial deposits (tillites) and glacial striations in Africa and South America (e.g., Hambrey [1985], Staden et al. [2010]). Positive changes in δ_{18}O isotope record (e.g., Brenchley et al. [1994], Marshall and Middleton [1990]) and clumped isotope paleothermometry studies (e.g., Finnegan et al. [2011a]) are also consistent with ice-age conditions. The glaciation was mainly limited to the Hirnantian Age, during which a large ice-sheet covered the Gondwana paleocontinent (e.g., Finnegan et al. [2011a]). This glaciation was atypical considering the atmospheric conditions of the time. In fact, even though the sun was approximately 5% dimmer than today, the partial pressure of CO_2 (pCO_2) is thought to have been $\sim$16x the present atmospheric level (Sheehan [2001]). The glaciation included multiple smaller cycles of ice growth and retreat, which are associated with high-frequency glacio-eustatic cycles (e.g., Dabard et al. [2015], Desrochers et al. [2010]). Through a combination of ice-sheet volume and distribution estimates, as well as an updated paleogeography, the eustatic sea-level fall is estimated as 130 m during peak glacial conditions (Creveling et al. [2018]). Due to the large sea level fall, shallow marine basins became exposed, hence the rock record of this time is punctuated by hiatuses, especially in epeiric seaways. The scarcity of continuous and well preserved stratigraphic successions represents a significant challenge when it comes to analyzing events such as the Late Ordovician Mass Extinction.

The Late Ordovician extinction is the first of the “Big Five” extinctions of the Phanerozoic Eon (e.g., Brenchley et al. [2001], Harper et al. [2014]). About 85% of marine species went extinct (Jablonski [1991]). It has been suggested that the extinction occurred in two pulses (e.g., Finnegan et al. [2016], Harper et al. [2014], Sheehan [2001]). The first occurred as climate cooling began, near the end of the Katian Stage (453.0-445.2 Ma), and the second pulse took place at the end of the Hirnantian Stage, during the climate warming that ended the Ordovician glaciation. There is a general consensus that this mass extinction is linked to glaciation (e.g., Crampton et al. [2016], Finnegan et al. [2011a,b, 2012], Sheehan [2001]), yet there is no clear consensus on the exact killing mechanism(s). There are a number of potential factors, including temperature change, loss of habitat due to eustatic sea level fall, and changes in ocean circulation patterns and marine geochemistry, such as oxygen levels (e.g., Sheehan [2001], Smolarek et al. [2017], Zou et al. [2018]). Evidence from paleobiologic studies suggests that multiple coinciding factors have contributed to the mass extinction (e.g., Finnegan et al. [2012, 2016], Harper et al. [2014], Wright and Stigall [2013]).

Carbonate strata from the Hirnantian Stage record a positive C isotope excursion signal, considered indicative of a global carbon cycle perturbation. This perturbation, known as the Hirnantian Isotope Carbon Excursion (HICE), has been linked with the glaciation (e.g., Brenchley et al. [1994]). Carbon isotope analyses have been used not only to better understand environmental perturbations (e.g., Quinton et al. [2016]), but also as a means to improve global stratigraphic correlations (e.g., Bergström et al. [2014]), as C isotopic excursions can be used as time markers for intra- and inter-basin correlation.

1.2 Ordovician-Silurian time-model: literature review

An inter-regional biostratigraphic correlation framework based on graptolite stratigraphy is the foundation for a time model for the O-S boundary. Graptolites are colonial organisms knows for their fast evolution and world-wide distribution which makes them ideal marker fossils (e.g., Loydell [2012], Berry [1962]). They are often preserved as pale "films" in black shales (e.g., Underwood [1992]). More recently, new approaches have been adopted to complement and strengthen the biostratigraphic model. These approaches use isotopes, both stable and unstable. Stable isotopes of carbon (^{12}C and ^{13}C) are widely used for chemostratratigraphy. Unstable isotopes, such as the ones belonging to the U-Th-Pb (uranium-thorium-lead) decay chain, are used for radiometric dating. This type of dating produces numeric ages that anchor the Geologic Time Scale. The following paragraphs give a brief overview of the time constraints on the current O-S boundary (see Fig. 1.1 and Fig. 1.2).

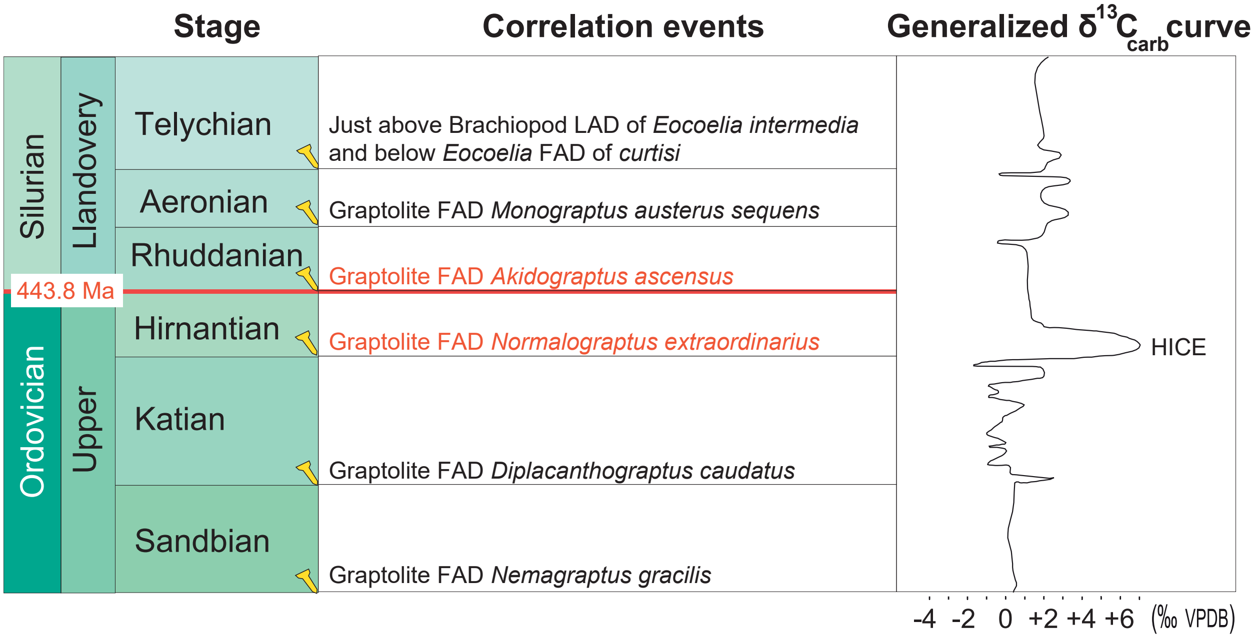

Figure 1.1: Primary correlation events and generalized carbonate carbon isotope curve for the Upper Ordovician and Lower Silurian (Llandrovery). Chronostratigraphic units and O-S boundary age from Cooper et al. [2012], Melchin et al. [2013]. The correlation events are from Ogg and Ogg [2008]. Generalized carbon isotope curve from Bergstroem et al. [2009], Cramer et al. [2011], Melchin et al. [2013]. FAD=First Appearance Datum. LAD=Last Appearance Datum. HICE=Hirnantian Isotope Carbon Excursion.

1.2.1 Biostratigraphy

The beginning of the Ordovician was marked by a significant radiation of marine organisms, known as the GOBE (Great Ordovician Biodiversification Event), resulting in high levels of biodiversity in marine ecosystems (e.g., Droser and Finnegan [2003], Munnecke et al. [2010]). Graptolites, class Graptolithina of Phylum Hemichordata (e.g., Xu et al. [2006]), are particularly abundant in Ordovician and Silurian sedimentary systems. Hence, graptolite stratigraphy has been the dominant method used for global correlations (e.g., Loydell [2012], Ogg and Ogg [2008], Toghill [1968], Xu et al. [2005]). Other biostratigraphic groups such as conodonts and chitinozoans also are useful for global correlations; while some other groups, such as brachiopods, corals and trilobites, have been found more suitable for regional zonation (e.g., Ogg and Ogg [2008]).

The Hirnantian is the last stage of the Ordovician, while the Rhuddanian (443.8-440.8 Ma) is the first stage of the Silurian (see Fig. 1.1). Both the base of the Hirnantian and the base of the Rhuddanian GSSP (Global Stratigraphic Section and Point) are defined in graptolitic shales. Graptolites are commonly found in fine-grained and organic-rich siliciclastic deposits (shales) rather than in coarse-grained siliciclastics and carbonate deposits. This makes correlations difficult between shale-rich and shale-poor deposits, the latter of which are typical of shallower marine environments. Therefore, tentative correlations between graptolites and different taxa must be adopted to attempt correlations on a global scale. The GSSP that marks the Hirnantian base is in Southern China, 0.39 m below the base of the Kuanyinchiao bed in the Wangjawan North section, Yichang (western Hubei). This corresponds to the FAD (First Appearance Datum) of the graptolite species *Normalograptus extraordinarius* (Chen et al. [2006], Gradstein et al. [2012]). The GSSP for the base of the Rhuddanian (equivalent to the Ordovician-Silurian boundary) is in Dob′s Linn, Scotland, 1.6 m above the base of the Birkhill Shale. This corresponds to the *Akidograptus ascensus* FAD[1] (Cooper et al. [2012], Melchin et al. [2013], Rong et al. [2008]).

---

[1] The base of the *Parakidograptus acuminatus* biozone (Holland [1985]) used to be considered the marker for the O-S boundary, but today this is known to be incorrect (e.g., Ogg and Ogg [2008]).

1.2.2 Chemostratigraphy: carbon isotope stratigraphy

Carbon stratigraphy is a widely used chemostratigraphic approach for the Late Ordovician. Carbon has two stable isotopes: ^{12}C, with a nucleus composed of 6 protons and 6 neutrons, is the most abundant (98.93%) and ^{13}C (6 protons and 7 neutrons) is rare (1.17%; Rosman and Taylor [1999]). The ratio between the heavy (^{13}C) and light (^{12}C) isotopes can be measured in carbon in sedimentary rocks (either as carbonates ($CaCO_3$) or sedimentary organic matter). Natural variations in this ratio are very small (on the order of parts-per-thousand), and so carbon ratios are expressed as δ values, measured as permil deviation from an internationally-recognized standard (White [2015]). In Equation 1.1, R is the ratio between the heavy and the light isotope (in this case, R=^{13}C/^{12}C) and the Vienna Dee Pee Belemnite (VDPB) is the commonly used standard (e.g., Tiwari et al. [2015]).

$$\delta^{13}C = \left\{ \frac{(R)_{sample}}{(R)_{standard}} - 1 \right\} * 10^3 \tag{1.1}$$

In different stratigraphic successions across the world, a positive signal (known as the Hirnantian Isotope Carbon Excursion (HICE), see Fig. 1.1) has been recorded in the δ^{13}C profiles of Hirnantian sediments (e.g., Brenchley et al. [2003], Holmden et al. [2013], Jones et al. [2011]), suggesting global environmental changes. The $\delta^{13}C_{\mathrm{carb}}$ (δ^{13}C of inorganic carbon) of pristine marine carbonates (i.e., carbonates that have a primary carbon isotopic signature) reflects the $\delta^{13}C_{\mathrm{carb}}$ of dissolved inorganic carbon in the ocean (e.g., Kump and Arthur [1999], Shackleton [1985]). It has been suggested that carbon isotope excursions measured in carbonates are synchronous (e.g., Brenchley et al. [2003], Kump and Arthur [1999])[2]. This is one of the reasons why many studies concerned with the Late Ordovician

---

[2] Synchroneity may not be valid for isotopic carbon peaks of carbonates ($\delta^{13}C_{\mathrm{carb}}$) and organic carbon

have focused on chemostratigraphy. The positive excursion (up to $\geq 6‰$ in the Baltic region, e.g., Brenchley et al. [2003]) is recorded in sediments from different paleocontinents, suggesting that this signal represents a large scale environmental change rather than a local process (e.g., Brenchley et al. [2003], Munnecke et al. [2010]). Even though the positive curve can be observed at a global scale, the absolute values of the excursion are different in different locations. Such difference could suggest that regional paleoenvironmental and geological settings also effect the carbon isotope record (e.g., Melchin et al. [2003]).

Nonetheless, the HICE has been recognized on different continents. Several studies focus on the carbon isotope curves of deposits from Laurentia and Baltica (e.g., Bergström et al. [2015], Brenchley et al. [2003]). These studies suggest that the carbon isotopic profile of the Late Ordovician can be used as a chronostratigraphic ruler against which biozonal boundaries and biotic events can be placed (see Fig. 1.1), enabling high resolution global correlation (e.g., Bergstroem et al. [2009], Bergström et al. [2014, 2015], Brenchley et al. [2003], Holmden et al. [2013]).

1.2.3 Radioisotopic dating

There are many radiometric dates that have been obtained for the Ordovician Period (e.g., Tucker and McKerrow [1995]), yet most of them are not accepted today for calibration of geologic time because they do not achieve the acceptable standards of precision, accuracy and suitable stratigraphic constraint to be useful (e.g., Cooper et al. [2012], Tucker et al. [1990], Tucker and McKerrow [1995]). According to the most recent Geologic Time Scale (GTS 2012), there are currently no radiometric dates for the Hirnantian Stage (Schmitz and Kuiper [2013]).

---

bearing sediments ($\delta^{13}C_{org}$), i.e., shales. This discrepancy can make correlations between carbonate and shale deposits challenging.

During the 1980s, the first isotopic ages for the Ordovician and Silurian systems were produced, using fission-track dating of zircons and apatites from tuffs and bentonites (Ross et al. [1982]). The dated samples were biostratigraphically well constrained and easily correlatable with the British graptolite biozonation. Nevertheless, it has since become clear that the fission-track methods are unsuitable for the refinement of the time scale, due to the large uncertainty on the results obtained (as high as ∼10%, 1σ). Therefore different techniques that could achieve better precision were adopted thereafter. Uranium-lead (U-Pb) dating is more reliable and can produce more precise dates, hence Tucker et al. (Tucker et al. [1990]) re-dated four samples (previously dated with fission track) with the isotope dilution method. It became clear that most of the ages that were not obtained through U-Pb dating had to be rejected (Cooper et al. [2012], Tucker and McKerrow [1995]).

In the GTS 2012, the radiometric ages closest to the O-S boundary are from the Katian Stage (below the Hirnantian, 453.0-445.2 Ma) and from the Rhuddanian Stage (e.g., Kunk et al. [1985], Ross et al. [1982], Tucker et al. [1990]). The Katian age (444.88±1.17 Ma), was obtained with U-Pb dating of zircon in a bentonite collected in the Hartfell Shales Formation of Dob′s Linn, Scotland (Fig. 1.2). There are two accepted radiometric ages for the Rhuddanian Stage (Fig. 1.2). The first one (442.59±5.36 Ma) was obtained with Ar-Ar dating of an ash collected in the Descon Formation of Esquibel Island, Alaska. The second age (439.57±1.33 Ma) was obtained with U-Pb dating of an ash collected from the Birkhill Shale Formation of Dob′s Linn, Scotland.

1.3 Motivations for this study

Numerous biostratigraphic and geochemical studies have been conducted to understand what is the order in which the different Late Ordovician events occurred, how long they lasted, and how they are interrelated. The number of geochronological studies, by contrast, is scarce. The current timescale relies heavily on biostratigraphic and chemostratigraphic work. An improved timescale can be produced with the aid of radiometric dating, by providing more precise dates of geological deposits close to the Ordovician-Silurian boundary (henceforth, O-S boundary). This study introduces two new radiometric dates from zircons extracted from Upper Ordovician bentonite beds, which are layers derived from the weathering of a volcanic ash (e.g., Ross and Shannon [1926]). One of the bentonites comes from Anticosti Island (Quebec, Canada), while the other one is from the Siljan District (Dalarna County, Sweden). U-Pb ages on single zircon crystals were obtained via chemical abrasion, isotope dilution, thermal ionization mass spectrometry (CA-ID-TIMS) to date the bentonites. The ages produced in this study are closer to the current O-S boundary than any age constraint used in GTS 2012. In order to gain more insights on the mass extinction, glaciation and carbon cycle perturbation that marked the O-S boundary, precise absolute ages are crucial for constraining the rates of Earth system change and the processes that drove them.

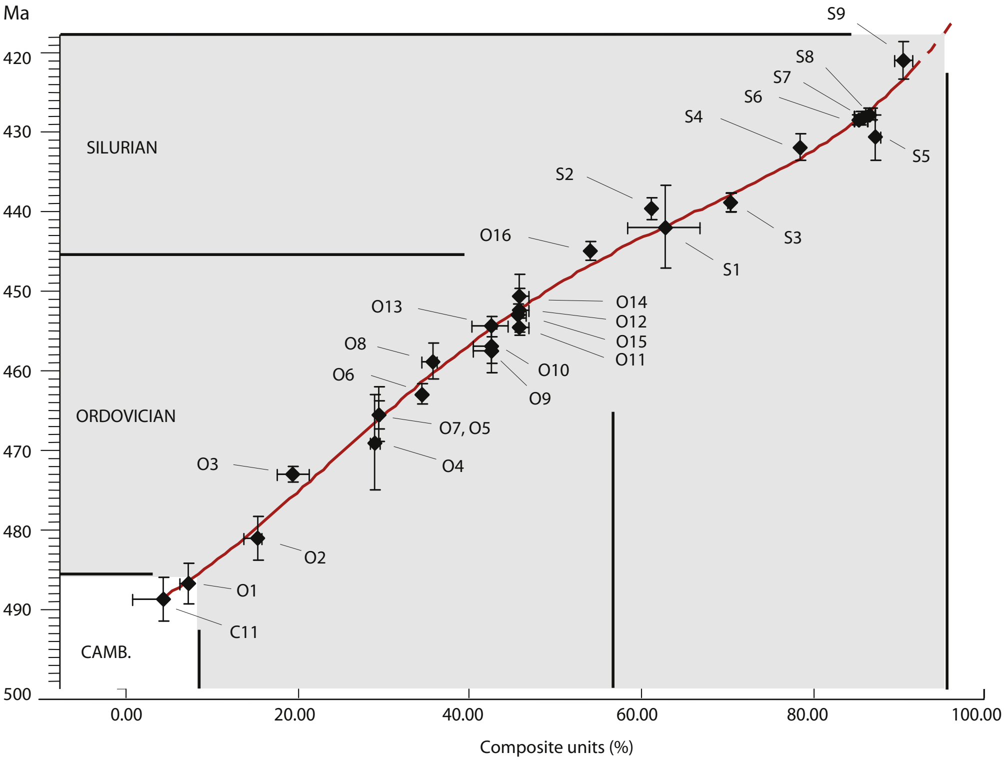

Figure 1.2: Calibration of the Ordovician-Silurian graptolite composite standard of the GTS 2012. The y-axis shows ages in Ma, and the x-axis is a composite section, designed to represent linear progress through a given time bin (i.e., 50% of total time elapsed). Radioisotopic dates of bentonites of acceptable quality (GTS 2012, Appendix 2) have been included to constrain this age model. Vertical analytical bars indicate the age error, while the horizontal error bars show the stratigraphic uncertainty. Heavy black lines are Period boundaries. Note the lack of ages near the O-S boundary. Figure edited from Cooper et al. [2012].

Chapter 2

Study Areas

After describing the major Earth history events that characterize the O-S boundary and the significance of developing more radiometric age control, this chapter gives more specific details about the sampling localities and samples used for this work. The first locality described is Anticosti Island, in eastern Canada (section 2.1) and the second locality is the Siljan district of Sweden (section 2.2).

2.1 Anticosti Island

Anticosti Island (see map in Fig. 2.1) is located in in the Gulf of Saint Lawrence, Quebec (eastern Canada). This island has long been the subject of stratigraphic and paleontologic study (e.g., Achab et al. [2011], Barnes [1988], Delabroye et al. [2012], Jin and Copper [2008], Melchin [2008]), owing to its superbly preserved Ordovician and Silurian fauna and for its easily accessible outcrops. The Anticosti Basin has also been the object of chemostratigraphic studies, due to the dominance of carbonate strata suitable for isotopic analyses (e.g., Jones et al. [2011], Long [1993]). This study represents the first attempt to bring U-Pb age constraints to this locality, which has long been important to the study of the O-S boundary.

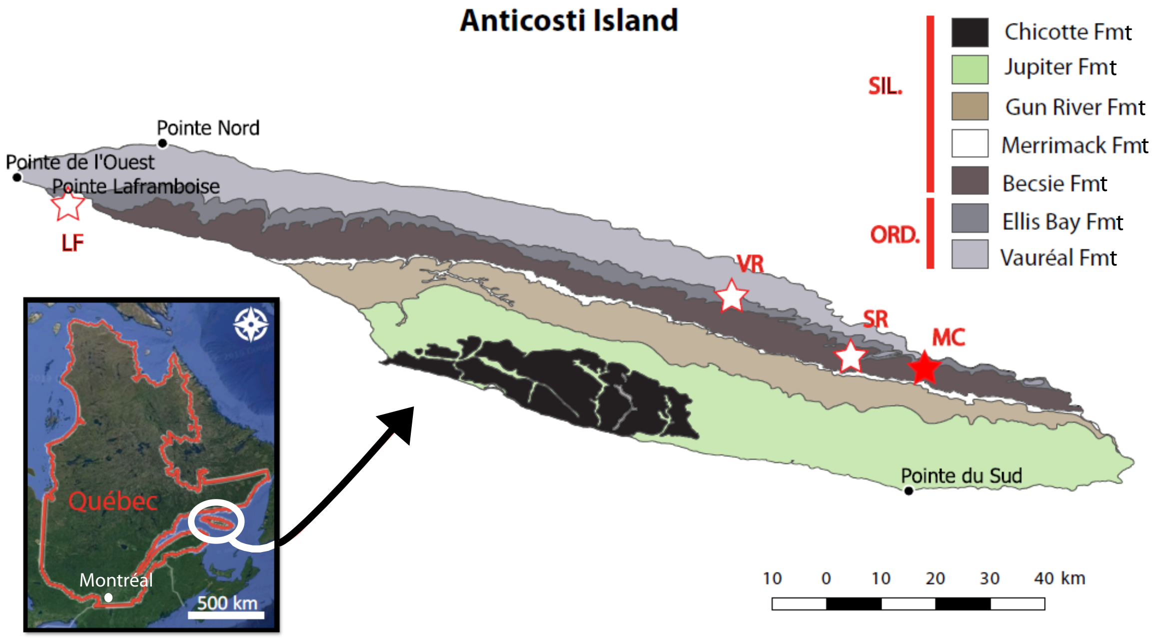

Figure 2.1: Geologic map of Anticosti Island, Quebec (Canada), edited from Desrochers et al. [2010]. The different colors represent different geological formations. Stars indicate sampling locations, with the filled star being the one sample that yielded a successful U-Pb depositional age. The other samples were processed, but did not yield eruptive ages. From left to right: LF=Laframboise Point, VR=Vauréal Falls, SR=Salmon River, MC=Macaire Creek.

2.1.1 Paleo-geographic and geologic settings

Strata on Anticosti Island span the Upper Ordovican to Lower Silurian, and represent one of the best preserved, most complete, fossil rich and well exposed stratigraphic successions deposited in a paleo-tropical setting (e.g., Copper et al. [2013]). During the Ordovician this site was situated in the southeastern margin of the Laurentia paleocontinent (see Fig. 2.2). The Anticosti Basin lays on Mesoproterozoic crust (Mesoproterozoic era: 1600-1000 Ma) (e.g., Waldron et al. [1998]). The Anticosti sediments were deposited in a foreland basin, on the west margin of the Iapetus Ocean (e.g., Long [2007]). As the Iapetus Ocean was closing, the Appalachian mountains were forming via the Taconic Orogeny. These collisional

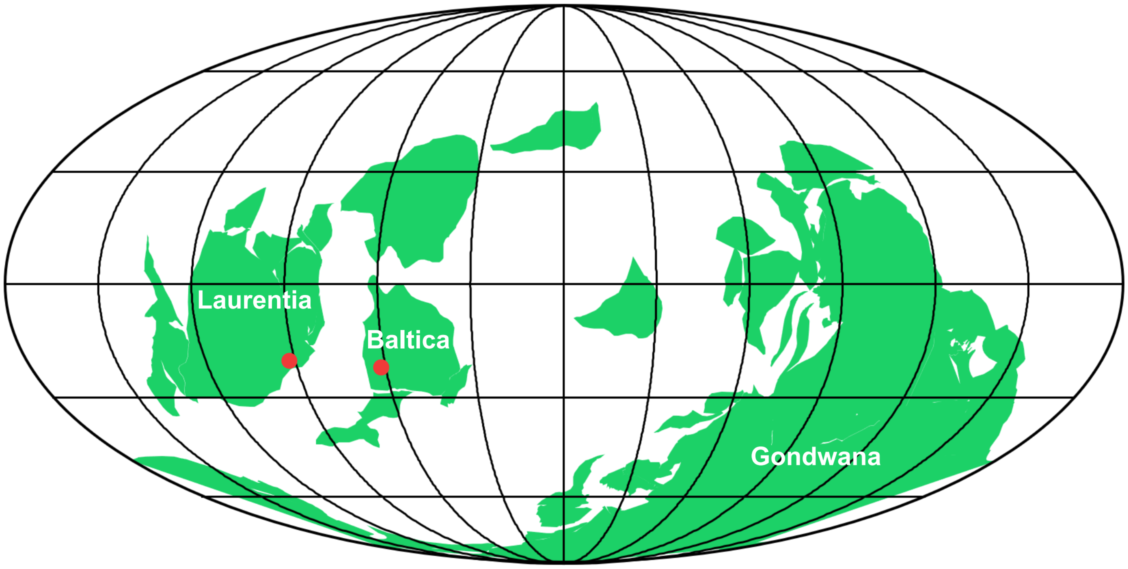

Figure 2.2: This image shows the paleogeography of 444 million years ago. The red dot within Laurentia shows where the Anticosti Basin was located. The red dot within Baltica shows where the Siljan district was located at the time. Paleogeographic reconstruction from Wright et al. [2013].

tectonic regimes have been connected with enhanced explosive volcanic activity (e.g., Huff et al. [1998]). Syn- and post-Taconic load subsidence (e.g., Barnes [1988], Desrochers et al. [2010]), accommodated a ∼900 m thick carbonate-siliciclastic succession (Desrochers et al. [2010]) that now extends for about 200 km from east to west, oblique to the paleo-shoreline and with strata gently dipping (less than 2°) southwestward. These sediments were deposited in a storm-dominated carbonate ramp environment (e.g., Desrochers et al. [2010], Long [2007], Sami and Desrochers [1992]). As the orogeny ceased and flexural subsidence came to an end, sediment deposition waned and halted in the Early Silurian (e.g., Long [2007]).

2.1.2 Stratigraphy

The central-western part of Anticosti is dominated by carbonate facies typical of distal offshore environments, while the eastern part presents more siliciclastic facies typical of near-shore environments (e.g., Desrochers et al. [2010], Long and Copper [1987], Sami and

Desrochers [1992]). Fig. 2.3 shows a generalized stratigraphy of the west and east ends of the island. These deposits are divided into seven formations (see geologic map in Fig. 2.1), which from oldest to youngest are: Vaureal, Ellis Bay, Becscie, Merrimack, Gun River, Jupiter and Chicotte.

This study focuses on the Upper Ordovician Ellis Bay Formation (Fmt) and the Lower Silurian Becscie Fmt, both of which outcrop throughout the island, with exceptional coastal exposures. The Lousy Cove Member (Mbr) is the upper part of the Ellis Bay Fmt (see Fig. 2.3). On the eastern side of the island, this Mbr starts with an intraclastic conglomerate overlain by interbedded limestone and shale. This is followed by a more massive nodular wackestone, overlain by interbedded shale and limestone (with numerous centimeter scale fossiliferous interbeds) grading up into a cross-stratified grainstone. The Lousy Cove is topped by an erosional surface, which forms the base of the Laframboise Mbr, the last unit of the Ellis Bay Fmt. This Mbr can easily be identified across the whole island as it includes a prominent oncolite marker bed (indicated in blue in all the images contained in this chapter), as well as an overlying calcimicrobial-coral bioherm with an erosional surface at the top. The oncolite bed consists of a poorly-bedded grainstone containing oncoids, i.e. carbonate spherules with semiconcentric layers which form as a product of microbial growth. The bioherm is a prominent thick-bedded boundstone (containing corals, stromatoporoids and other fossils), interbedded with thin calcareous and shaly layers. The characteristic oncolite bed will be recurrently used in this chapter as a way to stratigraphically constrain the collected samples. Eustatic fluctuations associated with the Late Ordovician glaciation are recorded by deposits showing transgressive-regressive (deepening-shallowing) depositional cycles in the Ellis Bay Fmt, as well as in the underlaying Vauréal Fmt (Desrochers et al. [2010]). The Ellis Bay Fmt is overlain by the Becscie Fmt. This Fmt begins with the Fox Point Mbr, a cross-stratified calcarenite on the eastern side of the island.

The Anticosti Basin is richly fossiliferous, owing in part to its very low levels of deformation (regional dips are ∼2°) (Barnes [1988], Copper et al. [2013]). Some of the most studied taxa include chitinozoans (Soufiane and Achab [2000]), brachiopods (Copper et al. [2013]), conodonts (Barnes [1988]) and acritarchs (Delabroye et al. [2012]). It has been suggested to place the O-S boundary statotype here instead of Dob′s Linn (Barnes [1988]). The main biostratigraphic element missing is a thorough graptolite stratigraphy, most commonly used for Orodovician-Silurian correlations. Well preserved graptolites are found in shale deposits, such as the ones in Yichang (Weatern Hubei, China) and the ones in Dob′s Linn (Scotland). This facies dependence of graptolites makes correlation difficult with carbonate rich sediments, such as the ones on Anticosti and in the Siljan district (described in the following section). To help address this limitation, high resolution chemostratigraphic studies that rely on C isotope excursions (such as the HICE) as correlating tools have helped refined the stratigraphy (e.g., Jones et al. [2011], Jones and Fike [2013]).

While the Ellis Bay Formation is constrained to be Ordovician and the overlying Becsie is Silurian, the exact extent of the Hirnantian Stage (last stage of the Ordovician) on Anticosti Island remains a matter of debate. According to several paleontological studies, faunal assemblages such as brachiopods, (e.g., Copper et al. [2013]); chitinozoans (e.g., Melchin et al. [2003]); and graptolites (e.g., Melchin [2008]), suggest that the whole Ellis Bay Fmt is Hirnantian in age (e.g., Melchin [2008]). These studies correlate the central and upper portion of the Ellis Bay Fmt (Prinsta to Laframboise members, see Fig. 2.3) to the *Normalograptus persculptus* biozone and the lower Ellis Bay (Grindstone and Velleda members, which underly the Prinsta Mbr) to the *Normalograptus extraordinarius* biozone.

By contrast, chemostratigraphic studies (e.g., Brenchley et al. [2003], Jones et al. [2011], Underwood et al. [1997]), argue that the Hirnantian Stage is confined to the topmost of the Ellis Bay Fmt (mainly the Laframboise Mbr, but also possibly the uppermost part of the Lousy Cove Mbr and the lowermost part of the overlaying Becscie Fmt; Fig 2.3). According to these studies, the Hirnantian in Anticosti corresponds to the prominent HICE positive signal (see Fig. 2.3). These studies show that the Ellis Bay strata below the Laframboise Mbr do not host the HICE. There are a few biostratigraphic studies (e.g., Delabroye et al. [2008], Delabroye and Vecoli [2010], Kaljo et al. [2008], Riva [1988]) that agrees with this view. According to these studies, Anticosti graptolite faunas are not diagnostic enough to be reliably adopted as a correlation tool. Chitinozoans (flask-like marine organisms that appeared in the Lower Ordovician and went extinct in the Upper Devonian, e.g., Paris et al. [2004]) may be more useful for high resolution biostratigraphy for correlations between carbonate-rich successions of Laurentia and Baltica (e.g., Soufiane and Achab [2000], Delabroye et al. [2008]). For instance, Delabroye et al. [2008] states that the chitinozoan *Belonechitina gamachiana* biozone (Soufiane and Achab [2000]) in the Ellis Bay (from the lowermost Grindstone Mbr to part of the Lousy Cove Mbr, see Fig. 2.3) can be correlated with the upper Pirgu Stage in Baltica (equivalent to the Katian Stage, immediately below the Hirnantian). This correlation argument is then consistent with the Hirnantian being confined mostly to the Laframboise Mbr (Fig. 2.3). Adding absolute dates to the Anticosti record will, amongst other things, help resolve the conundrum of the length of the Hirnantian Stage on Anticosti Island.

2.1.3 Sampling localities

During a 10-day expedition to Anticosti Island in July 2017, 14 potential bentonite samples[1] were collected from the Ellis Bay Fmt. These samples were collected from outcrops in four different sites (see Fig. 2.1) consisting predominantly of carbonate or siliciclastic-carbonate

---

[1] See Tables 2.1 to 2.4 for GPS coordinates.

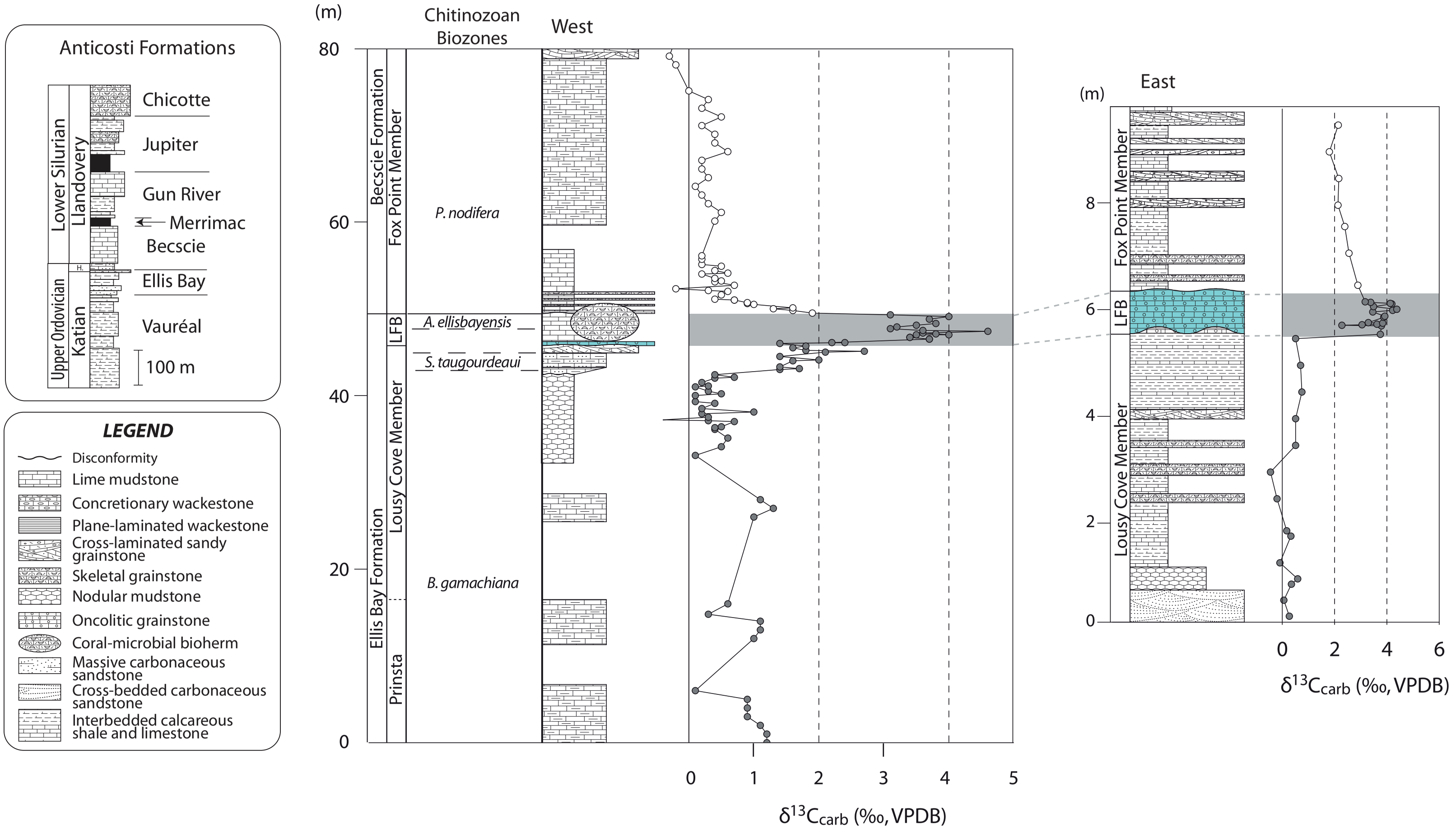

Figure 2.3: Stratigraphic units from Jones et al. [2011], chitinozoan biozonation from Soufiane and Achab [2000], lithostratigraphy and carbon stratigraphy ($\delta^{13}C_{carb}$) from Jones et al. [2011]. The grey shading is there to highlight the Laframboise Member (LFB), uppermost Member of the Ordovician Ellis Bay Formation. The base of the oncolite bed (in light blue) can be identified across Anticosti, despite its variable thickness.

sequences (see Figs. 2.4-2.8). The target horizons stood out because of their thickness (generally thicker compared to neighboring shaly strata), consistency (muddy/sticky, as compared to more lithified calcareous shale strata) and different color (brownish/greenish grey, rather than just dark grey). Collection was carried out with the aid of a geological hammer, which allowed to scrape and dig out the clay, which was then packed in a thick plastic sample bag. Samples range from a few centigrams to a couple of kilograms, depending on sampling accessibility.

Macaire Creek

Upper Ordovician volcanic zircons were successfully found and dated in only one of the samples collected on Anticosti Island. This sample was collected in the Macaire Creek (eastern Anticosti). Figure 2.4 shows the stratigraphic position of both samples collected in the Macaire Creek, including the successful one. MC-17-1:3.5 consisted of a ∼5 cm light brown, sandy clay layer, while MC-17-2:1.4 consisted of an unlithified brown-green ∼6 cm thick clay horizon. Table 2.1 shows the GPS locations of the samples collected in this location.

Location	Sample name	Latitude	Longitude
Macaire Creek	MC-17-2:1.4	49.380191	-62.204263
Macaire Creek	MC-17-2:3.5	49.378727	-62.203651

Table 2.1: List of samples collected in Macaire Creek, Anticosti Island.

While the rest of the sampling localities did not yield useful U-Pb ages, they are described below to help guide any future U-Pb sampling campaigns to Anticosti Island. The remaining sampling sites are listed from west to east: starting from Point Labramboise, moving onto the Vauréal Falls and ending with Salmon River.

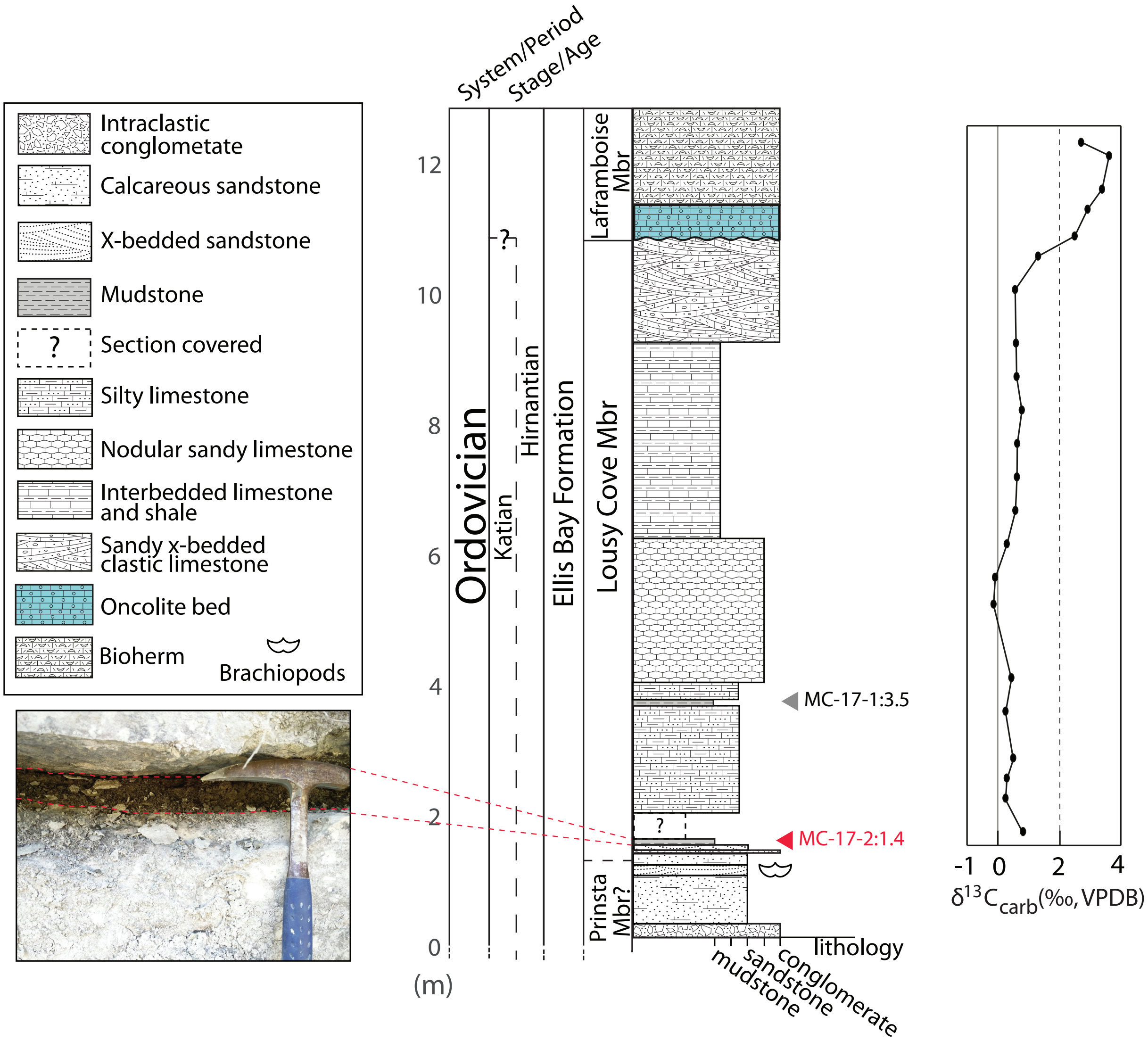

Figure 2.4: This figure shows samples collected in Macaire Creek: MC-17-1:3.5 and MC-17-2:1.4. From left to right: photo of the horizon collected, lithologic log (composite MC17-1/MC17-2/D813) and $\delta^{13}C_{carb}$ data. The $\delta^{13}C_{carb}$ data is from [Jones, personal communication, 2018]. Lithologic legend on top left corner. Successful sample (MC-17-2:1.4) is indicated in red. Both samples are situated below the oncolite bed (marked in blue).

Point Laframboise

The coastal succession in Point Labramboise (western Anticosti) consists of bioturbated grey carbonates with an abundance of fossils, including corals, stromatoporoids and brachiopods. The outcropping strata, over 300 m thick, expose nearly continuous stratigraphic record that

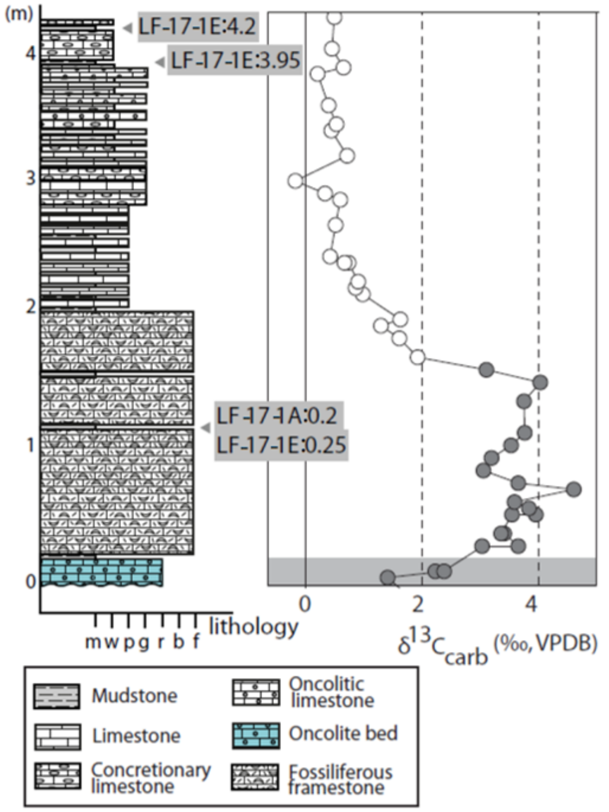

Figure 2.5: This stratigraphic section shows the position of four samples collected from Point Laframboise: LF-17-2E:0.2, LF-17-1A:0.2, LF-17-1E:3.95 and LF-17-1E:4.2. Lithology legend at the bottom. Note: all samples are above the base of the oncolite bed (in blue). On the right side there is $\delta^{13}C_{carb}$ data from Jones et al. [2011]. Oncolite bed data are shaded in grey. Unfilled data points are from the Becsie Fmt, and filled data points are from the Ellis Bay Fmt. m=mudstone, w=wackestone; p=packstone, g=grainstone, r=rudstone, f=framestone.

Location	Sample name	Latitude	Longitude
Point Laframboise	LF-17-1A:0.2	49.803344	-64.420165
Point Laframboise	LF-17-1E:0.25	49.800713	-64.381182
Point Laframboise	LF-17-1E:4.2	49.799454	-64.379954
Point Laframboise	LF-17-1E:3.95	49.799454	-64.379954
Point Laframboise	LF-17-2E:18.25	49.811193	-64.390588
Point Laframboise	LF-17-2E:17.2	49.811241	-64.390895

Table 2.2: List of samples collected at Point Laframboise.

spans the Vauréal Fmt, the entirety of the Ellis Bay Fmt, as well as part of the Becsie Fmt. We collected six samples from potential bentonite beds at Laframboise Point (see Fig. 2.5,

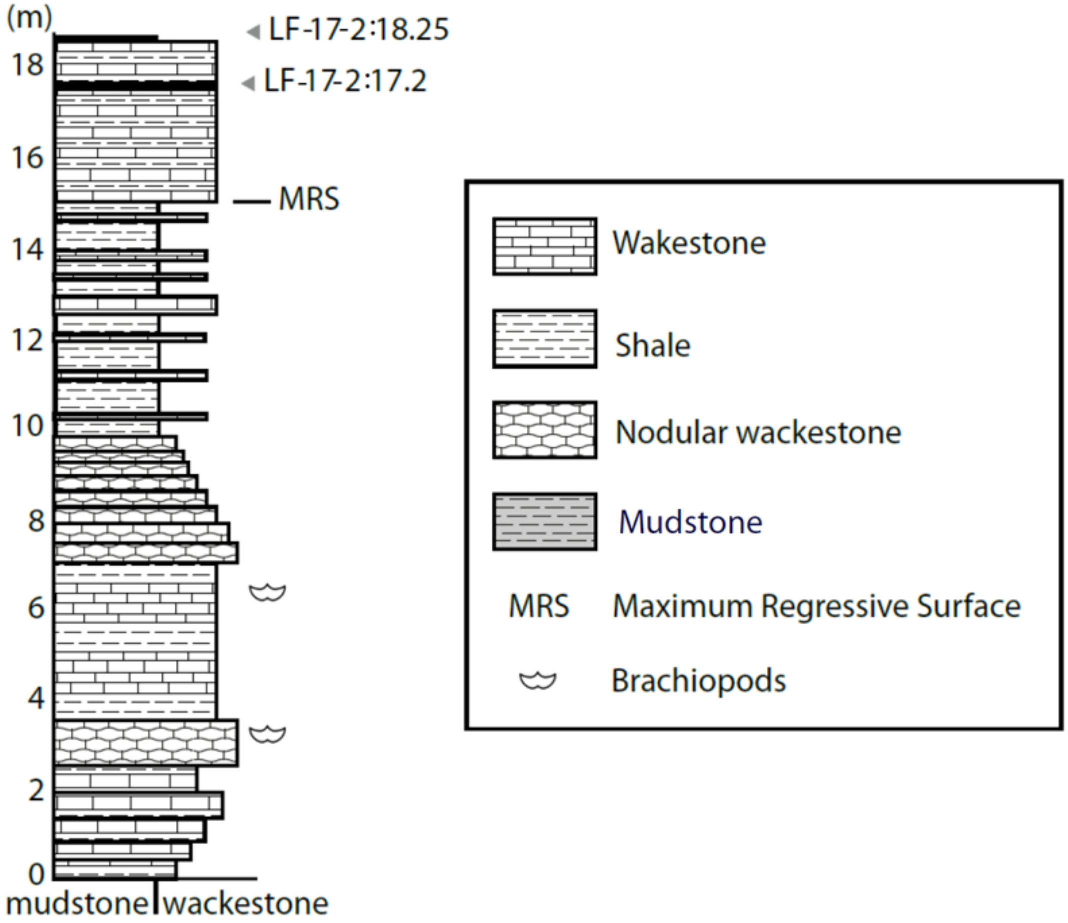

Figure 2.6: This figure shows the approximate stratigraphic position of samples LF-17-2:17.2 and LF-17-2:18.25. MRS refers to TR3 (Transgressive-Regressive sequence #3) near the contact between the Valleda and Prinsta Members, from Desrochers et al. [2010]. Legend on the right.

2.6). Samples LF-17-1A:0.2 and LF-17-1E:0.25 are from two different sections but they are the same stratigraphic horizon. The first four samples (see Table 2.2 and Fig. 2.5) were all collected close to the base of the oncolite bed: 0.2 m, 0.25 m, 3.95 m and 4.2 m above it. The last two samples are not as tightly constrained. Those were collected at a much lower stratigraphic level, close to the contact between the Prinsta (see Fig. 2.6) and the underlaying Velleda member, where a Transgressive-Regressive surface was identified by Desrochers et al. [2010] (see Fig. 2.6).

Vaureal Falls

Four samples were collected along the exposed layers adjacent to the Vaureal River, above the Vaureal Falls, within the lower Ellis Bay Fmt. GPS coordinates (see Table 2.3) and lithological description (see Fig. 2.7) are included, but where exactly these samples are positioned within the Ellis Bay Fmt is difficult to determine.

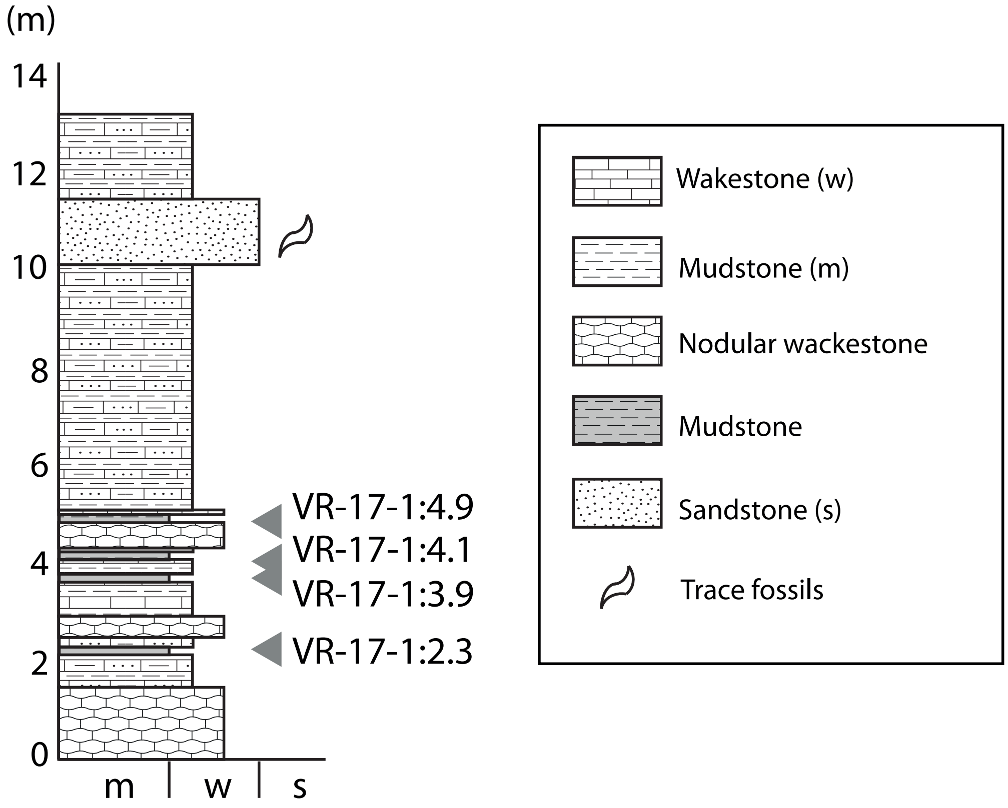

Figure 2.7: Field sketch showing the position of the samples collected in the Vaureal River, on top of the Vaureal Falls, Lower Ellis Bay. Legend on the right-hand side.

Location	Sample name	Latitude	Longitude
Vaureal Falls	VR-17-1:2.3	49.559998	-62.692596
Vaureal Falls	VR-17-1:4.9	49.559896	-62.690408
Vaureal Falls	VR-17-1:3.9	49.559896	-62.690408
Vaureal Falls	VR-17-1:4.1	49.559896	-62.690408

Table 2.3: List of samples collected in the Vauréal iver.

Salmon River

Two samples were collected in Salmon River (see Table 2.4), central-eastern Anticosti Island. One was sampled from above and one from below the oncolite bed (see Fig. 2.8).

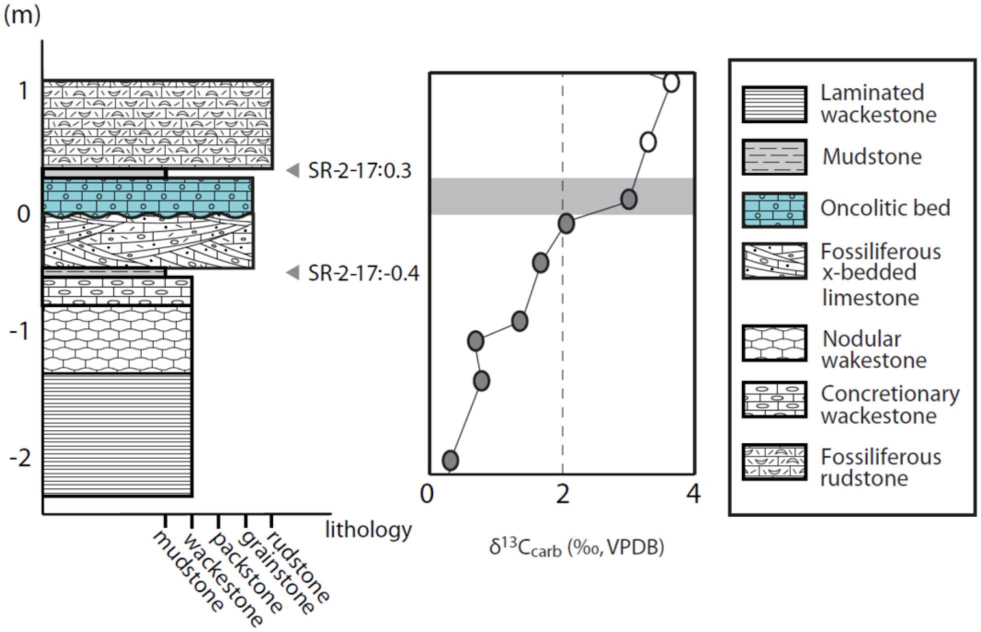

Figure 2.8: This figure shows the stratigraphic location of samples SR-2-17:-0.4 and SR-2-17:0.3 (which can be correlated to LF-17-1A:0.2 and LF-17-1E:0.25 as it is virtually in the same stratigraphic position). Legend on the right-hand side. Note: oncolite bed marked in blue. On the right side there is the δ^{13}C curve, edited from Jones et al. [2011]. Oncolite bed data are shaded in grey. Unfilled data points are from the Becsie Fmt, filled data points are from the Ellis Bay Fmt.

Location	Sample name	Latitude	Longitude
Salmon River	SR-17-2:-0.4	49.399913	-62.388988
Salmon River	SR-17-2:0.3	49.399913	-62.388988

Table 2.4: List of samples collected in Salmon River, Anticosti Island.

2.2 Siljan District

One bentonite sample was successfully dated from the Jutjärn quarry, located in the Siljan ring district (see Fig. 2.9), Dalarna County (central Sweden). Unlike the samples collected on Anticosti, this one was collected by collaborators from the University of California, Berkeley, in 2011.

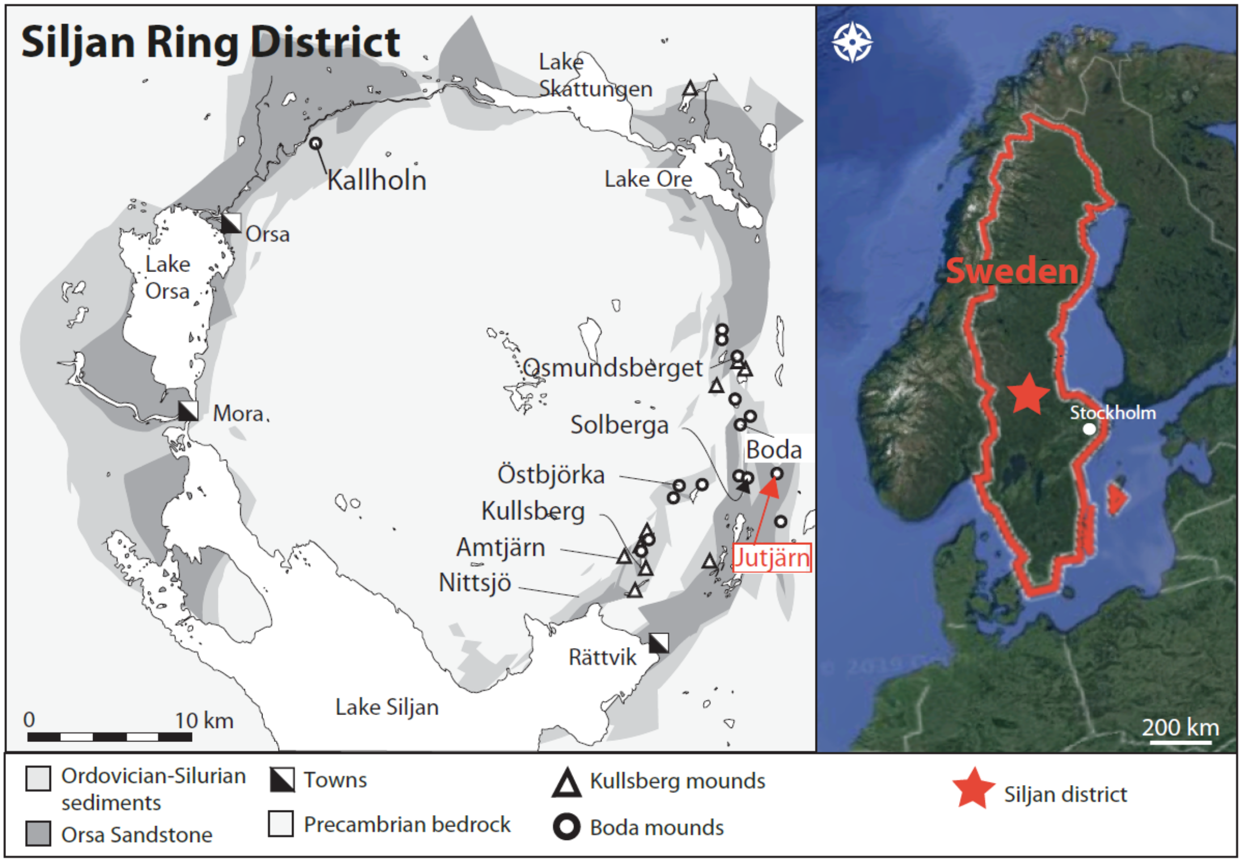

Figure 2.9: This figure shows a geologic map of the Siljan Ring District, edited from Ebbestad and Högström [2007], Ebbestad et al. [2015]. The red arrow points at the sampling location, the Jutjärn quarry.

2.2.1 Paleo-geographic and geologic settings

The Siljan district (Sweden) is part of the Baltica landmass (see Fig. 2.2 for its Late Ordovician paleogeography, red dot in western Baltica). It is called Siljan ring district due to the characteristic large circular structure (over 60 km wide), created by a late Devonian impactor (e.g., Reimold et al. [2005], Jourdan et al. [2009, 2012]), and it is the largest impact structure in Europe. Along its perimeter, Ordovician and Silurian sedimentary rocks are preserved. The strata that are most relevant to this study are the Late Ordovician (see Fig. 2.9): the Kullsberg and the Boda limestones (e.g., Ebbestad et al. [2015], Kröger et al. [2016]). These consist of massive carbonate mounds that can be up to 1000 m wide and up to 150 m tall (Kröger and Ebbestad [2014]). These structures have been interpreted as stromatactis carbonate mud-mounds (e.g., Kröger et al. [2016], Pratt [1995]). Stromatactis, which were particularly common in the Paleozoic, develop as a result of the centripetal cementation of an intricate cavity system by sparry calcite (e.g., Bathurst [1982], Kröger et al. [2016]). The bentonite sample was collected from the Jutjärn quarry within the Boda Limestone, hence the Kullsberg limestone will not be treated in this work. The Boda limestone mounds are characterized by fissures and karstic voids with syn-depositional and early post-depositional fossil rich fillings (e.g., Kröger et al. [2015, 2016]).

2.2.2 Stratigraphy

The sedimentary rocks within the Siljan district represent an important record for the Upper Ordovician in Sweden. The faunal richness (trilobites, brachiopods, bryozoans, nautiloids, gastropods, etc) and good fossil preservation within the cavities of the Boda Limestone has allowed for numerous paleontological and biostratigraphic studies (overview in Ebbestad and Högström [2007]). Carbon stratigraphy has shown that the HICE is well developed in this region (e.g., Bergström et al. [2012], Kaljo et al. [2008], Ebbestad et al. [2015]). An important correlation tool used in the Baltic basin is the recognition and tracing of different bentonite horizons found in Ordovician and Early Silurian deposits (e.g., Bergström et al. [1995], Huff et al. [1998], Kiipli et al. [2008]). The geochemistry and petrographic characteristics of these bentonite beds, rather than radiometric dating, has been used for correlation (e.g., Kiipli

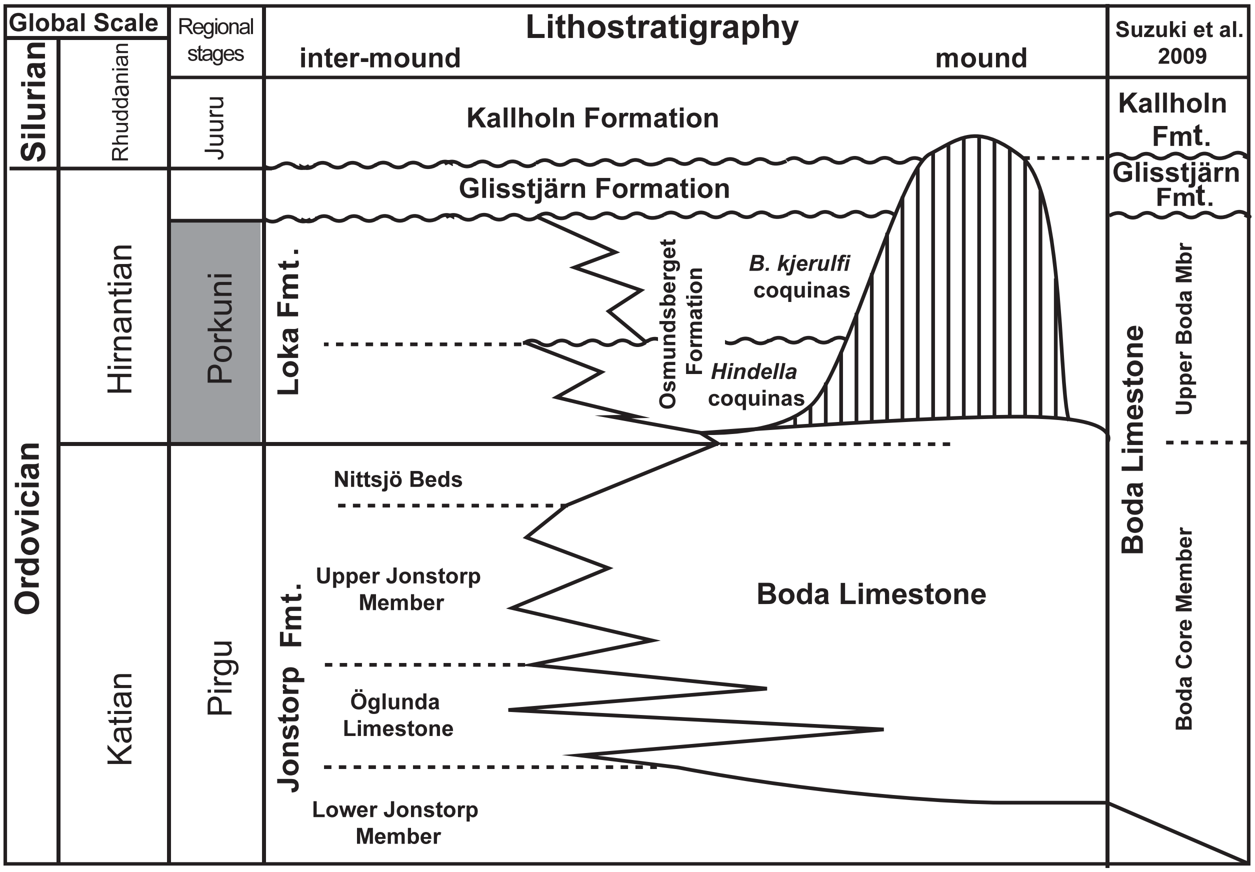

Figure 2.10: This figure shows the lithostratigraphy of the Boda Limestone and related sedimentary units. Vertical lines indicate hiatus. Fm=formation. International and regional stages on the lefthand side. The portion of the Porkuni Stage which is shaded in grey, indicates the position of the HICE. Simplified stratigraphy from Suzuki et al. [2009] on the righthand side. Figure modified from Kröger et al. [2016].

et al. [2008, 2010]). Nevertheless, K-Ar radiometric dating of Paleozoic K-bentonites of the Ordovician and Silurian period has been adopted to a lesser extent (e.g., Min et al. [2001]), but these ages are not precise or accurate enough to be useful for timescale calibration.

The stages of the Late Ordovician and Early Silurian have regional names in Baltica (see Fig. 2.10). The upper Katian is referred to as the Pirgu Stage, while the Hirnantian Stage is referred to as the Porkuni Stage (e.g., Cooper et al. [2012]). The Rhuddanian Stage is divided into the Juuru and the Raikküla stages (e.g., Cooper et al. [2012]).

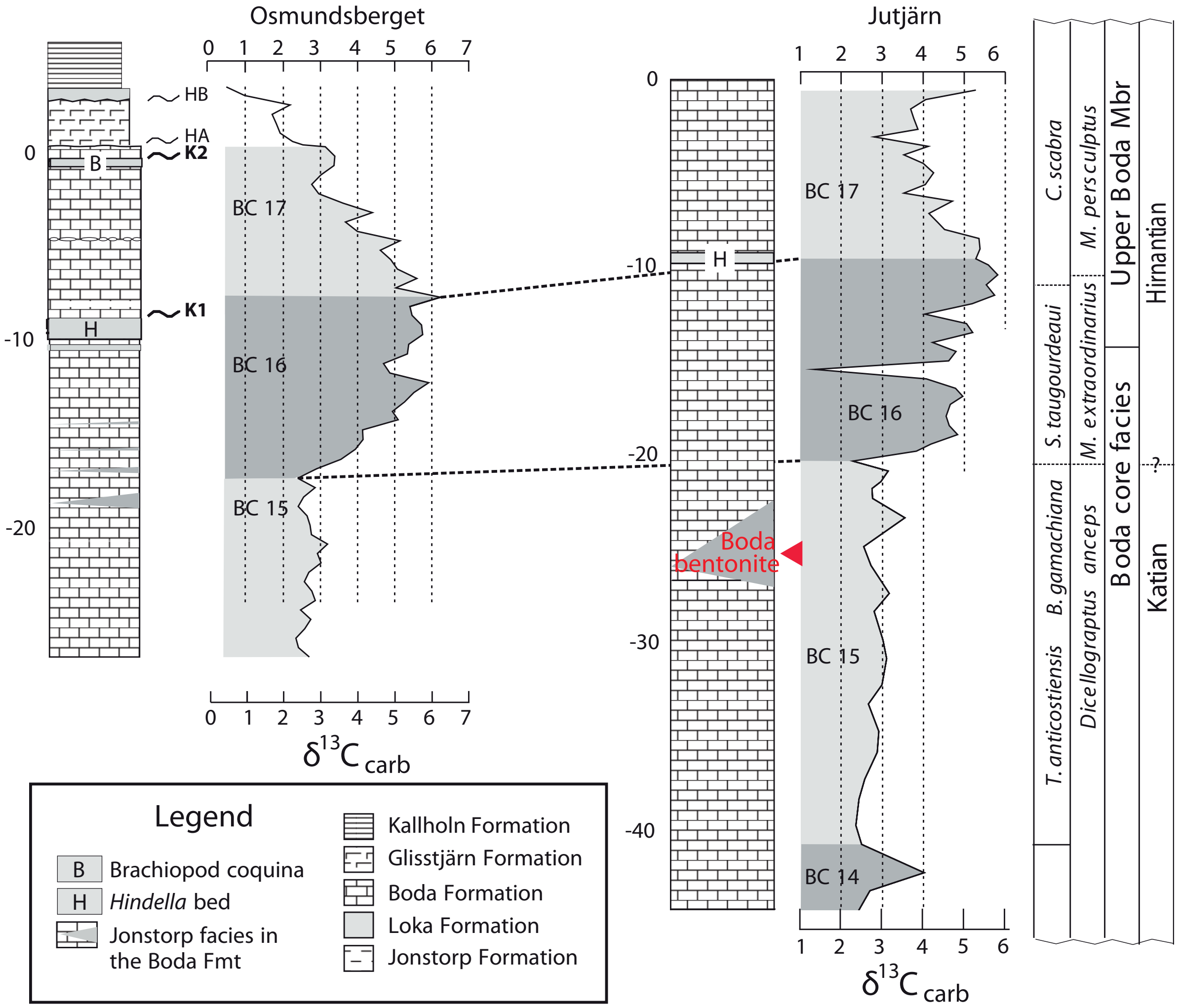

Figure 2.11: Stratigraphic and chemostratigraphic logs and C isotope data of two localities within the Siljan Ring District: Osmundsbergert and Jutjärn. Chitinozoan biozonation, graptolite zonation and chronostratigraphic units on the right-hand side. Light and dark grey indicate different C isotope zones. BC=Baltic Carbon isotope zonation after Ainsaar et al. [2010]. HA, HB, K1 and K2 are unconformities. Boda bentonite sample collected from a karst pocket, as inidicated by the red arrow. Image modified from Ebbestad et al. [2015].

2.2.3 Sampling locality

The bentonite sample, called Boda bentonite, comes from the Jutjärn Quarry. It was collected from a karstic pocket within the carbonate mud mounds of the Boda Limestone Fmt, about 15 m below the Hindella bed (see Fig. 2.11). The stratigraphic position of this sample is clear, yet its age relative to the encasing strata is debatable. As it is depicted in Fig. 2.11, the potential bentonite was collected from a karstic pocket underlying the Hirnantian positive $\delta^{13}C_{\mathrm{carb}}$ excursion. The formation of the cave (and of the deposition of the ash within it), could therefore be considered as postdepositional (younger) with respect to the enclosing sediments. Nevertheless, according to Kroger (Kröger et al. [2016]) there is faunal and lithological evidence that the karstic fillings are of Hirnantian Age, arguing for a syndepositional or early postdepositional origin for these karst pockets. The pocket hosting the Boda bentonite could be considered concomitant with one of the erosional surfaces, K1 or K2 (see Fig. 2.11) described in Kröger et al. [2015].

Chapter 3

Methods

In the field, it can be very difficult to distinguish a mudstone (sedimentary origin) from a bentonite clay (volcanic origin), as they can look exactly the same. The only way to confirm whether a sample is a bentonite is sample collection and further mineralogical, petrographic and geochemical analyses in the lab.

Zircons ($ZrSiO_4$) are common accessory minerals in felsic igneous rocks (including tuffs), extremely resistant to degradation and ideal for U-Pb radiometric dating (e.g., Faure and Mensing [2005]). U is compatible within the $ZrSiO_4$ crystal lattice, while Pb is incompatible. Zircon is also a Th-poor mineral, meaning that its initial Th/U ratio is less than the Th/U of the parent magma. Once a zircon crystallizes and becomes a closed system (no exchange with the surrounding environment), radiogenic Pb begins to accumulate in the crystal through the radioactive decay of ^{235}U and ^{238}U, both of which are long-lived radioisotopes. The half-life for ^{235}U parent isotopes to decay into its final, stable daughter isotope, ^{207}Pb, is 703.81 Ma, and ^{238}U has a half-life of 4468.3 Ma, with ^{206}Pb as final decay product (Jaffey et al. [1971]). Thus, U-Pb geochronology involves two independent decay systems that can be used to determine the zircon crystallization age. The decay of ^{238}U and ^{235}U into their stable daughters (^{206}Pb and ^{207}Pb respectively), can be described by the following equation (e.g., Faure and Mensing [2005]):

$$D^* = D_0 + N(e^{\lambda t} - 1), \tag{3.1}$$

where D* is the number of radiogenic daughter isotopes, D$_0$ is the initial amount of daughter isotope in the dated crystal, N is the number of parent isotopes, λ is the decay constant and t is time. Radioactive decay is a stochastic process. The decay constant, λ, indicates the probability that a given parent atom will decay in a time, t. As mentioned earlier, zircons incorporate U but not Pb, hence one can consider D$_0$ as negligible, assigning it a zero value. Then the equation can then be re-written as:

$$D^* = N(e^{\lambda t} - 1) \tag{3.2}$$

This general equation can be written for the two U-Pb decay systems of interest:

$$^{206}Pb^* =^{238} U(e^{\lambda_{238} t} - 1); \tag{3.3}$$

$$^{207}Pb^* =^{235} U(e^{\lambda_{235} t} - 1); \tag{3.4}$$

where λ_{238} is the decay constant[1] for ^{238}U and λ_{235} is the decay constant[2] for ^{235}U. In the case of a perfectly closed system, the ^{207}Pb/^{235}U and ^{206}Pb/^{238}U ages are the same. Zircons dated via U-Pb thus have the advantage of having two independent "clocks" within them, which allows for robust age interpretations. Moreover the soundness of U-Pb dating has improved thanks to the technical and analytical advances that have been made in the last 15 years (annealing, chemical abrasion and standard tracer solutions), allowing to produce highly precise dates.

---

[1] λ_{238}=1.55125 x 10^{-10}y^{-1} Jaffey et al. [1971].

[2] λ_{235}=9.8485 x 10^{-10}y^{-1} Jaffey et al. [1971].

The details of the mineral separation steps adopted to extract zircons from each sample are described in section 3.1. The U-Pb dating method via chemical abrasion, isotope dilution thermal ionization mass spectrometry (CA-ID-TIMS), is described in section 3.2. Fig. 3.1 shows a succinct flowchart of all mineral separation, while Fig. 3.2 depicts the CA-ID-TIMS procedures.

3.1 Mineral separation

Collected bentonite samples need processing to find and isolate the zircon crystals from everything else (such as clay minerals, carbonate fossils and organic matter). Material that was not needed for the radioisotopic analysis was progressively removed from each sample by using the mineral separation steps explained below (see Fig. 3.2). The end product were zircon-enriched separates.

3.1.1 Washing, drying and sieving

A mixture of sample and water (~1:5 ratio) was introduced inside of a regular 1.4 L kitchen blender. The mixture was blended for about 20 seconds and was given about 20 seconds for the majority of the particulate to settle down. Subsequently the clearer water at the top was gently poured out and new water was poured in. Several cycles of adding water, blending and decanting were carried out until the water lost the dark mud color and became nearly transparent. Then, the water was decanted, and the wet sample placed in an oven at 70°C to dry for 24+ hours. This simple washing procedure allows the removal of the lightest particles, which remain suspended in the water and are decanted. Once the samples were dry, they were sieved with a 500 μm mesh to remove larger granules and fossil fragments.

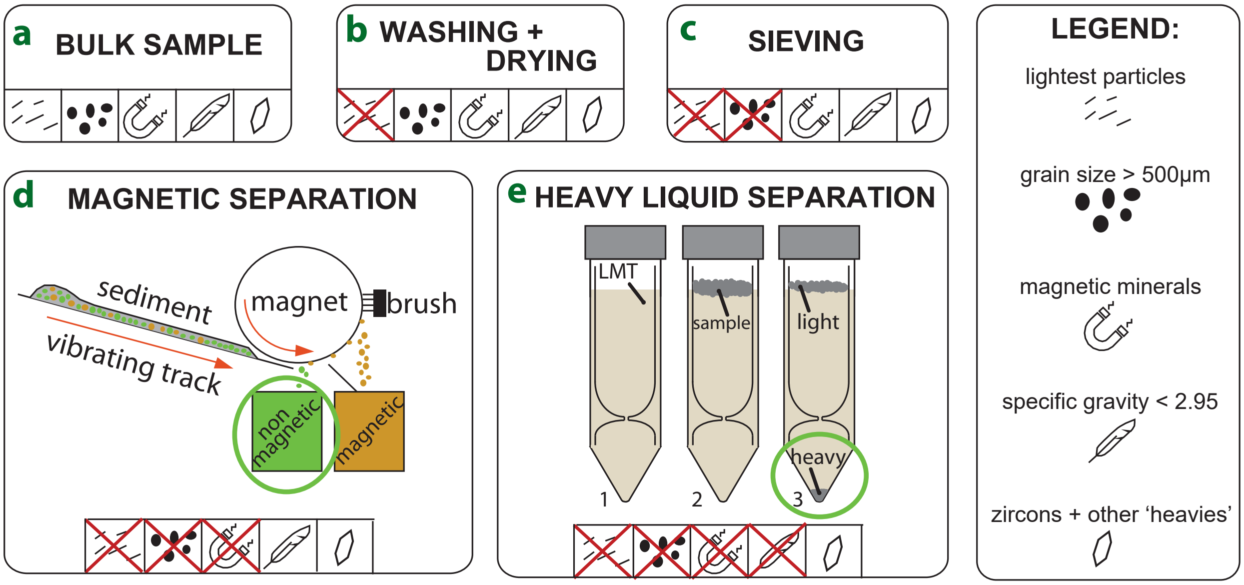

Figure 3.1: Diagram showing the different mineral separation steps, in sequential order from (a) to (e). The red crosses indicate the mineral fractions (legend on the right-hand side) that are progressively removed from each sample. (a) Initial sample. (b) The lightest particles are removed through washing. (c) a mesh 500μm sieve is used to remove the coarser particles. (d) A magnetic separator is used to remove the magnetic fraction. (e) Lithium metatungstate (LMT) is used to remove the light fraction with densities ≤ 2.95g/cm^3. Note: the green circles in Figs. d and e indicate the sample fraction which is retained and used for further processing.

3.1.2 Magnetic separation

Besides zircons, there are other minerals that have a high density, such as Fe-bearing minerals (specific gravity (SG) comparable or higher than zircons). Zircons, however, have low magnetic susceptibility. Hence, to rid the samples from magnetic minerals, a Carpco (Model MIH-13-111-5) high-intensity induced roll magnetic separator was employed. The sample was sprinkled across a vibrating track which progressively moved the sample closer to a rotating magnet. The non-magnetic fraction (containing the zircons), was not attracted by the magnet and would fall down into a crucible through a slit. The magnetic fraction, (without zircons) would be picked up by the rotating magnet and brushed off into a second crucible (see Fig. 3.1d).

3.1.3 Heavy liquid separation

With the removal of the magnetic fraction, most common minerals have a specific gravity of less than 3.0, while zircons have a significantly higher SG of ∼4.7 (e.g., Mungchamnankit et al. [2008]). The heavy liquid used for this study is lithium metatungstate (LMT). This is a non-toxic liquid, soluble in water and with SG of 2.95. For heavy liquid separation, a glass insert was placed in a 50 mL Falcon test tube. Then ∼40 mL of LMT were added into the test tube (see 3.1e). Secondly, part of the non-magnetic fraction (2 to 5 mL) was poured inside the test tube. The mixture of sample and LMT was stirred and centrifuged three times (20 seconds at 1000 revolutions per minute each time), with the sample mixed in between. Since LMT has a very high viscosity, heavy particles take a long time to settle as predicted by Stokes law: the higher the viscosity of the fluid, the lower the terminal velocity of a particle in that fluid. For this reason, the test tubes were left overnight. After a night for settling (see Fig. 3.1e), a 6 mm knitting needle was inserted to stop the flow of the light fraction through the neck of the insert during removal of the glass insert. The isolated heavy fraction was washed repeatedly with Milli-Q water to remove the LMT residue.

3.2 U-Pb CA-ID-TIMS

There are different zircon dating techniques commonly used today. In situ techniques, also known as spot analyses, such as laser ablation inductively coupled mass spectrometry (LA-ICP-MS) and secondary ion mass spectrometry (SIMS), are semi-invasive techniques, as only a small portion of the mineral is damaged. These types of analyses are rapid, and dates can be generated in minutes. Nevertheless, they can only achieve precision levels of ±5-8% for one spot analysis and ±1% for a group of analyses (e.g., Schmitz and Kuiper [2013]). Another widely used dating technique is CA-ID-TIMS. This method involves the dissolution of the whole zircon grain and the analysis requires hours (and 4-5 days of prepartory work in the clean laboratory prior to mass spectrometry). Nevertheless, it can achieve ≤0.1% precision for a single crystal analysis, and ±0.03% precision for a population of analyses (Schmitz and Kuiper [2013]). Time scale work requires this level of precision, especially when the goal is determining the order, causality or rates of events that can occur very rapidly (i.e., mass exctinctions, glaciations, C cycle perturbations). Thus, U-Pb zircon dating by CA-ID-TIMS is most suitable for this study.

With U-Pb dating of zircon, the major and most common problem is Pb loss, wherein the zircon loses Pb after its formation and results in an age younger than its crystallization. Before chemical abrasion, this problem was addressed by removing the outer part of zircon grains (thought to be the region most susceptible to alteration and exchange with the external environment) through an air abrasion technique, which significantly improved the achievable age accuracy by eliminating over 90% of Pb loss areas (Krogh [1982]). The modern technique to address Pb loss, chemical abrasion, is even more effective. Chemical abrasion consists of the pre-treatment (prior to ID-TIMS) of zircons via annealing and partial dissolution (Mattinson [2005]). Annealing is a high temperature treatment that repairs the lattice radiation damage of zircons. Zircons are heated to 900°C for ∼48 hours, which repairs (anneals) lattice radiation damage in the crystal structure. Chemical abrasion (CA) is a leaching procedure in which the zircon areas that have experienced Pb loss are preferentially dissolved (Mattinson [2005]).

3.2.1 Pre-treatments: annealing and chemical abrasion

After annealing, zircons were identified and isolated from each sample under an optical microscope. Detrital zircons, likely introduced during field sampling of the bentonite from surrounding sedimentary strata, are recognizable due to their rounded edges and are not rel-

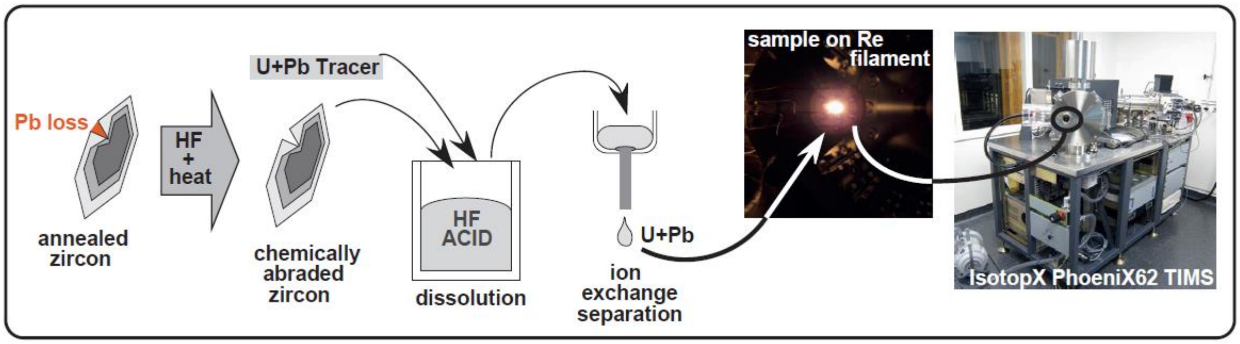

Figure 3.2: Diagram showing the workflow of the CA-ID-TIMS method. Edited from Schoene et al. [2010].

evant for this study. Only euhedral zircons, which suggest a volcanic origin, are suitable for this work. Therefore, only the samples that contain euhedral zircons (three from Anticosti and one from the Siljan district) were processed further. These samples are: MC-17-1:3.5, MC-17-2:1.4 and SR-17-2:0.4 and the Boda bentonite.

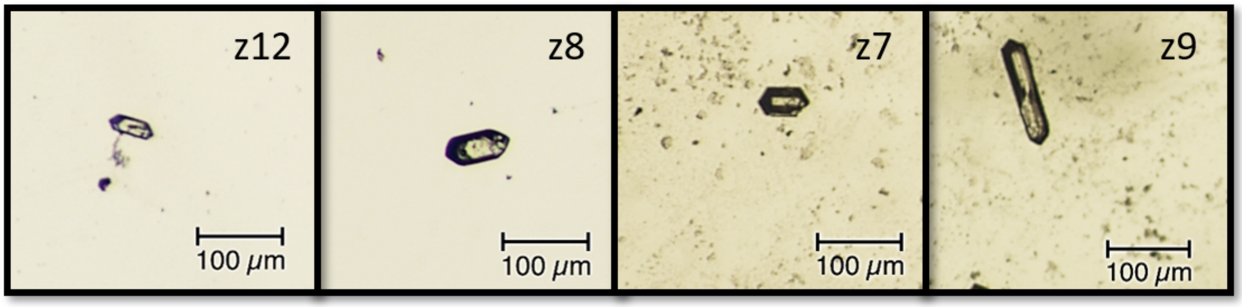

Figure 3.3: These micrographs show some of the zircons that were hand-picked and processed (optical microscope, polarized light). z12 and z8 are from sample MC-17-2:1.4; z7 and z9 are from the Boda bentonite.

Chemical abrasion and mass spectrometry were carried out in the Princeton Radiogenic Isotope Laboratory. Single zircon crystals were hand-picked (see Fig. 3.3) from each of the euhedral zircon-bearing samples with the aid of an optical microscope and fine tweezers. A total of 22 grains were picked from sample MC-17-2:1.4, five were picked from MC-17-1:3.5, 15 from SR-17-2:-0.4 and 14 from the Boda bentonite. Each zircon was placed in a Teflon beaker that had previously been thoroughly cleaned with ethanol. The beakers were moved to a clean laboratory and each zircon was then transferred into a 200 μl Savillex Teflon μcapsule together with blank-checked hydrofluoric acid (HF) and nitric acid (HNO_3). Blank refers to Pb blank, i.e., contamination Pb introduced while processing the sample (Mattinson [2013]), and blank-checked solutions contain $\leq$ 0.1 picogram (pg) of Pb per gram of acid. The μcapsules were then placed in a Parr bomb acid digestion vessel which was put in an oven at 185°C for 12 hours. After this leaching treatment, the zircon areas that had experienced Pb loss had been dissolved (Fig. 3.2).

After leaching, the μcapsules were extracted from the digestion vessel and the zircons were then rinsed repeatedly, following a series of steps. Only blank-checked reagents are used for rinsing. First, the solution inside each μcapsule (containing the leachate from the zircon) was removed with a piston pipette set to 180μL, with care not to remove the chemically-abraded, still-intact zircon crystal. Successively, the capsules were fluxed with 6N hydrochloric acid (HCl) $\rightarrow$ MQ water $\rightarrow$ 6N HCl $\rightarrow$ 4 drops MQ water, ending with 4 drops HF. The μcapsules, with caps on, were then left on a hot plate for 3 hours. One more round of rinses was carried out: MQ $\rightarrow$ 6 N HCl $\rightarrow$ MQ $\rightarrow$ 6N HCl. The μcapsules were left, with caps on, on a hot plate overnight. The next morning, another rinse cycle (MQ $\rightarrow$ HF $\rightarrow$ MQ $\rightarrow$ HF) was carried out, ending with the removal of the acid (leaving only one drop in the μcapsule, to make sure the zircon was not removed as well).

3.2.2 ID-TIMS

After the zircons have been annealed and chemically abraded, they must be completely dissolved in a solution spiked with an EARTHTIME tracer (Condon et al. [2015]. Pb and U are measured separately in the mass spectrometer. The number of moles of Pb and U must be calculated in order to solve equations 3.3 and 3.4 for time. To do this, we need to mix our ^{206}Pb and ^{207}Pb. with a tracer solution of known composition to solve for moles of ^{206}Pb and ^{207}Pb. Different laboratories traditionally used their own tracer solutions, making intercalibration and result comparison challenging. This situation has changed since the EARTHTIME initiative (e.g., Bowring et al. [2005]). This initiative has addressed intercalibration issues and has fostered a more cooperative community of geoscientists from different disciplines that come together with the goal to improve geochronology (e.g., Bowring et al. [2005], Schmitz and Kuiper [2013], Condon and Schmitz [2013]). With this object in mind, standardized tracer solutions[3] for U-Pb ID-TIMS that can be traced back to physical units (SI) have been prepared and are now used internationally (Condon et al. [2015]).

The tracer used for this project[4] is called ET2535 and it contains the synthetic ^{202}Pb, ^{205}Pb, and ^{233}U as well as the naturally occurring ^{235}U (e.g., Condon et al. [2015]). At this stage, each zircon was in a μcapsule with one drop of blank-checked HF. A measured mass of ET2535 solution was added to the μcapsule, along with four drops of blank-checked HF and one of HNO_3. The μcapsules were put back in the Parr bomb, which was placed in an oven at 210°C for 48 hours to let the zircons dissolve completely.

After dissolution, the μcapsules were taken out of the digestion vessel and placed on a hot plate to let the HF evaporate completely. Then 3 drops of 6N HCl were added to the dried μcapsules, which were placed back in the Parr bomb and the oven at 185°C for 12 hours. The digestion vessel was taken out of the oven and brought back to the clean lab. The μcapsules were placed on a hot plate to dry. Then 2 drops of 3N HCl were added and the μcapsules were placed back on the hot plate for about 20 minutes as the final step before ion exchange chromoatography, after Krogh [1973].

---

[3] The composition of the EARTHTIME tracers used in this study is included in the appendix, Table A.1.

[4] Exceptions: a different tracer was used for 4 zircons from the Boda bentonite (z2, z3, z4, z5) and for 2 zircons from MC-17-2:-1.4 (z3a, z8a). These were spiked with ET525 (EARTHTIME ^{205}U ^{233}Pb ^{235}Pb).

Each chromatography column employed was conditioned with 8 drops of 3N HCl and each sample (containing the dissolved zircon and HCl) was poured into a column (note: columns were previously cleaned thoroughly with cycles of MQ water and 6N HCL). Blank-checked 3N HCl was added to the columns and a vial was placed under each column to collect all dissolved elements other than U and Pb. Then a Savillex beaker was placed under each column instead. 8 drops of blank-checked 6N HCl were added to the each column to elute Pb. Afterwards, 10 drops of blank-checked MQ water were added to elute U. Once the U had eluted as well, one drop of blank-checked phosphoric acid (H_3PO_4) was added and the beakers were placed on a hot plate to dry.

U-Pb measurements were performed on an IsotopX Phoenix62 thermal ionization mass spectrometer at Princeton University. Each sample was placed on a single, outgassed rhenium (Re) filament in a Si-gel emitter (Gerstenberger and Haase [1997]). Under vacuum, the filament was heated up in a magnetic sector of the mass spectrometer in order to ionize Pb and U (which predominantly ionize as Pb^+ and $UO_2{}^+$) and accelerate them by applying a $\sim$8-10 kV electric potential (e.g., Schoene et al. [2010], Schaefer [2016]). The ion beam, traveling through a magnetic sector of the mass spectrometer, diverges into separate beams according to their mass (e.g., Faure and Mensing [2005]). Pb is measured first at a lower filament temperature and in dynamic mode on an axial ion-counting Daly photomultiplier. U was measured second in static mode on Faraday cups on $10^{12}\Omega$ resistors as UO_2. $^{233}UO_2$ and $^{235}UO_2$ were corrected for an oxygen isotopic composition of 0.002055 (Condon et al. [2015]). Because $^{18}O/^{16}O$ typically grows at the beginning of an analysis before stabilizing, early blocks of data are not included in final data reduction. Crucially, the known amount of ^{202}Pb, ^{205}Pb, ^{233}U and ^{235}U present in each sample (from the spike solution of known mass added to each dated zircon) allows for determination of the mass (in moles) of ^{206}Pb, ^{238}U,

^{207}Pb and ^{235}U, and hence the ^{206}Pb/^{238}U and ^{207}Pb/^{235}U ages.

3.2.3 Further investigation on MC-17-2:1.4

Supplementaty investigations were carried out for sample MC-17-2:1.4; namely petrographic observations and bulk geochemistry analysis. The light fraction (from heavy liquid separation) was observed through an optical microscope to detect volcanic phenocrysts. For the geochemical analysis, a pulverized whole-rock powder ($\geq$5g) of the sample was prepared and submitted to Actlabs (Ontario), where it was dissolved in a borate flux and then diluted in aqueous nitric acid. Inductively coupled plasma optical emission spectrometry (ICP-OES) and mass spectroscopy (ICP-MS) were used to quantify major and trace elements in the resulting solution.

Chapter 4

Results

Fifteen samples were collected from the field, but 11 were not dated via CA-ID-TIMS, because euhedral zircons were not found after heavy liquid separation. Four samples were dated, three from Canada and one from Sweden. Each contained zircons with euhedral habit (which suggests a volcanic origin). A total of 56 zircons were picked from the 4 samples, and were processed to produce isotopic dates. The extended version of the results for each of the dated potential bentonite samples, including all the dates, compositions and isotopic ratios, are reported in the appendix (Tables A.2, A.3, A.4, A.5). Samples MC-17-2:1.4 and Boda, described in section 4.1, successfully provided a cluster of robust and concordant dates. These dates have been used to determine an age for each of the two bentonite samples. An age consists of a number (obtained by solving equation 3.2 for time) associated with a geological event: the deposition of an ashfall in this case. Samples MC-17-1:3.5 and SR-17-2:-0.4, display dates that range from 2627 Ma to 449.24 Ma. Unlike MC-17-2:1.4 and Boda, a clear plateau, with multiple zircons of overlapping dates, was not apparent in these samples.

For each zircon analyzed, two ages have been produced: one using ^{206}Pb/^{238}U, and one using ^{207}Pb/^{235}U. The results have been displayed using Wetherill Concordia plots (Wetherill

[1956]) and weighted means (e.g., see Figs. 4.2 and 4.6). Concordia diagrams plot predicted U-Pb isotopic compositions for a closed system of a given age, t. When an analysis overlaps (considering its error) with this thereotical curve, the dated mineral is considered to represent a closed system with a robust age. Analyses that fall off concordia suggest open system behavior, such as Pb loss. The age for the two successfully dated bentonite samples was determined using weighted mean averages. The mean squared weighted deviation (MSWD) was the statistical analysis adopted to determine the goodness of the fit of this model. The expected MWSD value should be ∼1 when the deviations from the regression age line are within analytical error (Wendt and Carl [1991]).

A thorium correction has been applied to the results displayed in Figs. 4.2 and 4.6. Zircon is a Th-poor mineral. Thus, when zircon crystallizes, it is out of equilibrium with Th from the parent magma, i.e. Th-U fractionation between zircon and magma (f) is ≤ 1.

$$f = \frac{(Th/U)_{zircon}}{(Th/U)_{magma}} \tag{4.1}$$

^{230}Th is one isotope of Th, which is part of the ^{238}U decay chain (half-life of ∼75 kyr). Due to Th incompatibility, zircons will be depleted in ^{230}Th during crystallization. The end result of Th disequilibrium is that the ^{206}Pb/^{238}U age is too young, because less ^{230}Th means less ^{206}Pb ultimately made. Therefore, we calculate the original Th/U of the zircon directly. Th contents are calculated from radiogenic ^{208}Pb and ^{230}Th-corrected ^{206}Pb/^{238}U date of the sample, assuming concordance between U-Pb and Th-Pb systems (these ratios are in the data tables included in the appendix). It is also assumed that Th/U of the magma is 2.8. But importantly, for zircon, there is a hard absolute limit for how much this correction can change the age (because zircons have f values ≤ 1, rather than ≥ 1). If there is no Th in the zircon (Th/U = 0), the age will be too young by ∼75 kyr. Thus, the correction is important for young zircon, but less so for Mesozoic zircons or older (see Fig. 4 from Schärer [1984]).

The CA-ID-TIMS results, corrections and statistical data were processed using U-Pb Redux, which is a software that standardizes data processing protocols, hence enabling robust interlaboratory comparisons (Bowring et al. [2011]).

4.1 Samples MC-17-2:1.4 and Boda

This section presents the results for samples MC-17-2:1.4 (from Anticosti Island, Canada) and for the Boda bentonite (Siljan district, Sweden). Both of these samples show a cluster of Late Ordovician dates (4.2 and 4.6). Tables with complete data are included in the appendix (Tables A.2, A.3).

MC 17 2 1.4

We processed a total of 22 zircons, four of which were rejected (one due to unacceptably high Pb blank, and three lost during procedures prior to mass spectrometry). Of the 18 zircons successfully dated, one is Proterozoic (1096 Ma). 13 zircons range from Lower to Middle Ordovician (461.36 Ma to 475.23 Ma, see Fig. 4.1). The youngest 4 grains overlap with their uncertainties and have a weighted mean is 443.61±0.18/0.21/0.52. All uncertainties are at the 2σ level. The first, 0.18, is the analytical uncertainty; the second, 0.21, also includes tracer calibration; the third, 0.52, also includes decay constant uncertainties (e.g., Schoene [2014]). The MSWD on this group of dates is 0.72, thus indicating that a weighted mean is a good fit for these data. These four zircon also overlap with two zircons previously dated at Princeton from this same Anticosti bentonite layer. The weighted mean of these six zircons is 443.61±0.17/0.21/0.52, with MSWD = 0.61 (see Fig. 4.1, 4.2).

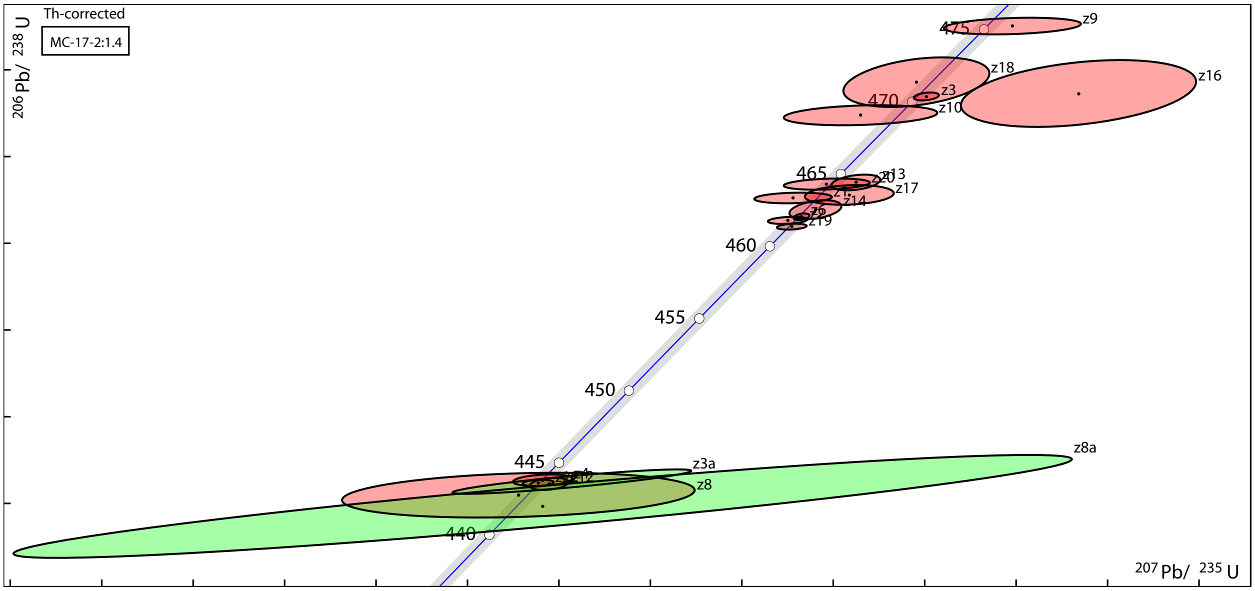

Figure 4.1: Concordia plot (^{206}Pb/^{238}U ratio versus ^{207}Pb/^{235}U ratio) of MC-17-2:1.4. The blue line is the concordia curve. The small black dots represent measured U-Pb isotopic ratios and the colored ellipses around each of those dots represent measurement uncertainty. The red are the new analyses produced, while the green color indicates the two older analyses (z3a, z8a). Each ellipsis is labeled (e.g.: z1, z2, etc.) with the name assigned to the measured zircon. All the accepted zircon dates are included, except for z21, which is >1000Ma.

Phenocrysts (Fig. 4.3) were identified during petrographic observation of this sample's light fraction (derived from LMT separation, see section 3.1), phenocrysts were identified (see Fig. 4.3). The bentoninite's bulk geochemical composition (see Table A.6 for extended data) falls withing trachyandesitic domain when plotted on the Winchester and Floyd, 1977 diagram (see Fig. 4.4). This volcanic rock classification diagram uses immobile trace elements, and is ideal for altered rocks (such as bentonites). The composition of MC-17-2:1.4 is comparable with other Upper Ordovician Laurentian bentonites, such as the Russell Bed bentonite (Sharma et al. [2005], see Fig. 4.4), from the Billings Fmt, eastern Ontario (Canada).

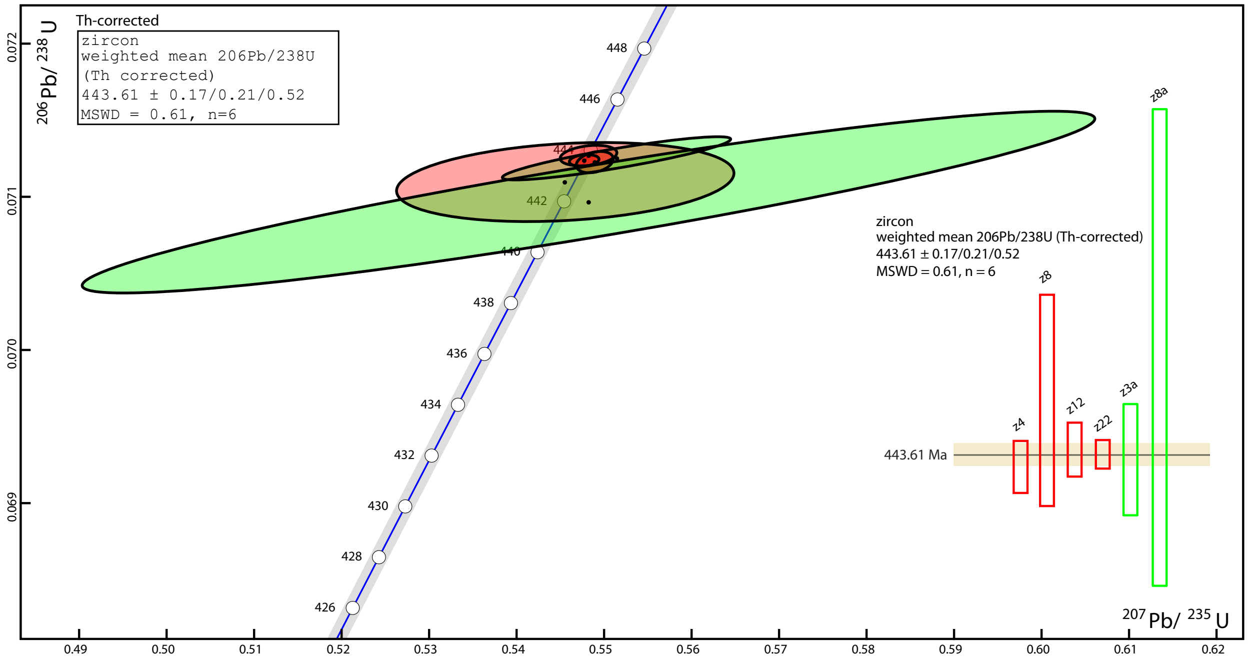

Figure 4.2: Concordia plot (^{206}Pb/^{238}U ratio versus ^{207}Pb/^{235}U ratio) of the MC-17-2:1.4 sample. This is a close up, which highlights the dates the ages which have been used in the weighted mean. The blue line is the concordia curve. The small black dots represent measured U-Pb isotopic ratios and the colored ellipses around each of those dots represent measurement uncertainty. The red are the new analyses produced, while the green color indicates the two older analyses. The bottom right of the figure illustrates the same results displayed by the weighted mean of their ^{206}Pb/^{238}U, in the top left.

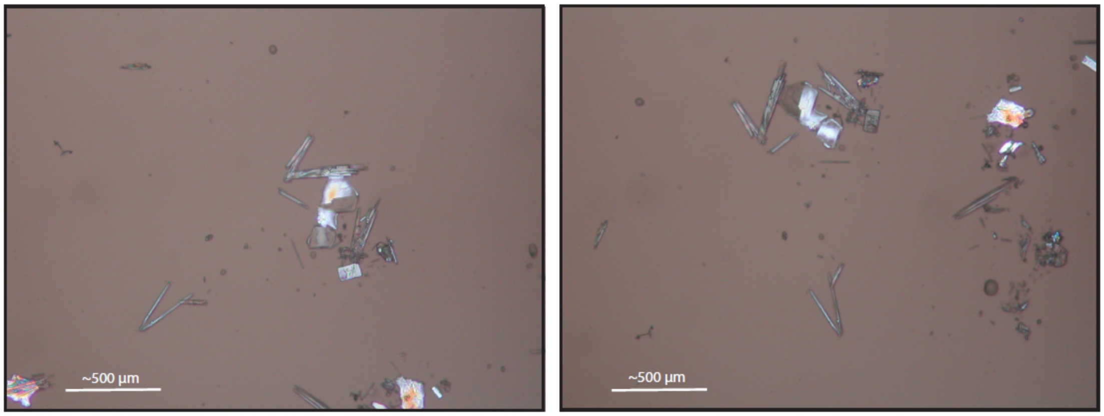

Figure 4.3: Micrographs of phenocrysts from sample MC-17-2:1.4, taken with an optical microscope, cross-polarized light. Note the twinning of the quasi-hexagonal crystal (feldspar?).

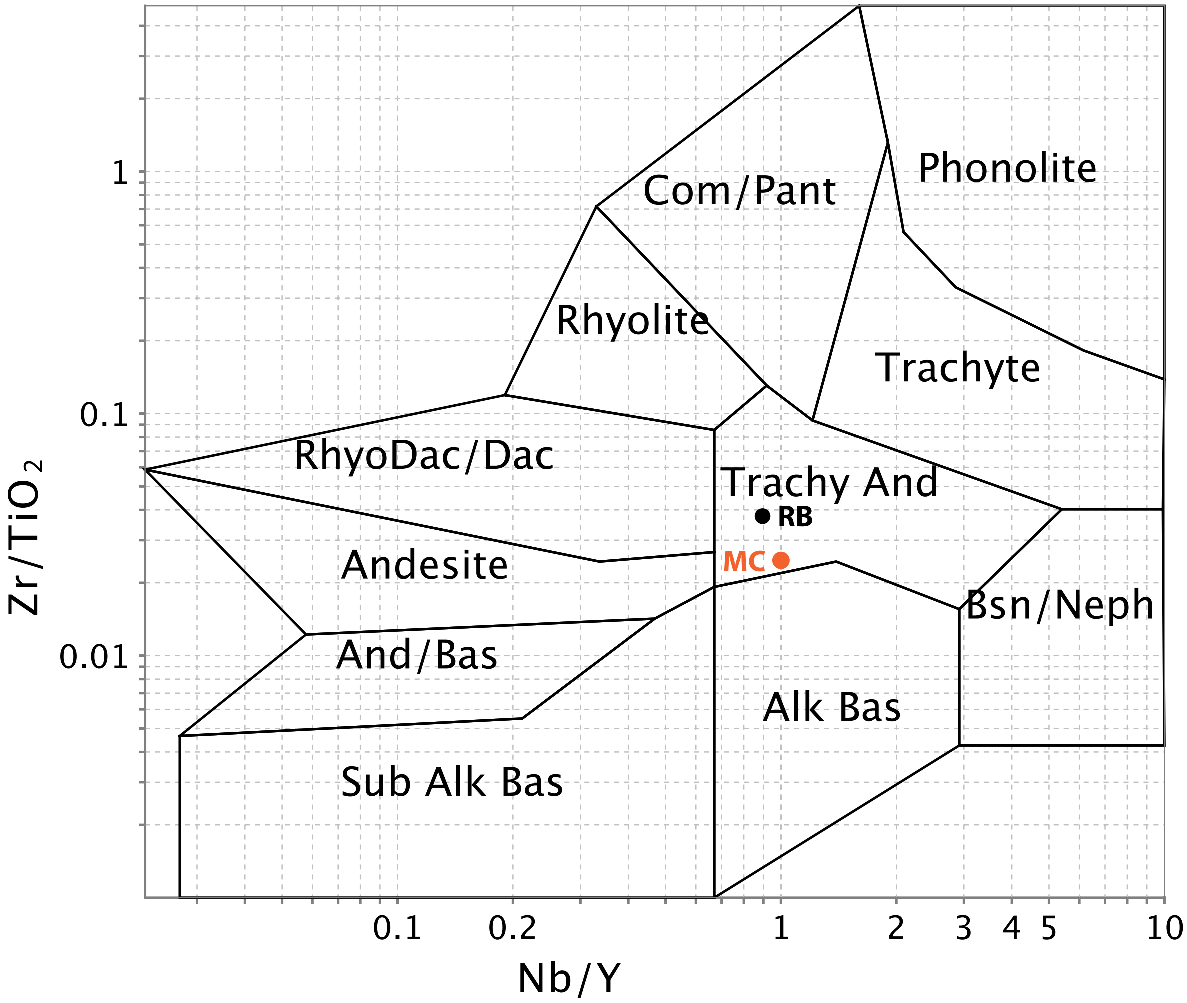

Figure 4.4: The bulk composition of sample MC-17-2:1.4 (trachyandesitic) is indicated by a orange dot (labeled MC) in this volcanic rock classification plot, Winchester and Floyd, 1977. The composition of the Russell Bed bentonite (black dot, labeled RB), from eastern Canada (Sharma et al. [2005]), is also plotted for comparison.

Boda bentonite

A total of 14 zircons were analyzed and 13 dates are presented here, with one rejected due to high Pb blank. Of the 13 zircons that were accepted, eight form a robust age plateau (see Fig. 4.5, 4.6). The weighted mean of the dates is 443.28±0.10/0.15/0.50 (analytical uncertainty/analytical + tracer/analytical + tracer + decay constant). All uncertainties are at the 2σ level. The MSWD for this population of zircons is 0.82. Three of the dated zircons are younger than this age plateau and two are older.

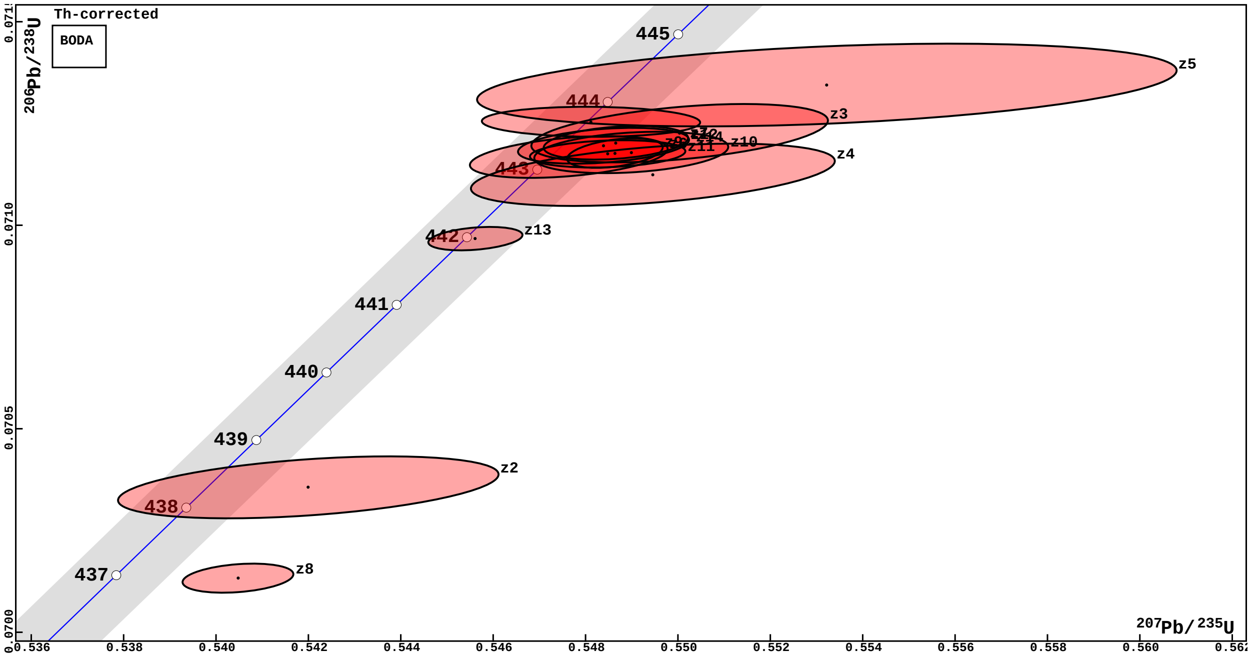

Figure 4.5: Concordia plot ($^{206}Pb/^{238}U$ ratio versus $^{207}Pb/^{235}U$ ratio) of the Boda bentonite sample. The blue line is the concordia curve. The small black dots represent measured U-Pb isotopic ratios and the ellipses around each of those dots represent the uncertainty. Each ellipsis is labeled (eg: z1, z2, etc.) with the name assigned to the measured zircon. All zircon dates are included.

4.2 Samples MC-17-1:3.5 and SR-17-2:-0.4

The dates from these two samples were very dispersed. Five zircons were dated for MC-17-1:3.5 (range of 444.72 to 2627 Ma, see Fig. 4.7) and 15 zircons were dated for SR-17-2:0.4 (range of 449.30 to 2653 Ma, see Fig. 4.8). As opposed to the two samples presented in the previous section, it was impossible to resolve unambiguous and meaningful ages from the data of these two samples. Further investigation would be required to determine potentially an age for these two samples, if one is present. Sample MC-17-1:3.5 looks particularly promising, as it has one zircon (z4) which is 444.72 Ma (see Fig. 4.7). Sample MC-17-

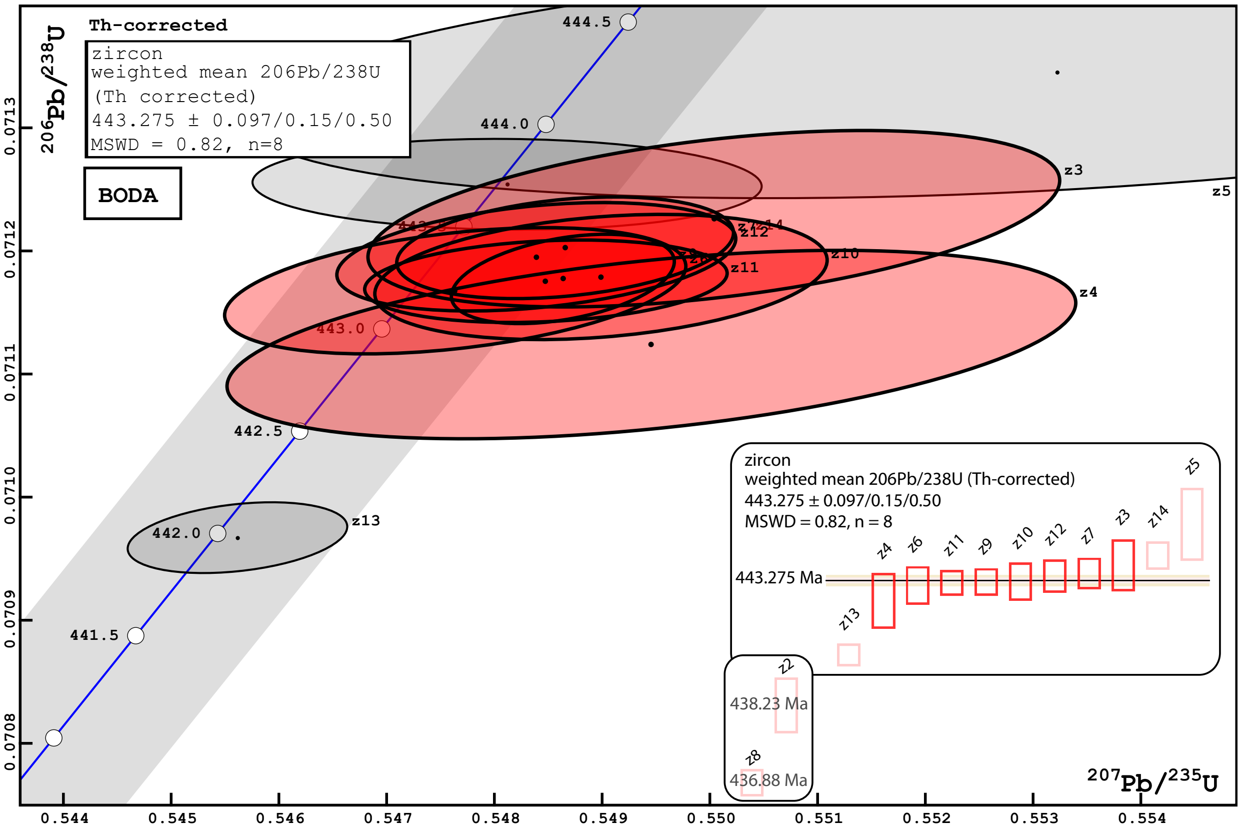

Figure 4.6: Concordia plot (^{206}Pb/^{238}U ratio versus ^{207}Pb/^{235}U ratio) of the Boda bentonite sample. This is a close up which highlights the dates that have been used for the weighted mean. The blue line is the concordia curve. The small black dots represent measured U-Pb isotopic ratios and the ellipses around each of those dots represent the uncertainty. Note that only the significantly overlapping ellipses have been highlighted in red. Each ellipsis is labeled (eg: z1, z2, etc.) with the name assigned to the measured zircon. The box on the bottom right of the figure illustrates the same results dispayed by their weighted mean in the top left.

1:3.5 was collected just ∼2m above MC-17-2:1.4 (see Fig. 2.4), therefore it is unequivocally younger (MC-17-2:1.4 is 443.61±0.17). Tables with complete data for samples MC-17-1:3.5 and SR-17-2:-0.4 are included in the appendix (see Figs. 4.7, 4.8 and Tables A.4, A.5).

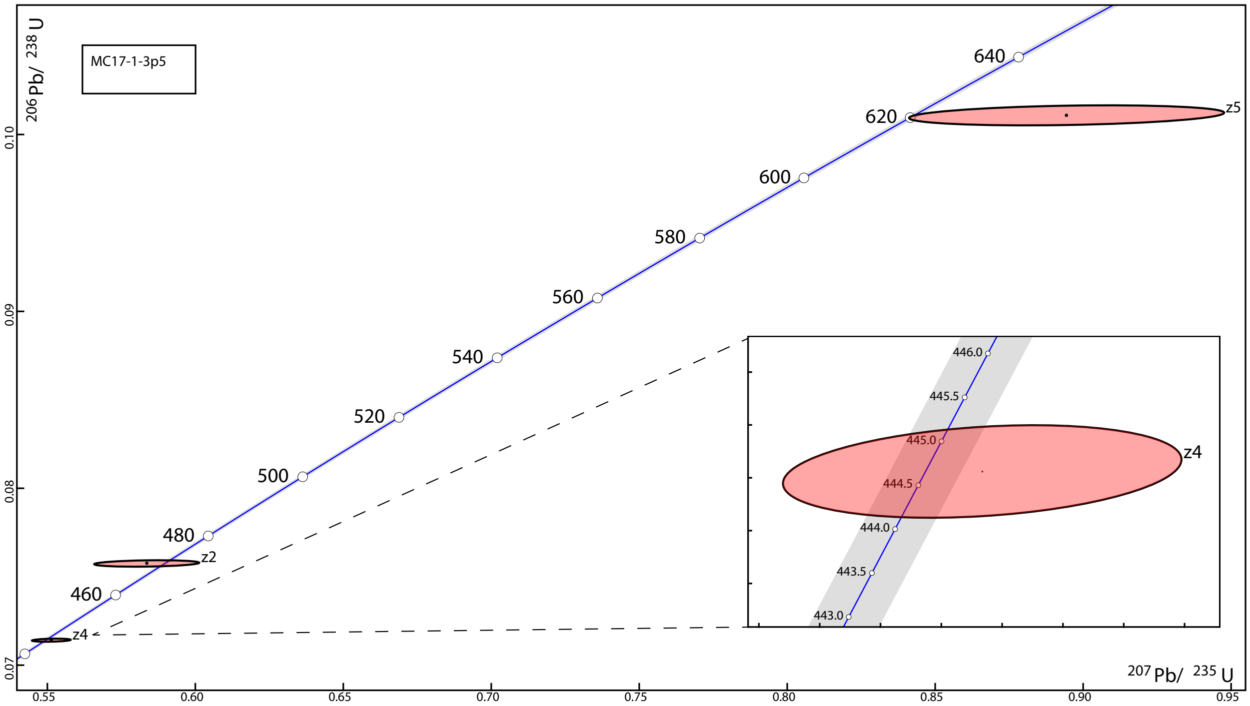

Figure 4.7: Concordia plot (^{206}Pb/^{238}U ratio versus ^{207}Pb/^{235}U ratio) of MC-17-1:3.5. The blue line is the concordia curve. The small black dots represent measured U-Pb isotopic ratios and the ellipses around each of those dots represent the uncertainty. Each ellipsis is labeled (eg: z1, z2, etc.) with the name assigned to the measured zircon. All zircon dates are included. All accepted zircon dates are shown, except for z1 and z3, which are >1000Ma. Insert at bottom right shows z4 more closely.

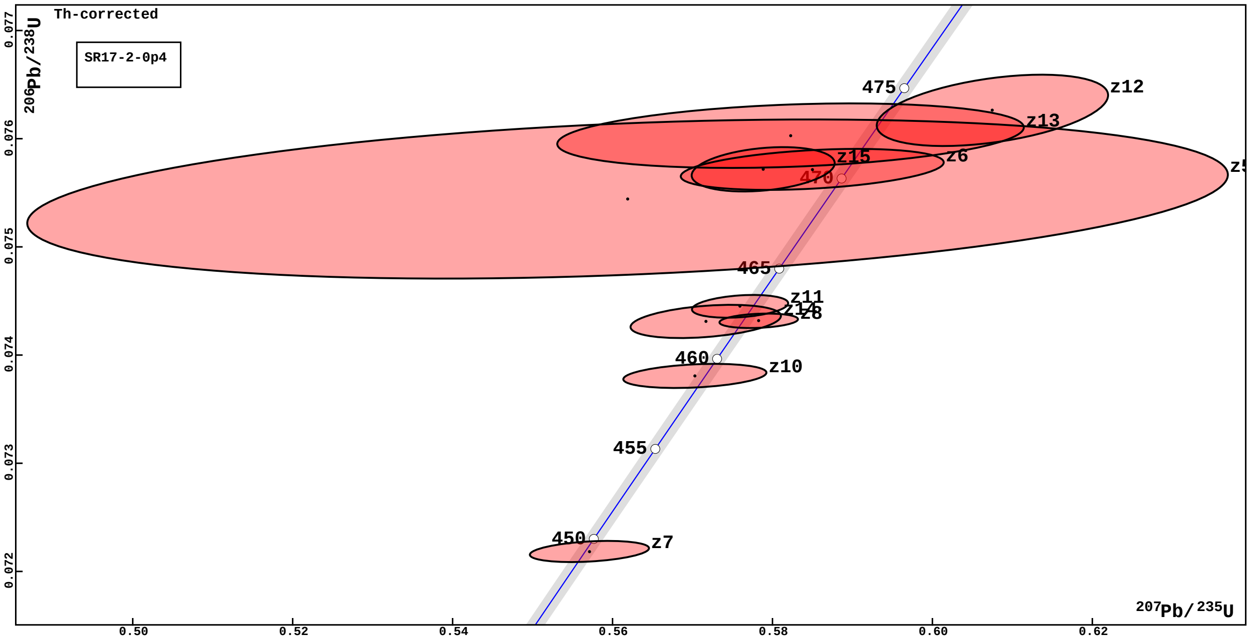

Figure 4.8: Concordia plot (^{206}Pb/^{238}U ratio versus ^{207}Pb/^{235}U ratio) of SR-17-2:-0.4. The blue line is the concordia curve. The small black dots represent measured U-Pb isotopic ratios and the ellipses around each of those dots represent the uncertainty. Each ellipsis is labeled (eg: z1, z2, etc.) with the name assigned to the measured zircon. All accepted zircon dates are included, except for z1, z2, z3, z4 and z9, which are >700Ma.

Chapter 5

Discussion

In this chapter, the U-Pb results will be discussed and their possible applications will be explored. Section 5.1 concerns the interpretation of the U-Pb dates obtained in this study. The following sections, illustrate the type of applications that can derive from this type of data. Specifically, section 5.2 describes how to make an age model for the duration of the HICE by combining radiometric ages with C isotope stratigraphy. Section 5.3 explains how to create a simple carbon model that can illustrate a potential C cycle perturbation manifest in the HICE, which has been commonly linked to end-Ordovician glaciation and mass extinction. Assumptions are required for each that are difficult to test, but both the age model and the carbon model are solely used to help convey the potential applications of our results and of radiometric ages in general.

5.1 From dates to ages: interpreting U-Pb ID-TIMS results

Volcanic eruptions can be considered as geologically instantaneous events. For this reason, dating bentonites is an important tool for the calibration of geologic time. The objective of dating a bentonite sample is to deduce the age of the volcanic eruption which created it. In an ideal scenario, all zircons present crystallized at the same time and simply date the ashfall event. In reality, date spectra found in bentonites are always more complex, because not all zircons are autocrysts. It is common to find antecrysts (formed from protracted zircon growth within the magma chamber before eruption) or xenocrysts (incorporated from country rock during eruption), as well as detrital grains from sediment contamination (e.g., Corfu [2013], Miller et al. [2007], Tucker et al. [1990]). Furthermore, some zircon crystals may be affected by Pb loss (e.g., Schoene et al. [2010]). Thus, the preferred approach (e.g., MacLennan et al. [2018], Schoene et al. [2010]) is to identify the youngest, robust age possible, and this serves as the best model for eruption age. A robust age can be determined when there are multiple overlapping zircon dates that form an age plateau.

Multiple, overlapping concordant dates (found both in MC-17-2:1.4 and in the Boda sample) suggest that the zircons are autocrysts, meaning that they formed within the youngest magma pulse and thus closest to the actual eruption age (e.g., Miller et al. [2007]). Their weighted mean, 443.61±0.17/0.21/0.52 Ma and 443.28±0.10/0.15/0.50 Ma respectively, serves as the best model for the eruptive age of each ashfall event. Weighted means are often interpreted as the best age estimate (e.g., Schoene [2014]). This assumption is most valid for older bentonite ages, given the precision of individual analyses (200-400 kyr for the end-Ordovician). It becomes more problematic for young ashes, as zircons do not crystallize instantaneously.

Sample MC-17-2:1.4 produced a cluster of six concordant dates with overlapping uncertainties. The one Proterozoic grain from this sample (1096 Ma) is interpreted as a detrital grain. There are also 13 dates that are older than the six plateau zircons, ranging from Lower to Middle Ordovician (see Fig. 4.1). The zircons that produced these dates could be interpreted as xenocrysts that became incorporated into the ashfall during eruption.

The sample was collected from the Lousy Cove Mbr of the Ellis Bay Fmt and sits ∼8 m below the HICE (see Fig. 2.4). The Lousy Cove Mbr is Katian/Hirnantian (Upper Ordovician age). This is consistent with the interpretation that the 13 dated zircons, which range from Middle to Lower Ordovician age (much older than the Lousy Cove sediments), are xenocrysts. In the field, MC-17-2:1.4 appeared as a ∼6 cm thick conformable bentonite horizon. Despite the complex age spectra from this sample, the volcanic origin of MC-17-2:1.4 is further reinforced by the the presence of phenocrysts (as one would expect from a sample that has volcanic origin) identified during petrographic observations (see Fig. 4.3). Furthermore, the geochemical composition of the bulk sample plots in the trachyandesitic field of the Winchester and Floyd [1977] diagram (see Fig. 4.4). The bulk composition of the sample is consistent with an explosive eruptive style (see Fig. 4.4) and is comparable with other Upper Ordovician Ordovician Laurentian bentonites (e.g., Russel Bed bentonite from the Billings Fmt, eastern Ontario (Canada)).

Euhedral zircons are abundant in the Boda bentonite. Fig. 4.6 shows an age plateau formed by a population of eight zircons. There are three zircons that are resolvably younger compared to this age plateau (see Fig. 4.5), hence the eight plateau zircons could be interpreted as grains that resolvably pre-date the eruption event. Nevertheless, the youngest zircon (z8), is clearly discordant (see Fig. 4.5), while the other two zircons grains do not overlap with any other grain and are here interpreted as a subtle Pb loss (i.e., not all Pb loss affected areas had not been completely removed during the chemical abrasion). This interpretation is not unreasonable, especially considering that subtle lead loss is nearly impossible to detect in U-Pb ages as young as these, because all discordia lines run nearly parallel to the concordia curve for ∼444 Ma crystrallization ages. There are also two zircons that are older than the age plateau that are interpreted as either antecrysts or xenocrysts (see Fig. 4.6).

The Boda bentonite was collected from a karstic void (located just below the HICE peak, see Fig. 2.11). It follows that the Boda bentonite can be considered as a minimum age constraint on the surrounding strata, as cave formation necessarily postdated the deposition of its encasing sediments. Thus, the strata could be older than the age of the Boda bentonite, but not younger. However, it has been suggested that cave formation was very early and coincident with either erosional surface K1 or K2 (Kröger et al. [2015]) further up section (∼10m and ∼19 m above the Boda bentonite sample, see Fig. 2.11). Regardless, the age obtained for the Boda bentonite (443.28±0.10/0.15/0.50 Ma) is younger than the one obtained for MC-17-2:1.4 (443.61±0.17/0.21/0.52 Ma). This ordination is consistent with the fact MC-17-2:1.4 is ∼8 m below the start of the HICE rise, whereas the Boda is either from the HICE maximum (if correlative to K1) or post-dates the excursion (if correlative to K2).

Owing to their stratigraphic contexts, sample MC-17-2:1.4 provides a stronger time constraint than the Boda bentonite, because the former is conformable with strata above and below, whereas the latter is not. Even though there is currently no agreement on the exact position of the Katian-Hirnantian boundary on Anticosti (due to contrasting chemostratigraphic and biostratigraphic interpretations, see section 2.1.2), it is agreed that the Lousy Cove Mbr is Ordovician and not Silurian. The age obtained for the Anticosti sample is 443.61±0.52 Ma (2σ, analytical, tracer calibration and decay constant uncertainties). In the most recently updated chronostratigraphic chart (Cohen et al. [2018]), the O-S boundary is placed at 443.8±1.5 Ma, thus predicting that MC-17-2:1.4 cames from Silurian strata. The age of our sample (indisputably Ordovician) implies that the age of the current O-S boundary is very unlikely to be on the older side of its given uncertainty (see Fig. 5.1).

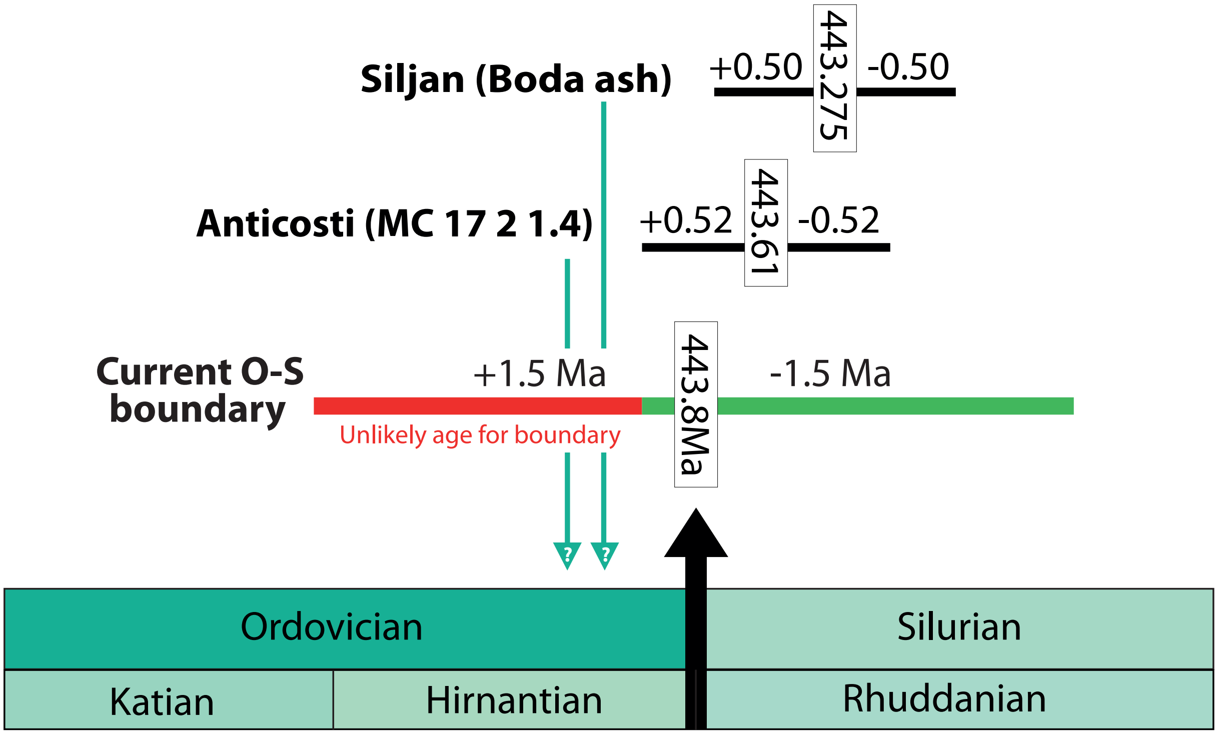

Figure 5.1: This illustration shows a comparison between the two new radiometric ages and the current O-S boundary (Cohen et al. [2018]).

In the future, the other two Anticosti samples that contain zircons with euhedral morphology (MC-17-1:3.5 and SR-17-2:-0.4) could be further investigated to ensure whether or not they are bentonite clays and bear a population of Hirnantian zircons. For this purpose, petrographic observations could be carried out and a faster dating method (such as laser ablation) could be adopted to identify an eruption age zircon population (if one exists).

5.2 How to make an age model

As a demonstration of what can be done with the radiometric ages obtained, the estimation of a minimum duration of the HICE will be used as an example. In other words, a duration which corresponds to the thickness of sediments deposited from pre-excursion δ^{13}C values to peak value (on eastern Anticosti, see Fig. 5.2) is is deduced. The analysis below makes several assumptions. These are subject to revision, especially as new geochronological constraints are developed.

In their global review of the Hirnantian stage, Delabroye and Vecoli [2010], examine the limitations and ongoing conundra of global correlations made with C isotope chemostratigraphy. These include (and are not restricted to) different absolute values of the HICE peaks in different locations. However, the approach chosen here considers the $\delta^{13}C_{carb}$ stratigraphic record to be synchronous (e.g., Kump and Arthur [1999]), hence suitable as a tool for global correlations. It follows that even though a consensus regarding the position of the Hirnantian Stage on Anticosti Island has not been reached, the position selected here is the one suggested by chemostratigraphic studies (e.g., Jones et al. [2011]): that the Hirnantian Stage is confined to the uppermost Ellis Bay Fmt, as shown in Fig. 5.2.

Given the above premises, the $\delta^{13}C_{carb}$ record ($\delta^{13}C$ of carbonate sediments) is used as a correlating tool to project the Boda sample into the eastern Anticosti stratigraphy (see Fig. 2.4 and 5.2). The $\delta^{13}C_{carb}$ data for the Macaire Creek is from [Jones, personal communication, 2018][1]. Here we consider the highest value of this dataset to be the peak of the HICE, although more $\delta^{13}C$ data would be helpful to ensure that the peak of the HICE corresponds with the one selected here and it is not situated higher in the section or truncated by a hiatus (as suggested by Brenchley et al. [2003]). The C isotope chemostratigraphy used for the Siljan district, is from the Osmundsberget 4 & 5 section included in Ebbestad et al. [2015] (Fig. 13) and in Kröger et al. [2015] (Fig 3). As mentioned earlier, the Boda ash comes from a karst pocket, therefore it provides a minimum age constraint on the adjacent strata.

---

[1] The $\delta^{13}C$ curve used in the age model is the same as the one shown in Fig. 2.4 of this manuscript. We do not have data for the very bottom and the very top of the stratigraphic section depicting the lithostratigraphy of the sampling location.

In this model, cave formation is considered coincident with erosional surface K1, which sits at the peak of the HICE (as suggested by Kröger et al. [2015], see Figs. 5.2).

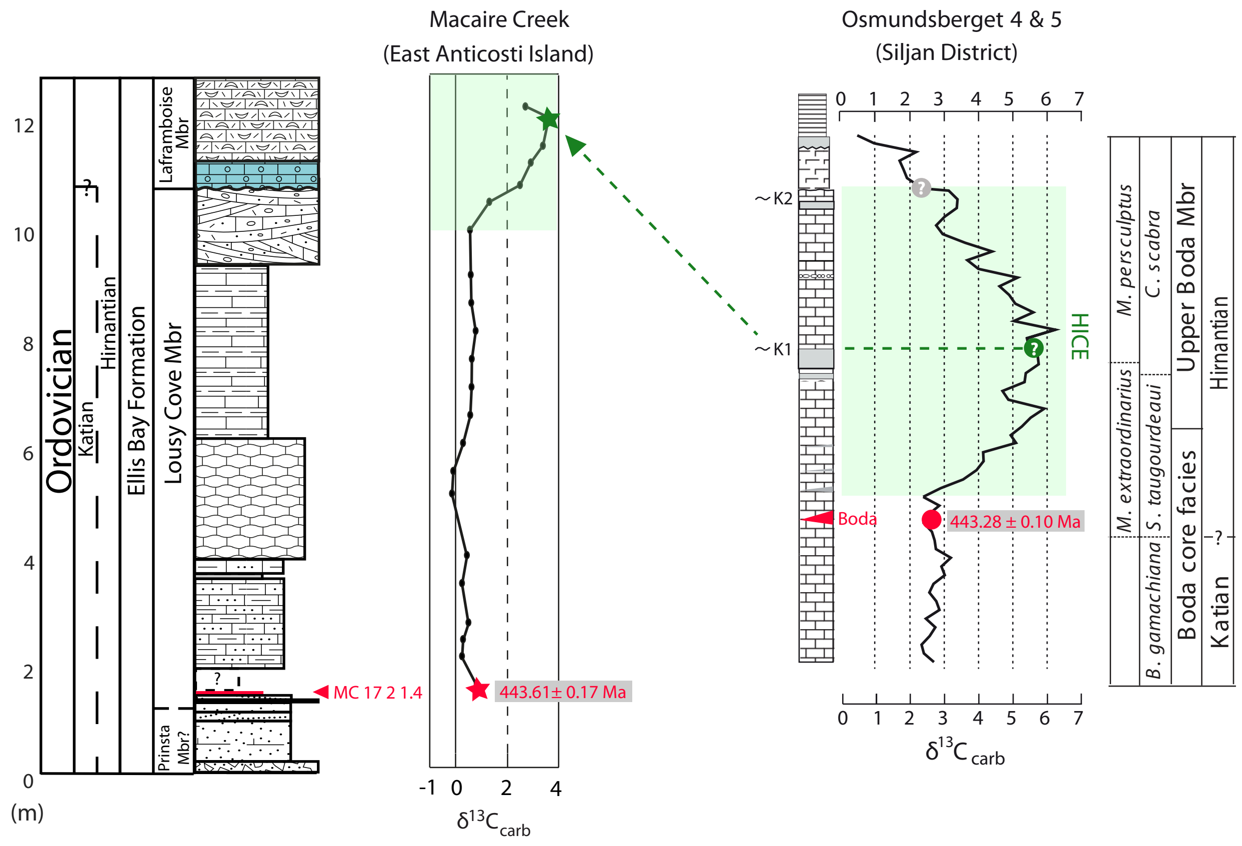

Figure 5.2: This figure shows a possible correlation scheme between eastern Anticosti and the Siljan district. The projection of the Boda bentonite into the eastern Anticosti stratigraphy is shown by the green dashed arrow. The Osmundsberget 4 & 5 lithostratigraphy, chemostratigraphy and biostratigraphy is from Ebbestad et al. [2015], (Fig. 13).

To calculate a duration for the HICE, the first step was to further refine the two probability distributions for the Boda and the MC-17-2:1.4 ages, starting with the weighted mean ages for each as an initial model. Since the purpose of this model is to calculate durations, and both bentonites have zircon U-Pb ages produced with EARTHTIME spikes, only the analytical uncertainty is relevant. From the two age distributions, a set of 10^5 date pairs are drawn. Each pair of randomly selected values was retained only if stratigraphically valid

—in other words, only if the age from sample MC-17-2:1.4 (stratigraphically lower compared to the Boda, hence older) was greater than the age for the Boda sample. The two refined age distributions are displayed in Fig. 5.3. The two new age distributions are nearly identical to their priors; and their respective mean values do not change. This result arises because the initial age models for both bentonites do not overlap at the two sigma level: 443.28±0.10 and 443.61±0.17. When initial ages do overlap, the final ages can be significantly different (e.g., Husson et al. [2016]).

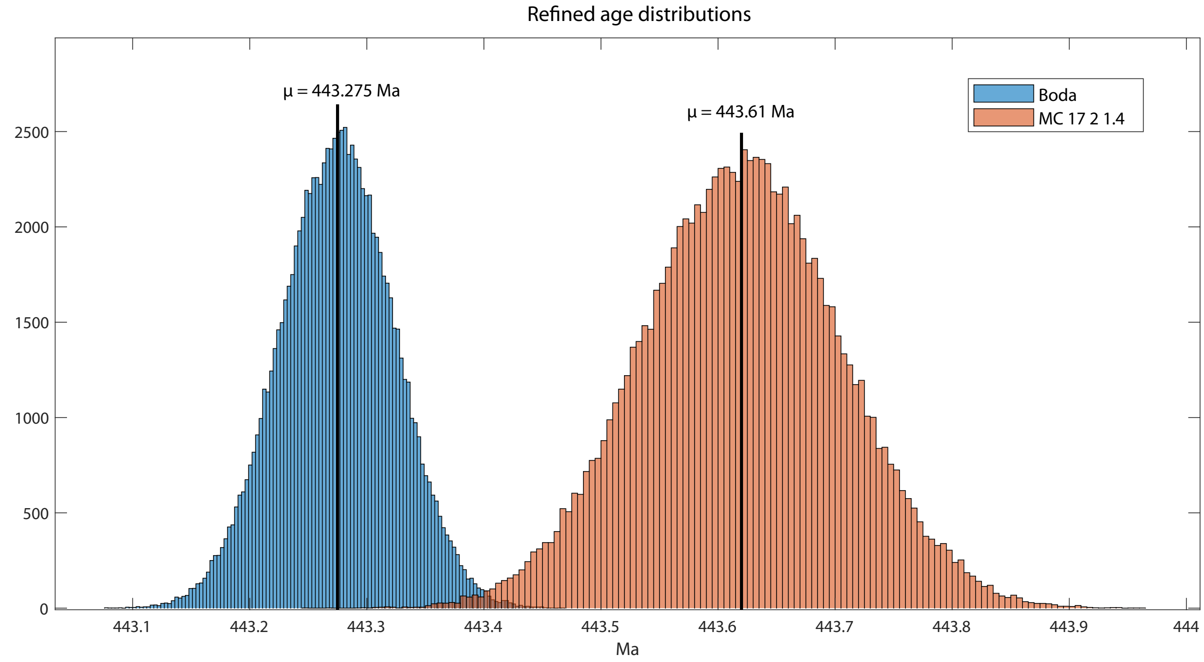

Figure 5.3: Probability age distributions for samples MC 17 2 1.4 (Anticosti) and for the Boda sample after the Markov-chain Monte Carlo method. Note: the means of the two distributions remained the same before and after resampling.

The second step was to produce a duration estimate to quantify the time elapsed between MC1-7-2:1.4 and the Boda bentonite, by subtracting all of the valid date pairs retained. Assuming a constant accumulation rate, the accumulation rate distribution was calculated by dividing the thickness of the sediments separating MC-17-2:1.4 from Boda (projected into the same stratigraphic section) by the duration distribution as shown in equation 5.1:

$$N_{sed} = \frac{h_{BODA} - h_{MC}}{N_{MC} - N_{BODA}} \ , \tag{5.1}$$

where N_{sed} is the accumulation rate distribution (in m/Myr), h_{BODA}-h_{MC} is the thickness of the sediments (in m), while N_{MC} and N_{BODA} are the refined age distributions for the two samples. Each probability distribution is defined by a mean, μ, and a standard deviation, σ.

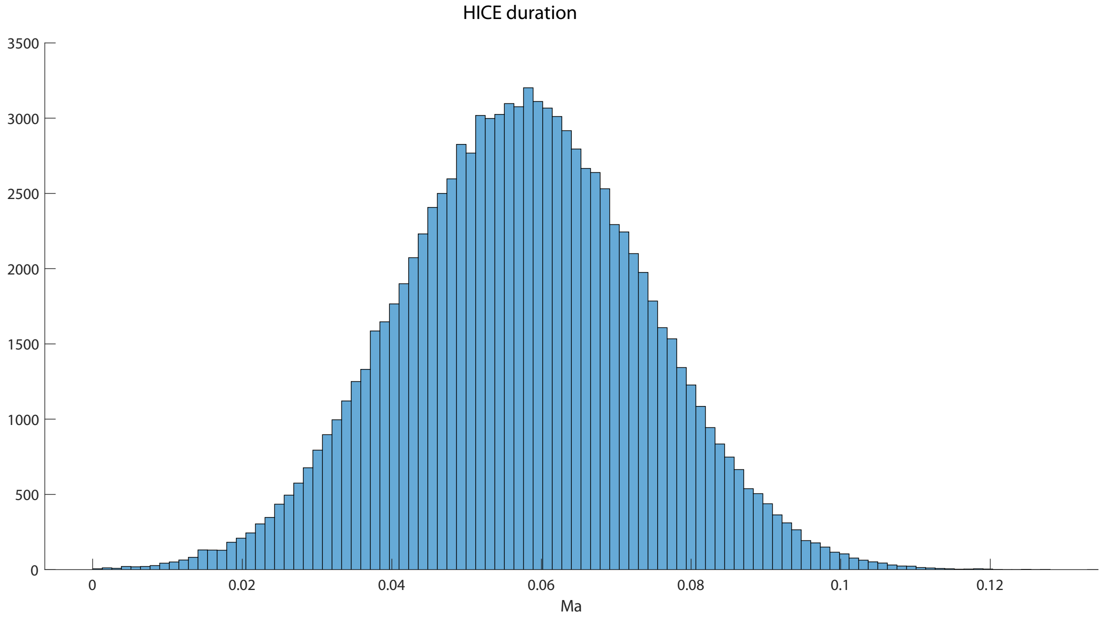

Figure 5.4: Probability distribution for the estimated minimum duration of the HICE.

The third and final step was to produce a probability distribution for the minimum duration distribution of the HICE. It is a minimum estimate, because the HICE at Macaire Creek may be truncated at its top —either because of incomplete sampling, or by a hiatus (Brenchley et al. [2003]). This was calculated by dividing the thickness of the sediments deposited during the HICE (h_{HICE2}-h_{HICE1}) by the accumulation rate distribution (N_{HICE}), as shown in equation 5.2:

$$N_{HICE}(\mu, \sigma) = \frac{h_{HICE2} - h_{HICE1}}{N_{sed}(\mu, \sigma)} \tag{5.2}$$

The minimum HICE duration produced here has a mean of 55.9 kyr with a standard deviation of 17 kyr. It is referred to as a minimum duration because the Laframboise Member may have disconformities near the upper part of the HICE, which would be reflected in reduced sediment thickness, which in turn would results in a shorter HICE duration (see Fig. 5.5b). As opposed to this, if significant disconformities are present below the HICE peak (i.e., where the $\delta^{13}\mathrm{C}_{\mathrm{carb}}$ record is flat and at baseline, and thus not easily detected), the accumulation rate would be faster compared to the one calculated here ($\mathrm{N}_{\mathrm{sed}}(\mu)= \sim 38$ m/Myr), meaning that the duration of the HICE would be even shorter (see Fig. 5.5a) than the estimate calculated here and displayed in Fig. 5.4.

5.3 Carbon model

An estimate of the duration of the HICE was made in the previous section. The calculated duration from base level to peak $\delta^{13}\mathrm{C}_{carb}$ is 31.0±1.9 kyr (2σ), which can be used to constrain a simple model of the HICE. This simple one-box model (see Fig. 5.6), reduces the C cycle into a single surface C reservoir, with one input flux and two output fluxes. Assuming steady state, the input flux equals the sum of the output fluxes. This model is the simplest C cycle model possible, yet it is still useful when considering possible drivers and interpretations of the HICE.

The surface reservoir considered in the model presented here consists of the C present

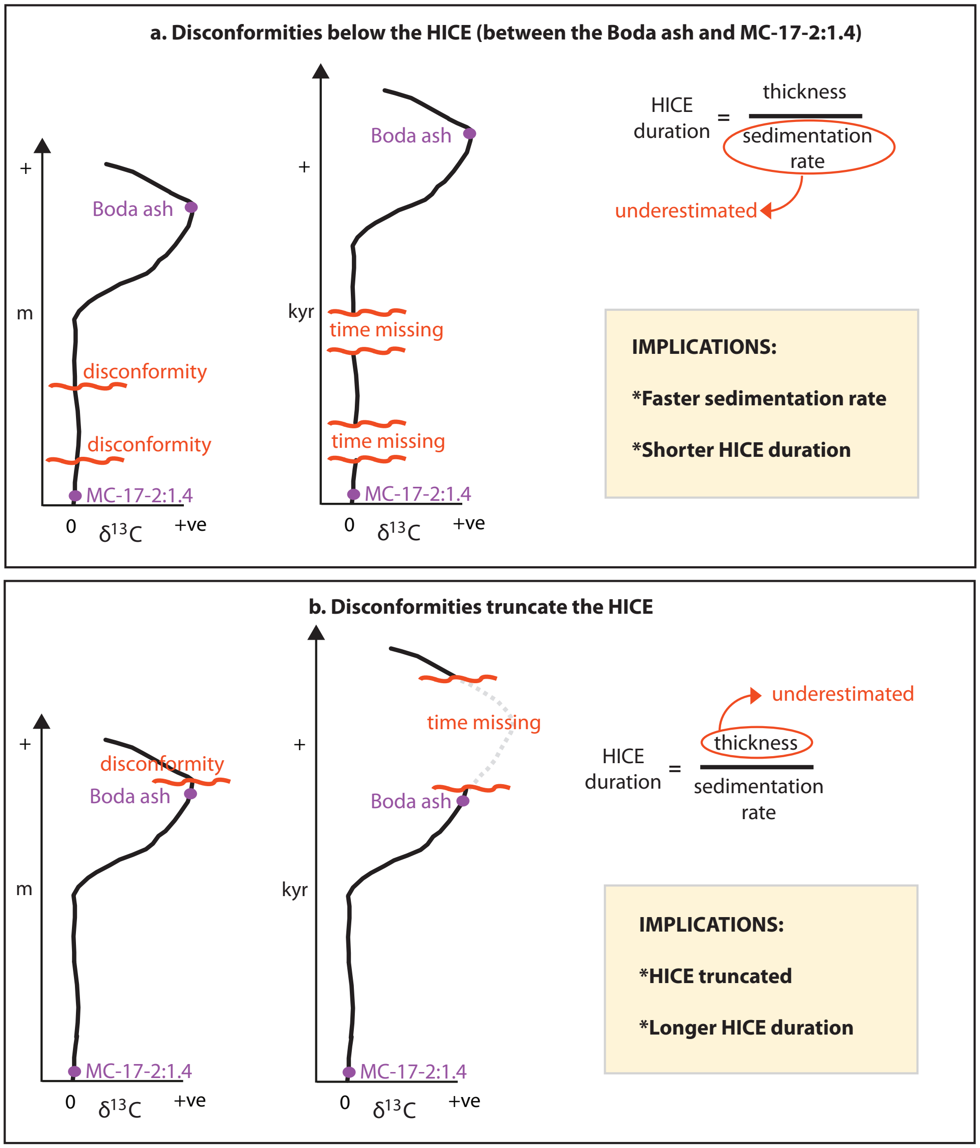

Figure 5.5: This conceptual diagram illustrates the implications that potential disconformities (and discontinuities) would have on the duration of the HICE estimated in the Macaire Creek section.

in the ocean and atmosphere. This is predominantly dissolved inorganic carbon (DIC) in the ocean, which consists of bicarbonate (HCO_3^-), carbonate (CO_3^{2-}) and carbon dioxide (CO_2). The C input consists of the mantle-derived C outgassed from the solid Earth, and the output consists of carbonate C and organic C burial. Assuming steady state conditions, we can write the mass balance as indicated by equation 1 in Husson et al. [2016]:

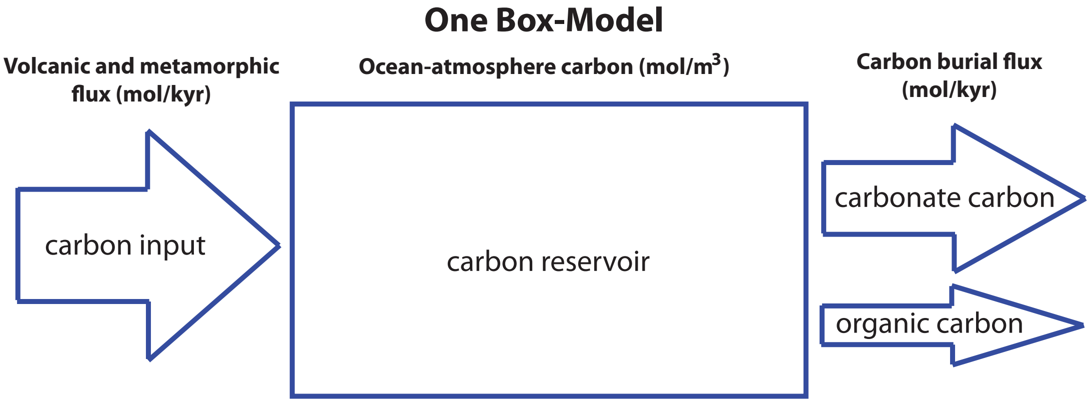

Figure 5.6: Conceptual diagram of a single box carbon model presented here (assuming steady state conditions, input flux = output flux).

$$\delta^{13}C_{input} = (1 - f_{org}) * \delta^{13}C_{DIC} + f_{org} * (\delta^{13}C_{DIC} - \varepsilon_{org}) \ , \tag{5.3}$$

where $\delta^{13}C_{\mathrm{input}}$ is the isotopic value of the volcanic and metamorphic input flux (e.g., -5‰, Kump and Arthur [1999]), f_{org} is the fractional burial of organic C, $\delta^{13}C_{\mathrm{DIC}}$ is the isotopic value of the ocean-atmosphere reservoir (assumed to be equivalent to δ^{13}C of carbonate precipitated from the ocean) and ε_{org} is the fractionation between organic C and carbonate C.

Positive $\delta^{13}C_{carb}$ excursions are commonly interpreted as driven by increases in organic C burial (e.g., Munnecke et al. [2010], Kump and Arthur [1999]), as organic C is depleted in the ^{13}C isotope (e.g., Kump and Arthur [1999]). It is not unreasonable to observe a positive δ^{13}C excursion in time of global cooling. The enhanced organic C burial can be linked to a decrease in atmospheric CO_2 (greenhouse gas), which is associated with the cooling of the Earth's surface temperature. Independently we can also observe that the Upper Ordovician deposits are punctuated by black shales high in organic C content (e.g., Melchin et al. [2013]). The rate of C isotopic change resulting from a change in organic C burial can be calculated using equation 2 from Husson et al. [2016] (adapted from Kump and Arthur [1999]):

$$\frac{d\delta^{13}C_{DIC}}{dt} = \frac{F_{in}}{M_C} * (\delta^{13}C_{input} - (1 - f_{org}) * \delta^{13}C_{DIC} + f_{org} * (\delta^{13}C_{DIC} - \varepsilon_{org})) \tag{5.4}$$

The term on the left-hand side indicates the rate of C isotopic change in the ocean-atmosphere reservoir, F_{in} indicates the C input flux, and M_C indicates the mass (in moles) of the surface C reservoir. The other terms are the same as in equation 5.3. Equation 5.4 was solved numerically using different combinations of C flux and reservoir size. Multiples of modern values were used for F_{in} ($0.6*10^{16}$ mol/kyr, from Kump and Arthur [1999]) as well as for M_C ($3.1*10^{18}$ mol, calculated using ocean volume from Eakins and Sharman [2010] and DIC from Sarmiento and Gruber [2006]), with a constant ε_{org} value of 30‰ (Hayes et al. [1999]). In each model iteration, a positive δ^{13}C excursion was simulated, with $\delta^{13}\mathrm{C_{carb}}$ of DIC rising from a baseline value of 0.6‰ to a maximum of 3.6‰, accomplished by changing f_{org} from 0.17 to 0.29 instantaneously (representing a sudden increase in black shale deposition). Fig. 5.7 shows simulations with different fluxes (the colorful lines on the plot are the fluxes). The time required for $\delta^{13}\mathrm{C_{carb}}$ to raise from the 0.6‰ to 3.6‰ is the response time (see Fig. 5.7), and is senstive to both F_{in} and M_C. For example, the response time will decrease if M_c is held constant and F_{in} is increased. It will increase if M_c is increased and F_{in} is held constant. The grey area in the same figure shows combinations of DIC and C flux that are consistent with the duration of the HICE as constrained by our U-Pb results. For example, if Hirnantian DIC levels were similar to today (2.3 mmol, dashed line in Fig. 5.7), the required input flux would be 80x the modern value for a total HICE duration of ~56 kyr.

Residence time of C in the ocean, i.e. the average length of time that a C atom will remain in the reservoir, is approximately 100 kyr (e.g., Emerson and Hedges [2008], Kump and Arthur [1999]). The duration from base level to peak $\delta^{13}C_{carb}$ calculated in this study is

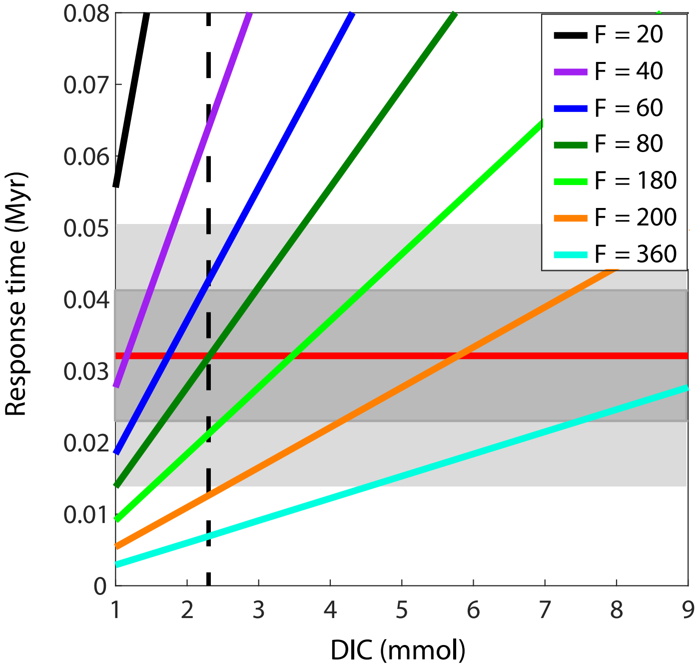

Figure 5.7: This plot depicts the outputs of the carbon model described in this section. Different values for DIC (which indicates the C reservoir size) and for C flux are shown. The red horizontal line indicates the duration from base level to peak $\delta^{13}C_{carb}$ calculated from geochronological constraits in section 5.2, the dark grey area is the standard deviation σ, and the light grey area is 2σ. The colorful lines that are collocated within the grey box represent parameters that are feasible for the response time calculated. The dashed vertical line indicates the modern DIC value (Sarmiento and Gruber [2006]). In the legend (top right), model fluxes are expressed as multiples of the modern value ($F_{in} = 0.6*10^{16}$ mol/kyr, Kump and Arthur [1999], Fig. 1).

slightly less than one third of the modern residence time. Hence this model could indicate that the C turnover in the Hirnantian ocean was much quicker than today. This is not implausible in times of eustatic sea level fall. The enhanced erosion due to larger landmasses and a greater area of shelf exposure, could account for an increased C input and a reduced residence time. On the other hand, the compatible fluxes are extremely high compared to modern values (60-180x). This could suggest that at a $\delta^{13}C_{carb}$ value of 3.64, the system was not yet in equiliblrium and more time was necessary to reach steady state conditions. If this is correct, then an even larger perturbation to the global C cycle is required than an increase of f_{org} from 0.17 to 0.29 to drive the HICE, because the calculation of $f_{org} = 0.29$

assumes that the carbon cycle had reached steady state.

Considering the high fluxes observed in the model presented here, it will be challenging to model the HICE as the C cycle reaching a new equilibrium. A dynamic carbon model that does not assume steady state conditions may be required. Nevertheless, the purpose of this carbon model, similarly to the age model, is to assist the reader to see the possible applications of the results obtained in this study. As the number of radiometric dates from different Upper Ordovician deposits around the world increases, it will be possible to further refine the timescale, and to make more robust global correlations. A refined timescale and more robust C isotope correlations will also allow to produce more refined carbon models.

Chapter 6

Conclusions

Two bentonite samples have successfully been dated with EARTHTIME U-Pb techniques (CA-ID-TIMS), contributing to the record of radiometric ages for the Late Ordovician. One of these samples, MC-17-2:1.4, was collected from the Lousy Cove Mbr of the Ellis Bay Formation (Anticosti Island, Quebec) and its age is 443.61±0.17/0.21/0.52 Ma. Despite the lack of consensus on the placement of the Katian-Hirnantian boundary in this location, the scientific community agrees that the Lousy Cove Mbr is of Late Ordovician age. The age of MC-17-2:1.4 can therefore be considered a strong constraint for the O-S boundary. The other sample, taken from the Boda core facies of the Siljan district (Dalarna County, Sweden) was dated 443.28±0.10/0.15/0.50 Ma. This age can only be seen as a soft constraint as the bentonite sample was collected from a karst pocket that post-dated its encasing sediments.

These results alone might not unravel the conundra of the end Ordovician glaciation and mass extinction, yet they contribute to the refinement of our current knowledge. The current age for the O-S boundary in the International Chronostratigraphic Chart 2018 (Cohen et al. [2018]) is 443.8±1.5 Ma. By comparing this value with the age of the Anticosti sample (443.61±0.52), it appears that the boundary age is very unlikely to be on the older side of this distribution (see Fig. 5.1). This work can be continued through the search for more bentonite. An obvious next step is continued examination of MC-17-1:3.5 and SR-17-2:-0.4, to see if either contain an eruptive age population.

Integrating radiometric ages to the existent chronology, is key to improve the accuracy and resolution of the Late Ordovician timescale, hence allowing an ever better understanding of large scale perturbations. Over time, the increased availability of more and more precise radiometric ages, will help the scientific community to better constrain the rates of various Earth system events, such as the HICE.

Appendix A

Additional Information

This appendix includes the extended version of the U-Pb ID-TIMS analyses conducted at the Princeton Radiogenic Isotope Laboratory, as well as the results of the geochemical analyses performed on sample MC 17 2 1.4 conducted at the Ontario Activation Laboratories Ltd.

- A.1: Composition of the EARTHTIME tracers used in this study;
- A.2: Extended data for ID-TIMS analyses on sample MC-17-2:1.4;
- A.3: Extended data for ID-TIMS analyses on the Boda bentonite sample;
- A.4: Extended data for ID-TIMS analyses on the sample MC-17-1:3.5;
- A.5: Extended data for ID-TIMS analyses on the sample SR-17-2:-0.4;
- A.6: Bulk composition of sample MC-17-2:1.4.

ET 535		
Parameter	**Value**	**1σ (abs.)**
^{205}Pb (mol/g)	1.03E-11	2.58E-14
^{235}U (mol/g)	1.03E-09	2.60E-12
^{204}Pb/^{205}Pb	9.00E-05	9.00E-06
^{206}Pb/^{205}Pb	3.89E-04	1.69E-04
^{207}Pb/^{205}Pb	2.96E-04	1.40E-04
^{208}Pb/^{205}Pb	7.44E-04	3.47E-04
^{233}U/^{235}U	9.95E-01	5.38E-05
^{238}U/^{235}U	3.08E-03	3.96E-07

ET 2535		
Parameter	**Value**	**1σ (abs.)**
^{205}Pb (mol/g)	1.03E-11	2.58E-14
^{235}U (mol/g)	1.03E-09	2.60E-12
^{202}Pb/^{205}Pb	9.99E-01	2.66E-04
^{204}Pb/^{205}Pb	1.05E-04	9.16E-06
^{206}Pb/^{205}Pb	4.83E-04	1.66E-04
^{207}Pb/^{205}Pb	4.32E-04	1.38E-04
^{208}Pb/^{205}Pb	1.04E-03	3.35E-04
^{233}U/^{235}U	9.95E-01	5.38E-05
^{238}U/^{235}U	3.08E-03	3.96E-07

Table A.1: Composition of the EARTHTIME tracers used in this study.

	Dates (Ma)								Composition						Isotopic Ratios										
Fraction	206Pb/ 238U <Th>[a]	±2σ abs	207Pb/ 235U[b]	±2σ abs	207Pb/ 206Pb[b]	±2σ abs	Corr. coef.	% disc[c]	Th/ U[d]	Pb* (pg)[e]	Pbc (pg)[f]	Pb*/ Pbc[g]	%comm 206	%comm 208	206Pb/ 204Pb[h]	206Pb/ 238U[i]	±2σ %	238U/ 206Pb[i]	±2σ %	207Pb/ 235U[i]	±2σ %	207Pb/ 206Pb[i]	±2σ %	208Pb/ 232Th[i]	±2σ %	Fraction
MC17-2-1p4::zircon																										
z1	463.34	0.37	461.6	2.7	454	16	0.178	-2.15	0.80	4.84	0.22	21.523029	-	-	1242	0.074510	0.082	-	-	0.5756	0.74	0.05605	0.73	-	-	z1
z2	461.79	0.25	461.3	1.4	458.9	8.1	0.284	-0.61	0.74	8.71	0.21	41.026704	-	-	2387	0.074252	0.055	-	-	0.5750	0.38	0.05619	0.36	-	-	z2
z3	470.36	0.27	470.98	0.88	474.4	4.9	0.326	0.87	0.55	8.81	0.12	70.515535	-	-	4280	0.075679	0.060	-	-	0.5902	0.23	0.05658	0.22	-	-	z3
z4	443.79	0.40	443.8	2.1	444	13	0.275	0.15	1.02	5.43	0.18	29.629173	-	-	1618	0.071257	0.094	-	-	0.5482	0.59	0.05582	0.57	-	-	z4
z6	462.05	0.23	462.23	0.56	463.5	3.1	0.376	0.33	0.77	33.4	0.20	167.698545	-	-	9630	0.074294	0.051	-	-	0.57653	0.15	0.056307	0.14	-	-	z6
z8	442.8	1.6	442	13	439	77	0.224	-0.85	0.97	6.47	1.49	4.353818	-	-	257	0.07108	0.36	-	-	0.546	3.5	0.0557	3.5	-	-	z8
z9	475.23	0.58	477.0	4.7	486	27	0.257	2.21	0.33	3.63	0.34	10.602157	-	-	697	0.076490	0.13	-	-	0.5996	1.2	0.05688	1.2	-	-	z9
z10	469.07	0.69	466.4	5.4	454	31	0.236	-3.40	0.58	4.54	0.43	10.450079	-	-	646	0.07546	0.15	-	-	0.5830	1.4	0.05606	1.4	-	-	z10
z12	443.53	0.42	444.3	1.4	448.6	8.2	0.304	1.14	1.15	5.29	0.10	52.510558	-	-	2771	0.071215	0.098	-	-	0.5489	0.39	0.05593	0.37	-	-	z12
z13	464.42	0.54	466.0	1.7	474.4	9.5	0.356	2.12	1.06	4.08	0.10	40.300888	-	-	2172	0.074691	0.12	-	-	0.5825	0.46	0.05659	0.43	-	-	z13
z14	462.53	0.66	463.2	1.8	467	10	0.364	0.96	0.75	4.70	0.11	42.603513	-	-	2472	0.07437	0.15	-	-	0.5781	0.49	0.05639	0.46	-	-	z14
z16	470.6	2.3	481.6	8.1	534	44	0.354	11.97	1.15	1.24	0.12	10.094796	-	-	547	0.07572	0.51	-	-	0.607	2.1	0.0582	2.0	-	-	z16
z17	463.56	0.68	465.6	3.1	476	18	0.171	2.64	0.45	2.37	0.14	17.299045	-	-	1092	0.07454	0.15	-	-	0.5818	0.84	0.05663	0.82	-	-	z17
z18	471.4	1.7	470.3	5.1	465	28	0.351	-1.24	0.62	1.72	0.15	11.375691	-	-	695	0.07584	0.38	-	-	0.5891	1.4	0.05636	1.3	-	-	z18
z19	461.36	0.20	461.5	1.0	462.9	6.1	0.267	0.34	0.66	11.5	0.21	54.175552	-	-	3208	0.074179	0.045	-	-	0.5755	0.28	0.05629	0.27	-	-	z19
z20	464.30	0.39	464.0	3.0	463	18	0.275	-0.29	0.90	7.73	0.40	19.375204	-	-	1095	0.074671	0.086	-	-	0.5793	0.81	0.05629	0.79	-	-	z20
z21	1096	11	1104	31	1119	87	0.341	2.02	0.29	0.587	0.20	2.960128	-	-	208	0.1853	1.1	-	-	1.965	4.6	0.0769	4.4	-	-	z21
z22	443.60	0.23	443.5	1.1	443.3	6.7	0.212	-0.05	1.28	11.5	0.18	64.139799	-	-	3288	0.071227	0.053	-	-	0.5477	0.31	0.05580	0.30	-	-	z22
D813-1.7::zircon																										
z3a	443.69	0.85	445.9	8.5	458	49	0.887	3.11	0.92	9.16	2.31	3.974895	-	-	236	0.07124	0.20	-	-	0.551	2.4	0.0561	2.2	-	-	z3a
z8a	442.0	3.6	444	38	454	220	0.918	2.64	0.80	6.35	7.40	0.859017	-	-	67	0.07095	0.84	-	-	0.548	11	0.0560	9.8	-	-	z8a

a Corrected for initial Th/U disequilibrium using radiogenic 208Pb and Th/U[magma] = 2.80000.
b Isotopic dates calculated using λ238 = 1.55125E-10 (Jaffey et al. 1971) and λ235 = 9.8485E-10 (Jaffey et al. 1971).
c % discordance = 100 - (100 * (206Pb/238U date) / (207Pb/206Pb date))
d Th contents calculated from radiogenic 208Pb and 230Th-corrected 206Pb/238U date of the sample, assuming concordance between U-Pb Th-Pb systems.
e Total mass of radiogenic Pb.
f Total mass of common Pb.
g Ratio of radiogenic Pb (including 208Pb) to common Pb.
h Measured ratio corrected for fractionation and spike contribution only.
i Measured ratios corrected for fractionation, tracer, blank and, where applicable, initial common Pb.

Table A.2: MC-17-2:1.4 report table. This table was produced with U-Pb Redux and it shows all the data produced after the TIMS analysis.

	Dates (Ma)								Composition						Isotopic Ratios											
Fraction	206Pb/ 238U <Th>^{a}	±2σ abs	207Pb/ 235U^{b}	±2σ abs	207Pb/ 206Pb^{b}	±2σ abs	Corr. coef.	% disc^{c}	Th/ U^{d}	Pb* (pg)^{e}	Pbc (pg)^{f}	Pb*/ Pbc^{g}	%comm 206	%comm 208	206Pb/ 204Pb^{h}	206Pb/ 238U^{i}	±2σ %	238U/ 206Pb^{i}	±2σ %	207Pb/ 235U^{i}	±2σ %	207Pb/ 206Pb^{i}	±2σ %	208Pb/ 232Th^{i}	±2σ %	Fraction
zircon																										
z2	438.30	0.46	439.7	2.7	448	16	0.419	2.10	0.91	21.7	0.79	27.426148	-	-	1486	0.070345	0.11	-	-	0.5420	0.76	0.05591	0.72	-	-	z2
z3	443.54	0.43	445.0	2.1	453	12	0.434	2.12	0.85	28.4	0.80	35.555034	-	-	1948	0.071214	0.10	-	-	0.5500	0.58	0.05604	0.55	-	-	z3
z4	442.92	0.46	444.6	2.6	454	15	0.442	2.43	0.97	16.5	0.56	29.442914	-	-	1571	0.071113	0.11	-	-	0.5495	0.72	0.05606	0.68	-	-	z4
z5	444.25	0.61	447.1	5.0	462	29	0.352	3.90	0.89	22.6	1.55	14.586052	-	-	802	0.07133	0.14	-	-	0.5532	1.4	0.05627	1.3	-	-	z5
z6	443.19	0.31	443.4	1.4	445.2	8.2	0.388	0.46	0.92	25.7	0.59	43.637890	-	-	2428	0.071156	0.072	-	-	0.5476	0.39	0.05584	0.37	-	-	z6
z7	443.40	0.25	444.1	1.0	448.2	6.1	0.294	1.09	0.83	9.58	0.15	63.474693	-	-	3601	0.071191	0.058	-	-	0.5487	0.28	0.05592	0.27	-	-	z7
z8	436.96	0.22	438.74	0.79	448.5	4.7	0.274	2.59	0.74	12.4	0.14	87.768166	-	-	5078	0.070120	0.051	-	-	0.5405	0.22	0.05593	0.21	-	-	z8
z9	443.24	0.22	444.10	0.68	448.9	3.9	0.389	1.28	0.88	13.5	0.12	114.386981	-	-	6393	0.071166	0.051	-	-	0.5486	0.19	0.055938	0.17	-	-	z9
z10	443.25	0.31	444.3	1.4	450.3	8.2	0.269	1.58	0.88	7.17	0.16	46.046791	-	-	2587	0.071167	0.071	-	-	0.5490	0.38	0.05597	0.37	-	-	z10
z11	443.23	0.20	444.0	1.1	448.3	6.7	0.194	1.15	0.87	10.4	0.19	55.875662	-	-	3140	0.071164	0.047	-	-	0.5485	0.31	0.05592	0.30	-	-	z11
z12	443.35	0.26	443.9	1.2	447.4	7.2	0.334	0.91	0.81	13.3	0.24	55.950117	-	-	3194	0.071183	0.062	-	-	0.5484	0.34	0.05590	0.32	-	-	z12
z13	441.98	0.17	442.12	0.67	443.2	4.0	0.312	0.29	1.01	15.9	0.15	107.358013	-	-	5834	0.070956	0.040	-	-	0.5456	0.19	0.055794	0.18	-	-	z13
z14	443.71	0.22	443.8	1.5	444.4	9.7	-0.044	0.18	0.74	6.85	0.18	37.861310	-	-	2203	0.071242	0.052	-	-	0.5481	0.43	0.05583	0.44	-	-	z14

a Corrected for initial Th/U disequilibrium using radiogenic 208Pb and Th/U[magma] = 2.80000.
b Isotopic dates calculated using λ238 = 1.55125E-10 (Jaffey et al. 1971) and λ235 = 9.8485E-10 (Jaffey et al. 1971).
c % discordance = 100 - (100 * (206Pb/238U date) / (207Pb/206Pb date))
d Th contents calculated from radiogenic 208Pb and 230Th-corrected 206Pb/238U date of the sample, assuming concordance between U-Pb Th-Pb systems.
e Total mass of radiogenic Pb.
f Total mass of common Pb.
g Ratio of radiogenic Pb (including 208Pb) to common Pb.
h Measured ratio corrected for fractionation and spike contribution only.
i Measured ratios corrected for fractionation, tracer and blank.

Table A.3: Boda bentonite report table. This table was produced with U-Pb Redux and it shows all the data produced after the TIMS analysis.

	Dates (Ma)								Composition						Isotopic Ratios											
Fraction	206Pb/ 238U <Th>[a]	±2σ abs	207Pb/ 235U[b]	±2σ abs	207Pb/ 206Pb[b]	±2σ abs	Corr. coef.	% disc[c]	Th/ U[d]	Pb* (pg)[e]	Pbc (pg)[f]	Pb*/ Pbc[g]	%comm 206	%comm 208	206Pb/ 204Pb[h]	206Pb/ 238U[i]	±2σ %	238U/ 206Pb[i]	±2σ %	207Pb/ 235U[i]	±2σ %	207Pb/ 206Pb[i]	±2σ %	208Pb/ 232Th[i]	±2σ %	Fraction
zircon																										
z1	1016.7	4.9	1012	17	1001	52	0.287	-1.57	0.47	1.41	0.33	4.209528	-	-	276	0.17082	0.52	-	-	1.708	2.6	0.0726	2.5	-	-	z1
z2	731.6	1.8	1137.8	4.7	2025	11	0.440	63.88	0.32	3.21	0.23	13.715411	-	-	852	0.12016	0.25	-	-	2.067	0.69	0.12480	0.62	-	-	z2
z3	1408.7	2.6	1447.0	7.1	1504	17	0.299	6.32	0.86	8.38	0.82	10.173286	-	-	578	0.24424	0.20	-	-	3.158	0.92	0.09382	0.88	-	-	z3
z4	1072.8	9.2	1058	57	1026	170	0.432	-4.54	0.82	1.47	0.90	1.636133	-	-	111	0.1811	0.93	-	-	1.83	8.7	0.0735	8.3	-	-	z4
z5	468.9	4.4	453	49	372	290	0.305	-25.98	0.73	1.46	1.21	1.200295	-	-	88	0.07543	0.97	-	-	0.562	13	0.0540	13	-	-	z5
z6	470.5	1.1	468	11	454	61	0.341	-3.62	0.93	2.93	0.50	5.839000	-	-	340	0.07570	0.25	-	-	0.585	2.8	0.0561	2.7	-	-	z6
z7	449.30	0.59	449.6	4.9	452	29	0.307	0.55	1.10	3.24	0.25	12.912972	-	-	704	0.072174	0.14	-	-	0.5571	1.3	0.05601	1.3	-	-	z7
z8	462.11	0.40	463.4	3.2	470	18	0.220	1.68	0.63	4.00	0.24	16.856704	-	-	1017	0.074304	0.090	-	-	0.5783	0.85	0.05647	0.83	-	-	z8
z9	2653	28	2673	13	2687.8	8.0	0.935	1.30	0.44	8.34	0.36	23.387547	-	-	1349	0.5091	1.3	-	-	12.90	1.4	0.18392	0.48	-	-	z9
z10	459.05	0.67	458.2	5.8	454	34	0.275	-1.01	0.56	6.22	0.69	9.056507	-	-	565	0.07379	0.15	-	-	0.5703	1.6	0.05608	1.5	-	-	z10
z11	462.91	0.63	461.9	3.9	457	23	0.275	-1.29	0.73	3.42	0.22	15.517578	-	-	917	0.07444	0.14	-	-	0.5759	1.0	0.05614	1.0	-	-	z11
z12	473.8	2.0	482.0	9.1	522	49	0.425	9.18	0.74	0.929	0.11	8.799957	-	-	526	0.07625	0.43	-	-	0.608	2.4	0.0578	2.2	-	-	z12
z13	472.4	1.8	466	19	435	110	0.257	-8.66	0.30	2.03	0.77	2.637459	-	-	189	0.07601	0.39	-	-	0.582	5.0	0.0556	4.9	-	-	z13
z14	462.07	0.92	459.1	6.1	445	35	0.335	-3.93	0.69	1.25	0.13	9.995112	-	-	602	0.07430	0.21	-	-	0.5717	1.6	0.05583	1.6	-	-	z14
z15	470.5	1.2	463.7	5.8	431	33	0.277	-9.25	0.53	1.88	0.14	13.740913	-	-	855	0.07570	0.27	-	-	0.5788	1.5	0.05548	1.5	-	-	z15

[a] Corrected for initial Th/U disequilibrium using radiogenic 208Pb and Th/U[magma] = 2.80000.
[b] Isotopic dates calculated using λ238 = 1.55125E-10 (Jaffey et al. 1971) and λ235 = 9.8485E-10 (Jaffey et al. 1971).
[c] % discordance = 100 - (100 * (206Pb/238U date) / (207Pb/206Pb date))
[d] Th contents calculated from radiogenic 208Pb and 230Th-corrected 206Pb/238U date of the sample, assuming concordance between U-Pb Th-Pb systems.
[e] Total mass of radiogenic Pb.
[f] Total mass of common Pb.
[g] Ratio of radiogenic Pb (including 208Pb) to common Pb.
[h] Measured ratio corrected for fractionation and spike contribution only.
[i] Measured ratios corrected for fractionation, tracer and blank.

Table A.4: SR-17-2:-0.4 report table. This table was produced with U-Pb Redux and it shows all the data produced after the TIMS analysis.

	Dates (Ma)								Composition						Isotopic Ratios											
Fraction	206Pb/ 238U <Th>[a]	±2σ abs	207Pb/ 235U[b]	±2σ abs	207Pb/ 206Pb[b]	±2σ abs	Corr. coef.	% disc[c]	Th/ U[d]	Pb* (pg)[e]	Pbc (pg)[f]	Pb*/ Pbc[g]	%comm 206	%comm 208	206Pb/ 204Pb[h]	206Pb/ 238U[i]	±2σ %	238U/ 206Pb[i]	±2σ %	207Pb/ 235U[i]	±2σ %	207Pb/ 206Pb[i]	±2σ %	208Pb/ 232Th[i]	±2σ %	Fraction
zircon																										
z1	1549.8	4.5	1577.8	5.0	1615.7	9.4	0.582	4.08	0.37	2.51	0.13	19.824930	-	-	1239	0.27175	0.33	-	-	3.730	0.62	0.09959	0.51	-	-	z1
z2	470.8	1.1	467	11	447	67	0.230	-5.20	0.86	4.01	0.82	4.888170	-	-	293	0.07575	0.24	-	-	0.584	3.0	0.0559	3.0	-	-	z2
z3	2627	10	2693.9	6.8	2744.3	8.9	0.657	4.26	0.17	3.17	0.42	7.484315	-	-	468	0.5031	0.48	-	-	13.198	0.72	0.1903	0.54	-	-	z3
z4	444.72	0.53	445.9	4.3	452	26	0.259	1.66	0.95	3.52	0.25	14.034308	-	-	788	0.071412	0.12	-	-	0.5513	1.2	0.05602	1.2	-	-	z4
z5	620.8	3.3	649	29	747	120	0.262	16.94	0.36	1.52	0.76	1.991909	-	-	145	0.10108	0.56	-	-	0.894	6.0	0.0642	5.8	-	-	z5

[a] Corrected for initial Th/U disequilibrium using radiogenic 208Pb and Th/U[magma] = 2.8000.

[b] Isotopic dates calculated using λ238 = 1.55125E-10 (Jaffey et al. 1971) and λ235 = 9.8485E-10 (Jaffey et al. 1971).

[c] % discordance = 100 - (100 * (206Pb/238U date) / (207Pb/206Pb date))

[d] Th contents calculated from radiogenic 208Pb and 230Th-corrected 206Pb/238U date of the sample, assuming concordance between U-Pb Th-Pb systems.

[e] Total mass of radiogenic Pb.

[f] Total mass of common Pb.

[g] Ratio of radiogenic Pb (including 208Pb) to common Pb.

[h] Measured ratio corrected for fractionation and spike contribution only.

[i] Measured ratios corrected for fractionation, tracer and blank.

Table A.5: MC-17-1:3.5 report table. This table was produced with U-Pb Redux and it shows all the data produced after the TIMS analysis.

Analyte Symbol	Unit	Detection Limit	Analysis Method	MC 17 2 1.4	Analyte Symbol	Unit	Detection Limit	Analysis Method	MC 17 2 1.4
SiO2	%	0.01	FUS-ICP	56.33	Nb	ppm	1	FUS-MS	12
Al2O3	%	0.01	FUS-ICP	15.2	Mo	ppm	2	FUS-MS	< 2
FeO	%	-	-	5.26	Ag	ppm	0.5	FUS-MS	0.5
Fe2O3(T)	%	0.01	FUS-ICP	1.75	In	ppm	0.2	FUS-MS	< 0.2
MnO	%	0.001	FUS-ICP	0.063	Sn	ppm	1	FUS-MS	2
MgO	%	0.01	FUS-ICP	4.8	Sb	ppm	0.5	FUS-MS	< 0.5
CaO	%	0.01	FUS-ICP	3.02	Cs	ppm	0.5	FUS-MS	4.1
Na2O	%	0.01	FUS-ICP	1.66	La	ppm	0.1	FUS-MS	23.3
K2O	%	0.01	FUS-ICP	3.15	Ce	ppm	0.1	FUS-MS	45.7
TiO2	%	0.001	FUS-ICP	0.816	Pr	ppm	0.05	FUS-MS	5.31
P2O5	%	0.01	FUS-ICP	0.14	Nd	ppm	0.1	FUS-MS	20.2
LOI	%		GRAV	7.04	Sm	ppm	0.1	FUS-MS	3.9
Total	%	0.01	FUS-ICP	99.23	Eu	ppm	0.05	FUS-MS	0.79
Sc	ppm	1	FUS-ICP	17	Gd	ppm	0.1	FUS-MS	3.2
Be	ppm	1	FUS-ICP	2	Tb	ppm	0.1	FUS-MS	0.4
V	ppm	5	FUS-ICP	121	Dy	ppm	0.1	FUS-MS	2.7
Ba	ppm	2	FUS-ICP	413	Ho	ppm	0.1	FUS-MS	0.6
Sr	ppm	2	FUS-ICP	106	Er	ppm	0.1	FUS-MS	1.6
Y	ppm	1	FUS-ICP	12	Tm	ppm	0.05	FUS-MS	0.25
Zr	ppm	2	FUS-ICP	202	Yb	ppm	0.1	FUS-MS	1.6
Cr	ppm	20	FUS-MS	290	Lu	ppm	0.01	FUS-MS	0.25
Co	ppm	1	FUS-MS	20	Hf	ppm	0.2	FUS-MS	4.6
Ni	ppm	20	FUS-MS	80	Ta	ppm	0.1	FUS-MS	0.8
Cu	ppm	10	FUS-MS	20	W	ppm	1	FUS-MS	< 1
Zn	ppm	30	FUS-MS	70	Tl	ppm	0.1	FUS-MS	0.5
Ga	ppm	1	FUS-MS	21	Pb	ppm	5	FUS-MS	13
Ge	ppm	1	FUS-MS	1	Bi	ppm	0.4	FUS-MS	< 0.4
As	ppm	5	FUS-MS	5	Th	ppm	0.1	FUS-MS	8.6
Rb	ppm	2	FUS-MS	105	U	ppm	0.1	FUS-MS	2.2

Table A.6: Table showing the bulk composition of sample MC 17 2 1.4. FUS-ICP: Fusion-Inductively Coupled Plasma. FUS-MS: Fusion-Inductively Coupled Plasma-Mass Spectrometry. LOI: Loss On Ignition. Note: a ratio of 3:1 for FeO and Fe_2O_3 was assumed (e.g., Sharma et al. [2005]).

Bibliography

A. Achab, E. Asselin, A. Desrochers, J. F. Riva, and C. Farley. Chitinozoan biostratigraphy of a new Upper Ordovician stratigraphic framework for Anticosti Island, Canada. *Bulletin*, 123(1-2):186–205, 2011.

L. Ainsaar, D. Kaljo, T. Martma, T. Meidla, P. Männik, J. Nõlvak, and O. Tinn. Middle and Upper Ordovician carbon isotope chemostratigraphy in Baltoscandia: a correlation standard and clues to environmental history. *Palaeogeography, Palaeoclimatology, Palaeoecology*, 294(3-4):189–201, 2010.

C. Barnes. Stratigraphy and palaeontology of the Ordovician-Silurian boundary interval, Anticosti Island, Quebec, Canada. *Bulletin of the British Museum, Natural History. Geology*, 43:195–219, 1988.

R. Bathurst. Genesis of stromatactis cavities between submarine crusts in Palaeozoic carbonate mud buildups. *Journal of the Geological Society*, 139(2):165–181, 1982.

S. M. Bergstroem, X. Chen, J. C. Gutiérrez-Marco, and A. Dronov. The new chronostratigraphic classification of the Ordovician System and its relations to major regional series and stages and to δ13C chemostratigraphy. *Lethaia*, 42(1):97–107, 2009.

S. M. Bergström, W. D. Huff, D. R. Kolata, and H. Bauert. Nomenclature, stratigraphy, chemical fingerprinting, and areal distribution of some Middle Ordovician K-bentonites in Baltoscandia. *Gff*, 117(1):1–13, 1995.

S. M. Bergström, M. E. Eriksson, S. A. Young, and E.-M. Widmark. Conodont biostratigraphy, and δ13C and δ34S isotope chemostratigraphy, of the uppermost Ordovician and Lower Silurian at Osmundsberget, Dalarna, Sweden. *GFF*, 134(4):251–272, 2012.

S. M. Bergström, M. E. Eriksson, S. A. Young, P. Ahlberg, and B. Schmitz. Hirnantian (latest Ordovician) δ13C chemostratigraphy in southern Sweden and globally: a refined integration with the graptolite and conodont zone successions. *GFF*, 136(2):355–386, 2014.

S. M. Bergström, M. R. Saltzman, S. A. Leslie, A. Ferretti, S. A. Young, et al. Trans-Atlantic application of the Baltic Middle and Upper Ordovician carbon isotope zonation. *Estonian Journal of Earth Sciences*, 64(1):6–10, 2015.

W. B. Berry. Graptolite occurrence and ecology. *Journal of Paleontology*, pages 285–293, 1962.

J. F. Bowring, N. M. McLean, and S. Bowring. Engineering cyber infrastructure for U-Pb geochronology: Tripoli and U-Pb_Redux. *Geochemistry, Geophysics, Geosystems*, 12(6), 2011.

S. A. Bowring, D. Erwin, R. Parrish, and P. Renne. EARTHTIME: A community-based effort towards high-precision calibration of earth history. *Geochimica et Cosmochimica Acta*, 69:A316–A316, 2005.

P. Brenchley, J. Marshall, G. Carden, D. Robertson, D. Long, T. Meidla, L. Hints, and T. Anderson. Bathymetric and isotopic evidence for a short-lived Late Ordovician glaciation in a greenhouse period. *Geology*, 22(4):295–298, 1994.

P. Brenchley, J. Marshall, and C. Underwood. Do all mass extinctions represent an ecological crisis? Evidence from the Late Ordovician. *Geological Journal*, 36(3-4):329–340, 2001.

P. Brenchley, G. Carden, L. Hints, D. Kaljo, J. Marshall, T. Martma, T. Meidla, and J. Nõlvak. High-resolution stable isotope stratigraphy of Upper Ordovician sequences:

Constraints on the timing of bioevents and environmental changes associated with mass extinction and glaciation. *Geological Society of America Bulletin*, 115(1):89–104, 2003.

X. Chen, J. Rong, J. Fan, R. Zhan, C. E. Mitchell, D. A. Harper, M. J. Melchin, P. Peng, S. C. Finney, X. Wang, et al. The Global Boundary Stratotype Section and Point (GSSP) for the base of the Hirnantian Stage (the uppermost of the Ordovician System). *Episodes*, 29(3):183, 2006.

K. Cohen, D. Harper, P. Gibbard, and J. Fan. International Chronostratigraphic Chart 2018/08. *International Commission on Stratigraphy*, 2018.

D. Condon, B. Schoene, N. McLean, S. Bowring, and R. Parrish. Metrology and traceability of U–Pb isotope dilution geochronology (EARTHTIME Tracer Calibration Part I). *Geochimica et Cosmochimica Acta*, 164:464–480, 2015.

D. J. Condon and M. D. Schmitz. One hundred years of isotope geochronology, and counting. *Elements*, 9(1):15–17, 2013.

R. Cooper, P. Sadler, O. Hammer, and F. Gradstein. The Ordovician Period. In *The geologic time scale*, pages 489–523. Elsevier, 2012.

P. Copper, J. Jin, and A. Desrochers. The Ordovician-Silurian boundary (late Katian–Hirnantian) of western Anticosti Island: revised stratigraphy and benthic megafaunal correlations. *Stratigraphy*, 10(4):213–227, 2013.

F. Corfu. A century of U-Pb geochronology: The long quest towards concordance. *Bulletin*, 125(1-2):33–47, 2013.

B. D. Cramer, C. E. Brett, M. J. Melchin, P. Maennik, M. A. Kleffner, P. I. McLaughlin, D. K. Loydell, A. Munnecke, L. Jeppsson, C. Corradini, et al. Revised correlation of Silurian Provincial Series of North America with global and regional chronostratigraphic units and δ13Ccarb chemostratigraphy. *Lethaia*, 44(2):185–202, 2011.

J. S. Crampton, R. A. Cooper, P. M. Sadler, and M. Foote. Greenhouse- icehouse transition in the Late Ordovician marks a step change in extinction regime in the marine plankton. *Proceedings of the National Academy of Sciences*, 113(6):1498–1503, 2016.

J. R. Creveling, S. Finnegan, J. X. Mitrovica, and K. D. Bergmann. Spatial variation in Late Ordovician glacioeustatic sea-level change. *Earth and Planetary Science Letters*, 496:1–9, 2018.

M.-P. Dabard, A. Loi, F. Paris, J.-F. Ghienne, M. Pistis, and M. Vidal. Sea-level curve for the Middle to early Late Ordovician in the Armorican Massif (western France): Icehouse third-order glacio-eustatic cycles. *Palaeogeography, Palaeoclimatology, Palaeoecology*, 436: 96–111, 2015.

A. Delabroye and M. Vecoli. The end-Ordovician glaciation and the Hirnantian Stage: a global review and questions about Late Ordovician event stratigraphy. *Earth-Science Reviews*, 98(3-4):269–282, 2010.

A. Delabroye, M. Vecoli, J. Nõlvak, and A. Uutela. Biostratigraphic (graptolites, chitinozoans, acritarchs, brachiopods) and chemostratigraphic (δ13C) correlations between latest Ordovician strata in Laurentia and Baltica. In *The Seventh Baltic Stratigraphical Conference 15œ22 May 2008, Estonia, Abstracts and Field Guide*, page 15, 2008.

A. Delabroye, A. Munnecke, T. Servais, T. R. Vandenbroucke, and M. Vecoli. Abnormal forms of acritarchs (phytoplankton) in the upper Hirnantian (Upper Ordovician) of Anticosti Island, Canada. *Review of palaeobotany and palynology*, 173:46–56, 2012.

A. Desrochers, C. Farley, A. Achab, E. Asselin, and J. F. Riva. A far-field record of the end Ordovician glaciation: the Ellis Bay Formation, Anticosti Island, Eastern Canada. *Palaeogeography, Palaeoclimatology, Palaeoecology*, 296(3-4):248–263, 2010.

M. L. Droser and S. Finnegan. The Ordovician radiation: a follow-up to the Cambrian explosion? *Integrative and Comparative Biology*, 43(1):178–184, 2003.

B. Eakins and G. Sharman. Volumes of the Worlds Oceans from ETOPO1. *NOAA National Geophysical Data Center, Boulder, CO*, 7, 2010.

J. O. R. Ebbestad and A. E. Högström. Ordovician of the Siljan district, Sweden. *Sveriges geologiska undersökning, Rapporter och Meddelanden*, (128):7–26, 2007.

J. O. R. Ebbestad, A. E. Högström, Å. M. Frisk, T. Martma, D. Kaljo, B. Kröger, and H. Pärnaste. Terminal Ordovician stratigraphy of the Siljan district, Sweden. *GFF*, 137 (1):36–56, 2015.

S. Emerson and J. Hedges. *Chemical oceanography and the marine carbon cycle*. Cambridge University Press, 2008.

G. Faure and T. M. Mensing. *Isotopes: principles and applications*. Wiley-Blackwell, 2005.

S. Finnegan, K. Bergmann, J. M. Eiler, D. S. Jones, D. A. Fike, I. Eisenman, N. C. Hughes, A. K. Tripati, and W. W. Fischer. The magnitude and duration of Late Ordovician–Early Silurian glaciation. *Science*, 331(6019):903–906, 2011a.

S. Finnegan, S. Peters, and W. Fischer. Late Ordovician-Early Silurian selective extinction patterns in Laurentia and their relationship to climate change. *Ordovician of the World (eds Gutiérrez-Marco JC, Rábano I, Garcia-Bellido D)*, pages 155–9, 2011b.

S. Finnegan, N. A. Heim, S. E. Peters, and W. W. Fischer. Climate change and the selective signature of the Late Ordovician mass extinction. *Proceedings of the National Academy of Sciences*, 109(18):6829–6834, 2012.

S. Finnegan, C. M. Rasmussen, and D. A. Harper. Biogeographic and bathymetric determinants of brachiopod extinction and survival during the Late Ordovician mass extinction. *Proceedings of the Royal Society B: Biological Sciences*, 283(1829):20160007, 2016.

H. Gerstenberger and G. Haase. A highly effective emitter substance for mass spectrometric Pb isotope ratio determinations. *Chemical geology*, 136(3-4):309–312, 1997.

F. M. Gradstein, J. G. Ogg, M. Schmitz, and G. Ogg. *The geologic time scale 2012*. elsevier, 2012.

M. Hambrey. The Late OrdovicianEarly Silurian glacial period. *Palaeogeography, Palaeoclimatology, Palaeoecology*, 51(1-4):273–289, 1985.

D. A. Harper, E. U. Hammarlund, and C. M. Rasmussen. End Ordovician extinctions: a coincidence of causes. *Gondwana Research*, 25(4):1294–1307, 2014.

J. M. Hayes, H. Strauss, and A. J. Kaufman. The abundance of 13C in marine organic matter and isotopic fractionation in the global biogeochemical cycle of carbon during the past 800 Ma. *Chemical Geology*, 161(1-3):103–125, 1999.

C. H. Holland. Series and stages of the Silurian System. *Episodes*, 8(2):101–103, 1985.

C. Holmden, C. Mitchell, D. LaPorte, W. Patterson, M. Melchin, and S. Finney. Nd isotope records of late Ordovician sea-level changeImplications for glaciation frequency and global stratigraphic correlation. *Palaeogeography, Palaeoclimatology, Palaeoecology*, 386:131–144, 2013.

W. D. Huff, S. M. Bergström, D. R. Kolata, and H. Sun. The Lower Silurian Osmundsberg K-bentonite. Part II: mineralogy, geochemistry, chemostratigraphy and tectonomagmatic significance. *Geological Magazine*, 135(1):15–26, 1998.

J. M. Husson, B. Schoene, S. Bluher, and A. C. Maloof. Chemostratigraphic and U–Pb geochronologic constraints on carbon cycling across the Silurian–Devonian boundary. *Earth and Planetary Science Letters*, 436:108–120, 2016.

D. Jablonski. Extinctions: a paleontological perspective. *Science*, 253(5021):754–757, 1991.

A. Jaffey, K. Flynn, L. Glendenin, W. t. Bentley, and A. Essling. Precision measurement of half-lives and specific activities of U 235 and U 238. *Physical Review C*, 4(5):1889, 1971.

J. Jin and P. Copper. Response of brachiopod communities to environmental change during the Late Ordovician mass extinction interval, Anticosti Island, eastern Canada. *Fossils and Strata*, 54(4):l–5, 2008.

D. S. Jones and D. A. Fike. Dynamic sulfur and carbon cycling through the end-Ordovician extinction revealed by paired sulfate–pyrite δ34S. *Earth and Planetary Science Letters*, 363:144–155, 2013.

D. S. Jones, D. A. Fike, S. Finnegan, W. W. Fischer, D. P. Schrag, and D. McCay. Terminal Ordovician carbon isotope stratigraphy and glacioeustatic sea-level change across Anticosti Island (Québec, Canada). *Bulletin*, 123(7-8):1645–1664, 2011.

F. Jourdan, P. Renne, and W. Reimold. An appraisal of the ages of terrestrial impact structures. *Earth and Planetary Science Letters*, 286(1-2):1–13, 2009.

F. Jourdan, W. U. Reimold, and A. Deutsch. Dating terrestrial impact structures. *Elements*, 8(1):49–53, 2012.

D. Kaljo, L. Hints, P. Männik, and J. Nõlvak. The succession of Hirnantian events based on data from Baltica: brachiopods, chitinozoans, conodonts, and carbon isotopes. *Estonian Journal of Earth Sciences*, 57(4), 2008.

T. Kiipli, L. Jeppsson, T. Kallaste, and U. Soderlund. Correlation of Silurian bentonites from Gotland and the eastern Baltic using sanidine phenocryst composition, and biostratigraphical consequences. *Journal of the Geological Society*, 165(1):211–220, 2008.

T. Kiipli, T. Kallaste, V. Nestor, and D. K. Loydell. Integrated Telychian (Silurian) K-bentonite chemostratigraphy and biostratigraphy in Estonia and Latvia. *Lethaia*, 43(1): 32–44, 2010.

B. Kröger and J. O. R. Ebbestad. Palaeoecology and palaeogeography of L ate O rdovician (K atian–H irnantian) cephalopods of the B oda L imestone, S iljan district, S weden. *Lethaia*, 47(1):15–30, 2014.

B. Kröger, J. O. R. Ebbestad, O. Lehnert, C. V. Ullmann, C. Korte, R. Frei, and C. M. Rasmussen. Subaerial speleothems and deep karst in central Sweden linked to Hirnantian glaciations. *Journal of the Geological Society*, 172(3):349–356, 2015.

B. Kröger, J. O. R. Ebbestad, and O. Lehnert. Accretionary mechanisms and temporal sequence of formation of the Boda limestone mud-mounds (Upper Ordovician), Siljan district, Sweden. *Journal of Sedimentary Research*, 86(4):363–379, 2016.

T. Krogh. Improved accuracy of U-Pb zircon ages by the creation of more concordant systems using an air abrasion technique. *Geochimica et Cosmochimica Acta*, 46(4):637–649, 1982.

T. E. Krogh. A low-contamination method for hydrothermal decomposition of zircon and extraction of U and Pb for isotopic age determinations. *Geochimica et Cosmochimica Acta*, 37(3):485–494, 1973.

L. R. Kump and M. A. Arthur. Interpreting carbon-isotope excursions: carbonates and organic matter. *Chemical Geology*, 161(1-3):181–198, 1999.

M. Kunk, J. Sutter, and C. Naeser. High-precision/sup 40/Ar//sup 39/Ar ages of sanidine, biotite, hornblende, and plagioclase from the Fish Canyon Tuff, San Juan volcanic field, south-central Colorado. *Geol. Soc. Am., Abstr. Programs;(United States)*, 17(CONF-8510489-), 1985.

D. Long and P. Copper. Stratigraphy of the Upper Ordovician upper Vaureal and Ellis Bay formations, eastern Anticosti Island, Quebec. *Canadian Journal of Earth Sciences*, 24(9): 1807–1820, 1987.

D. G. Long. Oxygen and carbon isotopes and event stratigraphy near the OrdovicianSilurian boundary, Anticosti Island Quebec. *Palaeogeography, Palaeoclimatology, Palaeoecology*, 104(1-4):49–59, 1993.

D. G. Long. Tempestite frequency curves: a key to Late Ordovician and Early Silurian subsidence, sea-level change, and orbital forcing in the Anticosti foreland basin, Quebec, Canada. *Canadian Journal of Earth Sciences*, 44(3):413–431, 2007.

D. Loydell. Graptolite biozone correlation charts. *Geological Magazine*, 149(1):124–132, 2012.

S. MacLennan, Y. Park, N. Swanson-Hysell, A. Maloof, B. Schoene, M. Gebreslassie, E. Antilla, T. Tesema, M. Alene, and B. Haileab. The arc of the Snowball: U-Pb dates constrain the Islay anomaly and the initiation of the Sturtian glaciation. *Geology*, 46(6):539–542, 2018.

J. D. Marshall and P. D. Middleton. Changes in marine isotopic composition and the late Ordovician glaciation. *Journal of the Geological Society*, 147(1):1–4, 1990.

J. M. Mattinson. Zircon U–Pb chemical abrasion (CA-TIMS) method: combined annealing and multi-step partial dissolution analysis for improved precision and accuracy of zircon ages. *Chemical Geology*, 220(1-2):47–66, 2005.

J. M. Mattinson. Revolution and evolution: 100 years of U–Pb geochronology. *Elements*, 9 (1):53–57, 2013.

M. J. Melchin. Restudy of some Ordovician–Silurian boundary graptolites from Anticosti Island, Canada, and their biostratigraphic significance. *Lethaia*, 41(2):155–162, 2008.

M. J. Melchin, C. Holmden, and S. H. Williams. Correlation of graptolite biozones, chitinozoan biozones, and carbon isotope curves through the Hirnantian. *Ordovician from the Andes*, 17:101–104, 2003.

M. J. Melchin, C. E. Mitchell, C. Holmden, and P. Štorch. Environmental changes in the Late Ordovician–early Silurian: Review and new insights from black shales and nitrogen isotopes. *GSA Bulletin*, 125(11-12):1635–1670, 2013.

J. S. Miller, J. E. Matzel, C. F. Miller, S. D. Burgess, and R. B. Miller. Zircon growth and recycling during the assembly of large, composite arc plutons. *Journal of Volcanology and Geothermal Research*, 167(1-4):282–299, 2007.

K. Min, P. R. Renne, and W. D. Huff. 40Ar/39Ar dating of Ordovician K-bentonites in Laurentia and Baltoscandia. *Earth and Planetary Science Letters*, 185(1-2):121–134, 2001.

A. Mungchamnankit, P. Limsuwan, K. Thongcham, and S. Meejoo. The electron spin resonance study of Gd3+ in natural zircon. *Journal of Magnetism and Magnetic Materials*, 320(3-4):479–482, 2008.

A. Munnecke, M. Calner, D. A. Harper, and T. Servais. Ordovician and Silurian sea–water chemistry, sea level, and climate: a synopsis. *Palaeogeography, Palaeoclimatology, Palaeoecology*, 296(3-4):389–413, 2010.

G. Ogg and G. Ogg. Gradstein MF, 2008, The Concise Geologic Time Scale, 2008.

F. Paris, A. Achab, E. Asselin, X.-H. Chen, Y. Grahn, J. Nõlvak, O. Obut, J. Samuelsson, N. Sennikov, M. Vecoli, et al. Chitinozoans. *The great Ordovician biodiversification event*, pages 294–311, 2004.

B. R. Pratt. The origin, biota and evolution of deep-water mud-mounds. In *Carbonate mud-mounds: their origin and evolution*, volume 23, pages 49–123. International Association of Sedimentologists, Special Publication 23, 1995.

P. C. Quinton, A. D. Herrmann, S. A. Leslie, and K. G. MacLeod. Carbon cycling across the southern margin of Laurentia during the Late Ordovician. *Palaeogeography, palaeoclimatology, palaeoecology*, 458:63–76, 2016.

W. U. Reimold, S. P. Kelley, S. C. Sherlock, H. Henkel, and C. Koeberl. Laser argon dating of melt breccias from the Siljan impact structure, Sweden: Implications for a possible relationship to Late Devonian extinction events. *Meteoritics & Planetary Science*, 40(4): 591–607, 2005.

J. Riva. Graptolites at and below the Ordovician-Silurian boundary on Anticosti Island, Canada. *Bulletin of the British Museum, Natural History. Geology*, 43:21–237, 1988.

J. Rong, M. Melchin, S. H. Williams, T. N. Koren, and J. Verniers. Report of the restudy of the defined global stratotype of the base of the Silurian System. *Episodes*, 31(3):315–318, 2008.

K. Rosman and P. Taylor. Table of isotopic masses and natural abundances. *Pure and Applied Chemistry*, 71:1593–1607, 1999.

C. S. Ross and E. V. Shannon. The minerals of bentonite and related clays and their physical properties 1. *Journal of the American Ceramic Society*, 9(2):77–96, 1926.

R. Ross, C. Naeser, G. Izett, J. Obradovich, M. Bassett, C. Hughes, L. Cocks, W. Dean, J. Ingham, C. Jenkins, et al. Fission-track dating of British Ordovician and Silurian stratotypes. *Geological Magazine*, 119(2):135–153, 1982.

T. Sami and A. Desrochers. Episodic sedimentation on an early Silurian, storm-dominated carbonate ramp, Becscie and Merrimack formations, Anticosti Island, Canada. *Sedimentology*, 39(3):355–381, 1992.

J. L. Sarmiento and N. Gruber. *Ocean biogeochemical dynamics.* Princeton university press, 2006.

B. F. Schaefer. *Radiogenic isotope geochemistry: A guide for industry professionals.* Cambridge University Press, 2016.

U. Schärer. The effect of initial230Th disequilibrium on young UPb ages: the Makalu case, Himalaya. *Earth and Planetary Science Letters*, 67(2):191–204, 1984.

M. D. Schmitz and K. F. Kuiper. High-precision geochronology. *Elements*, 9(1):25–30, 2013.

B. Schoene. 4.10-U–Th–Pb Geochronology. *Treatise on geochemistry*, 4:341–378, 2014.

B. Schoene, C. Latkoczy, U. Schaltegger, and D. Günther. A new method integrating high-precision U–Pb geochronology with zircon trace element analysis (U–Pb TIMS-TEA). *Geochimica et Cosmochimica Acta*, 74(24):7144–7159, 2010.

N. J. Shackleton. Oceanic carbon isotope constraints on oxygen and carbon dioxide in the Cenozoic atmosphere. *The carbon cycle and atmospheric CO2: natural variations Archean to present*, 32:412–417, 1985.

S. Sharma, G. R. Dix, and M. Villeneuve. Petrology and potential tectonic significance of a K-bentonite in a Taconian shale basin (eastern Ontario, Canada), northern Appalachians. *Geological Magazine*, 142(2):145–158, 2005.

P. M. Sheehan. The late Ordovician mass extinction. *Annual Review of Earth and Planetary Sciences*, 29(1):331–364, 2001.

J. Smolarek, L. Marynowski, W. Trela, P. Kujawski, and B. R. Simoneit. Redox conditions and marine microbial community changes during the end-Ordovician mass extinction event. *Global and Planetary Change*, 149:105–122, 2017.

A. Soufiane and A. Achab. Chitinozoan zonation of the Late Ordovician and the Early Silurian of the island of Anticosti, Québec, Canada. *Review of Palaeobotany and Palynology*, 109(2):85–111, 2000.

A. V. Staden, U. Zimmermann, F. Chemale Jr, J. Gutzmer, and G. Germs. Correlation of Ordovician diamictites from Argentina and South Africa using detrital zircon dating. *Journal of the Geological Society*, 167(1):217–220, 2010.

Y. Suzuki, Y. Shiino, and J. Bergström. Stratigraphy, carbonate facies and trilobite associations in the Hirnantian part of the Boda Limestone, Sweden. *GFF*, 131(4):299–310, 2009.

M. Tiwari, A. K. Singh, and D. K. Sinha. Stable isotopes: Tools for understanding past climatic conditions and their applications in chemostratigraphy. In *Chemostratigraphy*, pages 65–92. Elsevier, 2015.

P. Toghill. The graptolite assemblages and zones of the Birkhill Shales (Lower Silurian) at Dobb's Linn. *Palaeontology*, 11(5):654–668, 1968.

R. Tucker and W. McKerrow. Early Paleozoic chronology: a review in light of new U–Pb zircon ages from Newfoundland and Britain. *Canadian Journal of Earth Sciences*, 32(4):368–379, 1995.

R. Tucker, T. Krogh, R. Ross Jr, and S. Williams. Time-scale calibration by high-precision UPb zircon dating of interstratified volcanic ashes in the Ordovician and Lower Silurian stratotypes of Britain. *Earth and Planetary Science Letters*, 100(1-3):51–58, 1990.

C. J. Underwood. Graptolite preservation and deformation. *Palaios*, pages 178–186, 1992.

C. J. Underwood, S. Crowley, J. Marshall, and P. Brenchley. High-resolution carbon isotope stratigraphy of the basal Silurian Stratotype (Dob's Linn, Scotland) and its global correlation. *Journal of the Geological Society*, 154(4):709–718, 1997.

J. W. Waldron, S. D. Anderson, P. A. Cawood, L. B. Goodwin, J. Hall, R. A. Jamieson, S. E. Palmer, G. S. Stockmal, and P. F. Williams. Evolution of the Appalachian Laurentian margin: Lithoprobe results in western Newfoundland. *Canadian Journal of Earth Sciences*, 35(11):1271–1287, 1998.

I. Wendt and C. Carl. The statistical distribution of the mean squared weighted deviation. *Chemical Geology: Isotope Geoscience Section*, 86(4):275–285, 1991.

G. W. Wetherill. Discordant uranium-lead ages, I. *Eos, Transactions American Geophysical Union*, 37(3):320–326, 1956.

W. M. White. *Isotope geochemistry*. John Wiley & Sons, 2015.

J. A. Winchester and P. A. Floyd. Geochemical discrimination of different magma series and their differentiation products using immobile elements. *Chemical geology*, 20:325–343, 1977.

D. F. Wright and A. L. Stigall. Geologic drivers of Late Ordovician faunal change in Laurentia: investigating links between tectonics, speciation, and biotic invasions. *PLoS One*, 8(7):e68353, 2013.

N. Wright, S. Zahirovic, R. Müller, and M. Seton. Towards community-driven paleogeographic reconstructions: integrating open-access paleogeographic and paleobiology data with plate tectonics. *Biogeosciences*, 10(3):1529–1541, 2013.

C. Xu, F. Jun-Xuan, M. Melchin, and C. Mitchell. Hirnantian (latest Ordovician) graptolites from the Upper Yangtze region, China. *Palaeontology*, 48(2):235–280, 2005.

C. Xu, Z. Yuan-Dong, and F. Jun-Xuan. Ordovician graptolite evolutionary radiation: a review. *Geological Journal*, 41(3-4):289–301, 2006.

C. Zou, Z. Qiu, S. W. Poulton, D. Dong, H. Wang, D. Chen, B. Lu, Z. Shi, and H. Tao. Ocean euxinia and climate change double whammy drove the Late Ordovician mass extinction. *Geology*, 46(6):535–538, 2018.